

Exploring the crossover between high-energy-density plasma and ultracold neutral plasma physics

Cite as: Phys. Plasmas **26**, 100501 (2019); <https://doi.org/10.1063/1.5119144>

Submitted: 09 July 2019 . Accepted: 22 September 2019 . Published Online: 24 October 2019

Scott D. Bergeson , Scott D. Baalrud , C. Leland Ellison, Edward Grant, Frank R. Graziani , Thomas C. Killian , Michael S. Murillo, Jacob L. Roberts, and Liam G. Stanton 

COLLECTIONS

 This paper was selected as an Editor's Pick



View Online



Export Citation



CrossMark





AVS Quantum Science

A high impact interdisciplinary journal for **ALL** quantum science



ACCEPTING SUBMISSIONS

Exploring the crossover between high-energy-density plasma and ultracold neutral plasma physics

Cite as: Phys. Plasmas **26**, 100501 (2019); doi: [10.1063/1.5119144](https://doi.org/10.1063/1.5119144)

Submitted: 9 July 2019 · Accepted: 22 September 2019 ·

Published Online: 24 October 2019



View Online



Export Citation



CrossMark

Scott D. Bergeson,^{1,a)}  Scott D. Baalrud,^{2,b)}  C. Leland Ellison,^{3,c)}  Edward Grant,^{4,d)}  Frank R. Graziani,^{3,e)} 
Thomas C. Killian,^{5,f)}  Michael S. Murillo,^{6,g)}  Jacob L. Roberts,^{7,h)}  and Liam G. Stanton^{8,i)} 

AFFILIATIONS

¹Department of Physics and Astronomy, Brigham Young University, Provo, Utah 84602, USA

²Department of Physics and Astronomy, University of Iowa, Iowa City, Iowa 52242, USA

³Lawrence Livermore National Laboratory, Livermore, California 94550, USA

⁴Department of Chemistry, University of British Columbia, Vancouver, British Columbia V6T 1Z1, Canada

⁵Department of Physics and Astronomy, Rice University, Houston, Texas 77005, USA

⁶Department of Computational Mathematics, Science and Engineering, Michigan State University, East Lansing, Michigan 48824, USA

⁷Department of Physics, Colorado State University, Fort Collins, Colorado 80523, USA

⁸Department of Mathematics and Statistics, San Jose State University, San Jose, California 95192, USA

^{a)}Electronic mail: scott.bergeson@byu.edu

^{b)}Electronic mail: scott-baalrud@uiowa.edu

^{c)}Electronic mail: ellison6@llnl.gov

^{d)}Electronic mail: edgrant@chem.ubc.ca

^{e)}Electronic mail: graziani1@llnl.gov

^{f)}Electronic mail: killian@rice.edu

^{g)}Electronic mail: murillom@msu.edu

^{h)}Electronic mail: jacob.roberts@colostate.edu

ⁱ⁾Electronic mail: liam.stanton@sjsu.edu

ABSTRACT

In this paper, we present ideas that were part of the miniconference on the crossover between High Energy Density Plasmas (HEDP) and Ultracold Neutral Plasmas (UNPs) at the 60th Annual Meeting of the American Physical Society Division of Plasma Physics, November 2018. We give an overview of UNP experiments with an emphasis on measurements of the time-evolving ion density and velocity distributions, the electron thermalization rate, and plasma self-assembly—all just inside the strongly coupled plasma regime. We also present theoretical and computational models that were developed to understand a subset of HEDP experiments. However, because HEDP experiments display similar degrees of strong coupling, many aspects of these models can be vetted using precision studies of UNPs. This comparison is important because some statistical assumptions used for ideal plasmas are of questionable validity in the strongly coupled plasma regime. We summarize two theoretical approaches that extend kinetic theories into the strong-coupling regime and show good agreement for momentum transfer and self-diffusion. As capabilities improve, both computationally and experimentally, UNP measurements may help guide the ongoing development of HEDP-appropriate plasma models. Future opportunities in viscosity, energy relaxation, and magnetized plasmas are discussed.

© 2019 Author(s). All article content, except where otherwise noted, is licensed under a Creative Commons Attribution (CC BY) license (<http://creativecommons.org/licenses/by/4.0/>). <https://doi.org/10.1063/1.5119144>

TABLE OF CONTENTS

I. INTRODUCTION	2	A. Mean force kinetic theory	5
A. Overview of HEDP physics	3	B. Ion transport	7
B. Overview of UNP physics	4	C. Electron-ion transport	8
C. Comments on Fermi degeneracy	5	D. Magnetized plasmas	8
II. MEAN FORCE KINETIC THEORY APPLIED TO TRANSPORT CALCULATIONS	5	III. IONIC TRANSPORT CALCULATIONS IN NONIDEAL PLASMAS USING AN EFFECTIVE BOLTZMANN EQUATION	8

A. Boltzmann equation 9
 B. Transport coefficients 9
 C. Coulomb logarithms 10
 D. Effective Boltzmann equation 10
 E. Numerical fits 11
 F. Connection to UNPs 11

IV. NEW TRANSPORT MODELS IN THE ARES MULTIPHYSICS CODE 11
 A. Plasma viscosity 11
 B. Electron-ion coupling 13
 C. Discussion 15

V. AVALANCHE TO STRONG COUPLING IN A MOLECULAR RYDBERG GAS 15
 A. The molecular beam ultracold plasma compared with a MOT 15
 B. Supersonic molecular beam temperature and particle density 16
 C. Penning ionization 17
 D. Spontaneous electron-impact avalanche 17
 E. Plasma evolution in a Rydberg gas Gaussian ellipsoid 18
 F. A molecular ultracold plasma state of arrested relaxation 19
 G. Applications of molecular plasmas to HEDP 20

VI. STUDYING COLLISIONAL PROCESSES IN STRONGLY COUPLED STRONTIUM UNPs 20
 A. Strontium ultracold neutral plasmas 20
 B. Optical probes and manipulations of strontium ions in ultracold neutral plasmas 20
 C. Velocity equilibration beyond Landau-Spitzer 21
 D. Self-diffusion 21
 E. Future prospects 22

VII. ELECTRON-ION COLLISION PHYSICS 22
 A. Advantages of lower density UNPs 22
 B. Initiating and measuring center-of-mass electron oscillations for electron-ion collision measurements 23
 C. Comparison of measured electron-ion collision rates to theoretically predicted rates 23
 D. Future investigations 25

VIII. MOMENTUM TRANSFER IN DUAL-SPECIES ULTRACOLD NEUTRAL PLASMAS 25
 A. Experiment 25
 B. The fluid simulation 26
 1. The interspecies friction force 26
 2. The Coulomb logarithm and momentum transfer 27
 3. The velocity distribution $f(v_z)$ 27
 C. Comparing simulation with experiment 28
 D. Discussion and future directions 28

IX. CONCLUSION AND OUTLOOK 28

I. INTRODUCTION

High-energy-density plasmas (HEDPs) exist at high temperatures and high densities. They play a key role in military applications, high-intensity and high-brightness sources of x-rays and neutrons, and nuclear fusion research and technology. Billions of dollars have been spent trying to generate, characterize, understand, and control

these sources. The HEDP environment occurs at pressures in excess of 100 GPa in the presence of free electrons.^{1,2} In equilibrium, this corresponds to solid-density plasmas at temperatures of millions of degrees.

Ultracold neutral plasmas (UNPs), on the other hand, exist at the relatively low densities that of a reasonably good laboratory vacuum system and temperatures near 1 K. Because the density is low and the electrons are relatively warm, the ultracold plasmas exist without significant recombination.

Despite the differences in temperature and density between HEDP and UNPs, ion interactions in both systems can be described in many cases with a classical Yukawa one-component plasma (YOCP) model.^{3,4} Even though HEDPs and UNPs are multicomponent plasmas, pairwise ion interactions can be approximated using a screened, repulsive $1/r$ potential,

$$V(r_{ij}) = \frac{Z_i Z_j e^2}{4\pi\epsilon_0 r_{ij}} \exp\left(-\frac{r_{ij}}{\lambda}\right), \quad (1)$$

where Z_i and Z_j are the (effective) ionization states of ions i and j and r_{ij} is the distance between them. In this model, electrons serve as a smooth and continuous neutralizing background charge, screening ion charges with a characteristic length λ . The screening length is often taken to be the Debye length $\lambda_D = [k_B T_e \epsilon_0 / (n e^2)]^{1/2}$, where n is the electron density and T_e is the electron temperature. However, as we will see in this review (Sec. III), other formulations of this length can be made to include ion screening, quantum, and strong-coupling effects.

A YOCP model does not capture all of the expected physics in HEDPs and UNPs. Electron-ion thermalization,^{19–21} for example, is not explicitly included in the YOCP model. Quantum effects,^{22,23} such as bound states, three-body recombination, and quantum degeneracy, are also not included. HEDPs and UNPs share similar physics in these non-YOCP aspects as well.

When the YOCP model is valid, two parameters uniquely define the plasma state.^{5,24} One is the (unscreened) strong-coupling parameter,

$$\Gamma = \frac{Z^2 e^2}{4\pi\epsilon_0 a_{ws} k_B T}, \quad (2)$$

where $a_{ws} = (3/4\pi n_i)^{1/3}$ is the Wigner-Seitz radius (ion sphere radius), n_i is the ion density, and T is the ion temperature. The other is the inverse scaled screening length,

$$\kappa = \frac{a_{ws}}{\lambda}, \quad (3)$$

where λ is once again the screening length in the YOCP model.

The YOCP model is commonly used to describe ion-ion interactions in both weakly and strongly coupled plasmas^{3,5} such as white dwarf stars,⁶ the cores of Jovian planets,^{7,8} plasmas produced during inertial confinement fusion,⁹ dusty plasmas consisting of highly charged dust particles,^{10–13} charge-stabilized colloidal systems such as latex spheres in a polar solvent,^{14,15} some non-neutral plasmas,¹⁶ and ions in UNPs.^{17,18} It is valid for $0 \leq \kappa < 7$ (see Ref. 5 and references therein).

Even though HEDPs and UNPs are radically different in density and temperature, they find areas of overlap in the $\kappa\Gamma$ plot shown in Fig. 1. Because of this, tests in well-diagnosed table-top experiments,

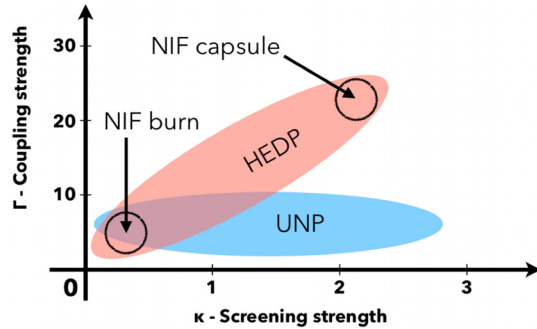


FIG. 1. A $\kappa\Gamma$ plot showing regions of UNPs and HEDPs. In these scaled units, the similarity of ultracold neutral plasmas and high-energy-density plasmas becomes clearer. UNPs display the physics of moderately strongly coupled and moderately shielded plasmas without quantum degeneracy.

when paired with appropriate molecular dynamics (MD) simulations or advanced kinetic theories, can provide direct insights into some aspects of HEDPs.

These tests are important because the onset of strong coupling, when $\Gamma \geq 1$, corresponds to densities outside the limits of the validity of standard kinetic theories. When $\Gamma \geq 1$, the number of particles per Debye sphere is small and statistical assumptions about collisions become less clearly justified. Furthermore, the evaluation of the Coulomb logarithm becomes problematic (Sec. III C). Strong coupling also introduces qualitatively new behaviors in the plasma that arise from spatial order over a variety of length scales. Disentangling strong-coupling effects from the many other processes that occur in HEDPs is difficult because the measurement environment is challenging.

Strongly coupled physics appears in many systems. For plasmas, as Eq. (2) indicates, strong coupling occurs when nearest-neighbor interaction energy exceeds the average kinetic energy. This occurs in some stages of laser-driven plasma experiments and X- and Z-pinch plasmas, dusty plasmas, quark-gluon plasmas, and other systems. In pursuit of nuclear fusion, HEDP facilities (NIF, Z, Omega, etc.) have continued to probe higher temperatures. As the temperatures increase, the resulting plasmas are becoming increasingly kinetic and less strongly coupled, with coupling parameters in the 1–10 range, as shown in Fig. 1. Thus, understanding transport processes in this parameter range is of extreme relevance to the HEDP community. This has been a particular focus of UNP experiments.

In this article, we briefly review HEDPs and UNPs with an emphasis on the areas of possible overlap. We then present a few theoretical approaches for describing strongly coupled plasmas with moderate values of Γ , which suggest questions of interest to HEDPs that appear accessible with UNPs (Secs. II–IV). Finally, we describe current trends in UNP experiments that are exploring this interface (Secs. V–VIII). This paper reports on presentations in the miniconference on the crossover between High Energy Density Plasmas (HEDP) and Ultracold Neutral Plasmas (UNPs) at the 60th Annual Meeting of the American Physical Society’s Division of Plasma Physics, November 2018. While this is not a comprehensive summary of either HEDP or UNP science, we have attempted to connect to other subfields of plasma science when appropriate.

A. Overview of HEDP physics

High energy-density physics is defined as the science of matter with an energy density that exceeds 10^{11} J/m³. It is the study of matter with a pressure over a million times that of our everyday experience—far greater than the crushing pressures at the bottom of the ocean and comparable to the Earth’s center.

High energy densities can be created by any combination of the particles in the plasma. It is customary to consider photons, electrons, and ions and to estimate the pressure, rather than the energy, as

$$P_{total} = P_\gamma + P_e + P_i. \quad (4)$$

Here, the photon pressure in thermodynamic equilibrium is written as

$$P_\gamma = \frac{4\sigma}{3c} T_{rad}^4, \quad (5)$$

where σ is the Stefan-Boltzmann constant, the electron pressure for an ideal Fermi gas

$$P_e = \frac{2T_e}{\lambda^3} f_{5/2}(z), \quad (6)$$

where $f_{5/2}$ is a Fermi integral in terms of the fugacity z ; this interpolates between the classic limit of $n_e k_B T_e$ and the quantum limit of $\frac{2}{5} n_e E_F$, where the Fermi energy is given by

$$E_F = \frac{\hbar^2 (3\pi^2 n_e)^{2/3}}{2m_e}, \quad (7)$$

where m_e is the electron mass. In the absence of ion degeneracy or correlation effects, the ionic pressure can be found using the ideal gas relation

$$P_i = n_i k_B T_i. \quad (8)$$

Note that, in general, all of the species have different temperatures. An important quantum length scale also appears here, the thermal de Broglie wavelength

$$\lambda_{th} = \sqrt{\frac{2\pi\hbar^2}{m_e k_B T_e}}, \quad (9)$$

which characterizes the quantum smearing length required by the Heisenberg uncertainty relation at temperature T_e . Another parameter commonly used to determine the importance of quantum effects is the Brueckner parameter,¹³

$$r_s = \frac{a_{ws}}{a_B}, \quad (10)$$

where $a_B = (4\pi\epsilon_0\hbar^2)/(mZ^2e^2)$ is the effective Bohr radius for particles of mass m and charge state Z . Ideal quantum systems correspond to $r_s \ll 1$. With the foregoing estimates, high energy density science is thus the science of matter with $P_{tot} > 1$ Mbar.

Various plasma regimes are shown in Fig. 2 where the solid black line is the contour of one megabar pressure from Eq. (4). The horizontal branch marked “radiation” at low density is primarily determined by the radiation pressure from Eq. (5) and has no density dependence. In this diagram, we have assumed $T_\gamma = T_e = T_i$. The classical electron-ion pressure generates the diagonal line marked “classical.” At high densities and low temperatures, however, quantum degeneracy becomes important. The Fermi degeneracy parameter,

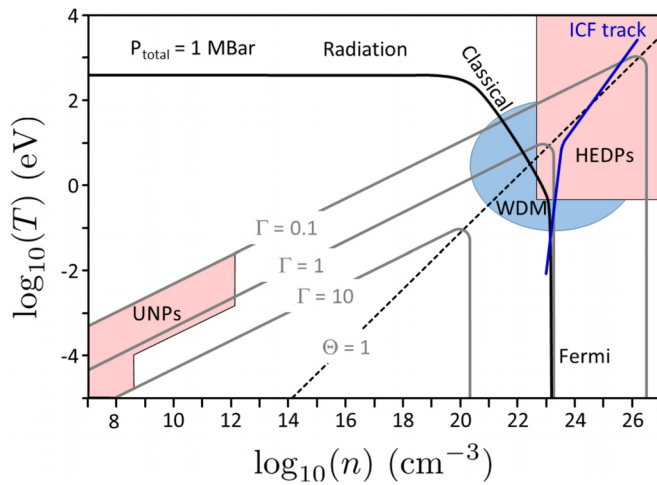


FIG. 2. Plasma phase diagram in logarithmic temperature number-density space. The black solid line shows a total pressure of 1 Mbar from Eq. (4). The gray lines show the values of the Coulomb coupling parameter for $\Gamma = 0.1, 1,$ and 10 for hydrogen using Eq. (2). The dashed black line shows $\Theta = 1$ from Eq. (11). To the right and below this dashed line, quantum effects become important. A rough inertial confinement fusion track is shown as a blue line. The shaded pink area in the lower left-hand portion of this figure shows typical temperatures and densities of UNPs. The shaded pink area in the upper right-hand portion of this figure shows the approximate region of HEDP considered in this review. The blue shaded ellipse indicates the area of warm dense matter²⁵ (WDM), corresponding to $\Gamma \sim 1$ and $k_B T_e \sim E_F$.

$$\Theta = \frac{k_B T}{E_F}, \quad (11)$$

becomes small and the pressure is then dominated by the Fermi pressure of the partially degenerate electrons.

The physical properties of the plasma vary greatly across the range of temperatures and densities shown. In particular, the Coulomb coupling can vary greatly.^{26–28} For particles with a single temperature T , the gray lines indicate $\Gamma = 0.1, 1.0,$ and 10 when $Z = 1$. For plasma mixtures,^{29,30} it is sometimes necessary to consider the species Coulomb coupling parameter, generalized from Eq. (2) as

$$\Gamma_{ij} = \frac{Z_i Z_j e^2}{(4\pi\epsilon_0) a_{ij} K_{ij}}, \quad (12)$$

where Z_i is the effective charge of species i , a_{ij} is an estimate of the average interparticle separation of species i and j ,

$$a_{ij} = \left(\frac{3}{4\pi \frac{n_i + n_j}{2}} \right)^{1/3}, \quad (13)$$

and K_{ij} is an estimate of the kinetic energy of the i - j pair.³¹ For coupling parameters that involve the electrons (i.e., Γ_{ee} and Γ_{ei}), a quantum estimate is needed for the kinetic energy, and these are shown as gray contours in Fig. 2. Note that the electronic couplings “decrease” for very high density because the electron kinetic energy is given by the Fermi energy, and the coupling parameter of Eq. (2) becomes $\Gamma = (e^2/4\pi\epsilon_0 a_{ws})/E_F \propto n^{-1/3}$.

In addition to the theoretical treatments given in Secs. II–IV, many additional theoretical approaches are used to describe HEDP systems. These include quasilocalized charge approximation,^{32,33} density-functional theory,³⁴ *ab initio* simulations,^{35,36} molecular dynamics (MD) simulations, and many others.³¹

B. Overview of UNP physics

Two excellent review articles covering the essentials of UNPs have been written.^{17,18} Only a brief overview will be given here. The temperatures and densities for UNPs are far below what is required for ionization in equilibrium. However, because UNPs are out of equilibrium and because UNP experiments study transient phenomena, the electrons and ions do not recombine at these ultracold temperatures.

Generally speaking, UNPs are created by photo-ionizing cold atoms or molecules. The initial neutral particle temperature is subkelvin. The atoms and molecules are photoionized near resonance. In the atom experiments, neutral atoms are laser-cooled and held in a magneto-optical trap (MOT).³⁷ In the molecule experiments, neutral molecules in a skimmed supersonic jet are excited to Rydberg states that subsequently ionize due to collisions.³⁸ Atoms have also been used for Rydberg/plasma experiments^{39–41} and in some cases recombination is important.^{42–46} In this review, the plasma ions are singly ionized. Typical plasma densities are 10^7 to 10^{12} cm^{-3} . Typical plasma sizes range from 0.3 to 5 mm. Typical values of Γ are near 2 , with some experiments ranging down to 0.1 and up to 11 .⁴⁷

The electron and ion temperatures usually differ by an order of magnitude or more. The ion temperature is usually limited by disorder-induced heating (DIH), discussed in a moment. The electron temperature T_e is selected by choosing the wavelength of the ionizing laser (for atoms) or by selecting the initial Rydberg level (for molecules). Typical values range from $T_e = 1$ to 500 K. The lower temperature limit is set by three-body recombination,^{48–51} which simultaneously depletes the plasma density and heats the remaining electrons. In principle, there is no limit on the upper temperature although higher electron temperatures lead to greater charge imbalance.

The ions initially retain the millikelvin temperatures of the neutral atoms and molecules. However, the ion temperature rapidly increases because of disorder-induced heating.^{11,52–54} This occurs because there is no spatial correlation in the initial distribution of the thermal atomic cloud. After ionization, the potential energy landscape immediately hardens because the ions repel each other.⁵⁵ The resulting excess potential energy is converted to kinetic energy over the time scale of a few ion plasma periods, $(\omega_p^{(i)})^{-1}$, where $\omega_p^{(i)} = [n_i e^2 / (m_i \epsilon_0)]^{1/2}$ is the ion plasma frequency, as the ions thermalize. Another way to phrase this is to say that the ion-ion pair distribution function is initially flat in the instant after ionization. As this completely disordered system thermalizes, the pair distribution function develops a “hole” at $r = 0$. The energy required to generate this new pair distribution function, one with lower nearest-neighbor electrical potential energy, is deposited into thermal energy of the ions. This process is called disorder-induced heating (DIH).

The majority of UNP experiments measure the spatial density distribution of the ions in the plasma, the ion velocity distribution, the electron temperature, or some combination of these quantities.^{17,18} These are probed using fluorescence or absorption imaging, laser-induced fluorescence (single-channel) measurements, radio frequency radiation absorption, and electron or ion particle detection.

For a singly ionized plasma, when the electron temperature is not too low, the ions equilibrate at the disorder-induced heating temperature,

$$T_{\text{DIH}} = \frac{e^2}{4\pi\epsilon_0 k_B a_{\text{ws}}} \frac{1}{2.3}, \quad (14)$$

where the factor 2.3 is found in both molecular dynamics (MD) simulations and experiments.^{56,57} This corresponds to a value of the unscreened ion-ion strong coupling parameter of $\Gamma_{ii} = 2.3$. Electron screening contributes to lower ion temperatures, but also smaller nearest-neighbor potential energy. In Secs. V and VI, we describe experiments with higher values of Γ_{ii} .

The resulting plasmas are charge-neutral, but unconfined. The electron pressure causes them to expand due to the ambipolar field, with a local acceleration given by

$$a_a = -\frac{k_B T_e}{m_i} \frac{\nabla n(\vec{r}, t)}{n(\vec{r}, t)}, \quad (15)$$

where $n(\vec{r}, t)$ is the plasma density. For plasmas with a Gaussian spatial density distribution and a single species of ions, the expansion is self-similar and the density distribution remains Gaussian.

The DIH process in UNPs was “discovered” when the time-dependent ion temperature was measured.⁵² If the ions had retained the millikelvin temperature of the neutral atoms, the strong-coupling parameter would have been $\Gamma > 200$. However, disorder-induced heating increased the ion temperature to the value given in Eq. (14). Prior to this work, MD simulations had observed DIH as kinetic energy oscillations in the ions,^{58–61} but without an interpretation.⁵⁵

Disorder-induced heating provides a few examples of how UNP measurements have informed HEDP experiments. X-ray diffraction measurements in laser-driven graphite failed to find any evidence of crystalline order.⁶² Wigner crystallization⁵ should appear when $\Gamma \geq 171.8$, and the authors estimated Γ in their experiment to be several thousand. However, when DIH is considered, in this case due to the mismatch between the honeycomb structure of graphite and the hexagonal-close-pack structure of an equilibrium strongly coupled plasma, the strong coupling parameter was calculated to be 50—well below the crystallization limit.⁶³

The DIH process has been described as an interaction quench, and UNP measurements have shown that this is a universal behavior of Yukawa-screened systems.⁵⁶ In addition to these examples, UNP measurements have been used to confirm determination of self-diffusion from MD simulations originally designed to simulate HEDP systems.⁶⁴

C. Comments on Fermi degeneracy

As we have shown in Figs. 1 and 2, HEDPs and UNPs share features of strong ion coupling ($\Gamma = 1$ –10) and charge neutrality when we limit our discussion of HEDP systems to the upper right-hand corner of Fig. 2. Fermi degeneracy in these HEDP systems further strengthens this similarity. Degeneracy in HEDPs blocks recombination and weakens the electron-ion and electron-electron coupling. As a result, these plasmas exist as an ionized state of matter at equilibrium with well-defined thermodynamic properties such as an equation of state. This can be contrasted with UNPs, which are described with classical mechanics. The UNPs exist in a transient state far from equilibrium. The low plasma density and high electron temperature

typically make $\Gamma_{ee} \ll 1$ and $\Gamma_{ei} \ll 1$. This, together with the short time scales of the UNP experiments, makes recombination negligible. Therefore, the UNPs also exist in a quasiequilibrium state with well-defined thermodynamic properties.

II. MEAN FORCE KINETIC THEORY APPLIED TO TRANSPORT CALCULATIONS

In this section, we describe a recent example highlighting the synergy between HEDP and UNP science. We discuss a method to extend plasma transport calculations into the strongly coupled plasma regime, with $\Gamma \leq 20$. We show comparisons of transport coefficients calculated using this theory with measurements in UNP experiments. We also apply this theory to ion transport in more complex high energy density plasmas.

A. Mean force kinetic theory

Traditional plasma kinetic theories are based on either a low density or weak interaction expansion. The low density expansion leads to the Boltzmann equation.⁶⁵ However, the Boltzmann equation diverges when applied to the Coulomb interaction because it misses the many-body effect of screening. This shortcoming is resolved by making use of the weak coupling approximation, $\Gamma \ll 1$, whereby the Coulomb force is “limited” to act only within a Debye length. Alternatively, the weak interaction approximation leads to linear response theory and the Lenard-Balescu kinetic equation.^{66,67} This approach captures Debye screening in the weak interaction limit, but also diverges when applied to a plasma because it neglects strong short-ranged interactions. The shortcoming is again resolved by making use of the weak coupling approximation by limiting short-range interactions to the distance of closest approach in a binary collision.

Neither the low density nor weak interaction expansion parameters appear applicable to strongly coupled plasmas, where these approximations are not valid. Many papers have been published that extend kinetic theories into the strongly coupled regime (see, for example, Refs. 68–71 and many others).

In 2013, Baalrud and Daligault proposed an effective potential theory that postulated that the Boltzmann equation-based approach can be extended to stronger coupling by treating the dynamics of binary interactions as occurring via the potential of mean force, rather than the Coulomb potential.^{72,73} Other effective potentials have been proposed in the past (cf. Ref. 74). The YOCP presented in the Introduction is itself an effective potential for ion-ion interactions and is a weak-interaction limiting case of the potential of mean force.

The potential of mean force is the potential associated with the force between n particles in a system obtained when holding those n particles at fixed positions and canonically averaging over all possible configurations of the other $N-n$ particles at equilibrium (see, for example, Ref. 75). For a binary interaction, $n = 2$, the potential of mean force is simply related to the radial density distribution function,

$$w^{(2)}(r) = -k_B T \ln [g(r)], \quad (16)$$

for a uniform-density plasma.

The postulate underlying this approach is that although only two particles are considered in the dynamics of the interaction, important aspects of many-body physics are captured by the potential of mean force. This was found to lead to an accurate extension of plasma

kinetic theory into the strongly coupled regime.^{76–78} Whereas the traditional Landau-Spitzer theory breaks down when $\Gamma \gtrsim 0.1$, the effective potential approach was found to be accurate for $\Gamma \lesssim 20$. As shown in Fig. 1, this covers the regime of coupling strength most relevant to both HEDP and UNP experiments.

More recently, this approach has been formalized and extended by showing that it can be derived from a single expansion parameter⁷⁹ that ensures that the exact equilibrium limit is maintained at all orders of the Bogolyubov-Born-Green-Kirkwood-Yvon (BBGKY) hierarchy. This differs from either of the traditional expansion parameters, which do not treat the spatial component of the distribution function at equilibrium. The effective-potential expansion parameter is

$$\Delta f^{(n+1)} \equiv f^{(n+1)} - \frac{f_o^{(n+1)}}{f_o^{(n)}} f^{(n)}, \quad (17)$$

where $f^{(n)}$ is the reduced distribution function,

$$f^{(n)}(\mathbf{r}^n, \mathbf{v}^n, t) = \frac{N!}{(N-n)!} \int d\Gamma^{(N-n)} f^{[N]}(\mathbf{r}^N, \mathbf{v}^N, t), \quad (18)$$

and $f^{[N]}$ is the exact N -particle distribution function. Here, $\mathbf{r}^N = (\mathbf{r}_1, \mathbf{r}_2, \dots, \mathbf{r}_N)$, where \mathbf{r}_i denotes the spatial location of particle i , $d\Gamma_n \equiv d\mathbf{r}_n d\mathbf{v}_n$ is a shorthand notation for the 6-dimensional phase-space, and $d\Gamma^{(N-n)} \equiv d\Gamma_{n+1}, \dots, d\Gamma_N$. Equation (17) represents a measure of the perturbation of the distribution function about equilibrium,

$$f_o^{(n)}(\mathbf{r}^n, \mathbf{v}^n) = \rho^{(n)}(\mathbf{r}^n) f_M^{(n)}(\mathbf{v}^n), \quad (19)$$

where

$$f_M^{(n)}(\mathbf{v}^n) = \left(\frac{m}{2\pi k_B T} \right)^{3n/2} \exp \left(- \sum_{i=1}^n \frac{m \mathbf{v}_i^2}{2k_B T} \right) \quad (20)$$

is the Maxwellian velocity distribution function,

$$\rho^{(n)}(\mathbf{r}^n) = \frac{N!}{(N-n)! \mathcal{Z}_N} \int d\mathbf{r}^{(N-n)} e^{-(V_{\text{ext}} + V_N)/k_B T} \quad (21)$$

is the n -particle density distribution function, $V_N(\mathbf{r}^N) = \sum_{i=1}^N \sum_{j>i}^N \phi(r_{ij})$ is the electrostatic potential energy, $V_{\text{ext}}(\mathbf{r}^N) = \sum_{i=1}^N \phi_{\text{ext}}(\mathbf{r}_i)$ is the interaction energy with the external potential ϕ_{ext} , and $\mathcal{Z}_N = \int \exp[-(V_{\text{ext}} + V_N)/k_B T] d\mathbf{r}^N$ is the configurational integral. The closure in Eq. (17) may be contrasted with the expansion parameter $f^{(n+1)}$, which is used to derive the Boltzmann equation.⁶⁵

The BBGKY hierarchy can be rearranged in a way so as to express Eq. (17) as the expansion parameter,

$$\left[\frac{\partial}{\partial t} + \sum_{i=1}^n (\mathcal{L}_i + \bar{\mathcal{L}}_i^{(n)}) \right] f^{(n)} = - \sum_{i=1}^n \int d\Gamma_{n+1} \mathcal{L}_{i,n+1}^C \Delta f^{(n+1)}. \quad (22)$$

Here, $\mathcal{L}_i = \mathbf{v}_i \cdot \partial / \partial \mathbf{r}_i + (q_i/m_i)(\mathbf{v}_i \times \mathbf{B}) \cdot \partial / \partial \mathbf{v}_i$, and

$$\bar{\mathcal{L}}_i^{(n)} \equiv \frac{1}{m_i} \bar{\mathbf{F}}_i^{(n)}(\mathbf{r}^n) \cdot \frac{\partial}{\partial \mathbf{v}_i} \quad (23)$$

is an operator associated with the mean force

$$\bar{\mathbf{F}}_i^{(n)}(\mathbf{r}^n) = -\nabla_i w^{(n)}(\mathbf{r}^n), \quad (24)$$

where the potential of mean force is

$$w^{(n)}(\mathbf{r}^n) = -k_B T \ln \left[\frac{\rho^{(n)}(\mathbf{r}^n)}{\rho^n} \right], \quad (25)$$

and $\rho = \lim_{V \rightarrow \infty} \int_V d\mathbf{r} \rho^{(1)}(\mathbf{r})/V$ is the average particle density and V is the volume of the plasma. If the plasma is uniform, i.e., there is no external potential, $\phi_{\text{ext}} \equiv 0$, $w^{(n)}(\mathbf{r}^n) = -k_B T \ln g^{(n)}(\mathbf{r}^n)$, where $g^{(n)}(\mathbf{r}^n) = \rho^{(n)}(\mathbf{r}^n)/\rho^n$ is the n -particle distribution function [when $\phi_{\text{ext}} \neq 0$, $g^{(n)}(\mathbf{r}^n) = \rho^{(n)}(\mathbf{r}^n)/\prod_{i=1}^n \rho^{(1)}(\mathbf{r}_i)$].

In principle, a kinetic theory can be obtained by taking $\Delta f^{(n+1)} = 0$ at any chosen order. With this, Eq. (22) reduces to a dynamical equation for $f^{(n)}$ in which n particles interact via the mean force $w^{(n)}$. In Ref. 79, this calculation has been carried out for $n = 2$. The result is a kinetic equation that is similar to the Boltzmann equation, but with three important extensions.

First, the collision cross section that arises in the collision operator is associated with a binary interaction of particles interacting via the potential of mean force $w^{(2)}$ rather than the bare Coulomb potential ϕ . The potential of mean force includes the exact screening due to surrounding particles at equilibrium. However, the theory is not yet closed in the sense that this depends on the two-particle density $\rho^{(2)}$ or, since the plasma is uniform at the small scale of the collision volume, the radial distribution function $g(r)$. Fortunately, accurate approximations exist for modeling $g(r)$ that are very computationally efficient to evaluate. Examples include the hypernetted chain approximation (HNC) in classical plasmas⁸⁰ as well as quantum HNC extensions in HEDP.⁸¹ Any such model may be used to provide the input to the theory. A couple of examples are illustrated in Secs. II B–II D.

Second, the molecular chaos approximation that is typically used in the derivation of the Boltzmann equation is somewhat relaxed by utilizing a version of Enskog's kinetic theory.^{82,83} This models the statistical excluded volume that surrounds charged particles interacting via a repulsive potential. It leads to a slight increase (usually 20%–40%) in the collision frequency for $\Gamma \gtrsim 1$. The effective diameter of particles is determined from $g(r)$ in this model and the increase in the collision rate through a matching with Enskog's equation of state.⁸² These first two aspects provided a derivation of the collision operator that was postulated in Refs. 72 and 82.

Third, the recent formal derivation from Ref. 79 has revealed that, in addition to the collision operator, the mean force contributes to the convective derivative term of the kinetic equation (commonly referred to as the left hand side). Specifically, this term can be written as the gradient of a second-rank tensor $\bar{\mathbf{F}}_1^{(1)} = -(\nabla_1 \cdot \mathcal{P}_\Phi)/[\rho^{(1)}(\mathbf{r}_1)]$, where

$$\mathcal{P}_\Phi = -\frac{1}{2} \int d\mathbf{r} \mathbf{r} \mathbf{r} \frac{\phi'(r)}{r} \int_0^1 d\mu \rho^{(2)}(\mathbf{r}_1 - (1-\mu)\mathbf{r}, \mathbf{r}_1 + \mu\mathbf{r}). \quad (26)$$

Here, $\mathbf{r} \equiv \mathbf{r}_2 - \mathbf{r}_1$ and $\phi'(r) \equiv d\phi/dr$. In the common limit that the density gradient of the background plasma is small over the spatial scale of the two-body correlations, this can be expressed as the gradient of a scalar $\nabla_1 \rho_\Phi$, where

$$\rho_\Phi = -\frac{\rho^2}{6} \int_0^\infty d\mathbf{r} \phi'(r) r g(r) \quad (27)$$

is the standard expression for the potential component of the scalar pressure from classical statistical thermodynamics.⁸⁰ Taking moments

of the kinetic equation reveals that this mean force contribution captures the exact potential contribution to the equation of state properties in the pressure, internal energy, and heat flux terms, near equilibrium.⁷⁹

By applying the Chapman-Enskog (CE) method,⁸⁶ the mean force kinetic theory predicts both the transport coefficients and equation of state properties for the hydrodynamic, or magnetohydrodynamic, description of the macroscopic evolution of the plasma. The input to the theory is the appropriate radial distribution functions, which determine the potential of mean force associated with the interaction between each species in the plasma.

B. Ion transport

This section describes an example of how comparison with UNP experiments contributed to validating this theory for ion transport in HEDP systems. Several ion transport properties have been studied now, including diffusion,^{72,77,87} viscosity,⁷⁶ temperature anisotropy relaxation,⁷⁸ and stopping power.^{88–93} For illustration, we focus here on self-diffusion. Figure 3 shows a comparison of the theory with a series of simulations and experiments for systems that become increasingly more complex from left to right.

The left panel shows a comparison of the self-diffusion coefficient calculated using the effective potential theory with MD simulations of a one-component plasma (OCP). Molecular dynamics simulation results were obtained over a broad range of Coulomb coupling conditions, ranging from weak coupling where the Landau-Spitzer theory is valid ($\Gamma \lesssim 0.1$) up to solidification at $\Gamma = 171.8$. The comparison shows that the theory agrees well with the MD simulations well into the strongly coupled regime, extending the traditional theory up to Γ values near 20. Molecular dynamics is a first-principles solution of Newton's equations of motion for this system, so this comparison certainly lends confidence to the theory, but validation must come from experiment.

The middle panel of Fig. 3 compares the theoretical calculation and MD simulations with measurements of the ion self-diffusion coefficient in a UNP.⁶⁴ In this experiment, the electrons were much hotter than the ions so that the screening parameter was estimated to lie in

the range $\kappa \equiv a/\lambda_D \approx 0.1 - 0.6$. For this reason, ion dynamics is expected to be accurately represented by the OCP model. Both the MD and theoretical predictions agree with the experimental data within measurement error. The data are accurate enough to exclude a simple model where the force between interacting particles is modeled using a Debye-Hückel potential.^{94,95} A comparison with experimental measurements of velocity relaxation⁹⁶ in a UNP showed similar agreement in the same range of conditions.⁷² These measurements provide rigorous tests with sufficient resolution to distinguish between competing models.

Transitioning from ultracold to high energy density plasma requires treating electron degeneracy in the theory. Although ion dynamics are expected to obey classical physics, degenerate electrons participate in screening the ions. Quantum effects, such as pressure ionization, are also essential to determining the average charge state of the system. In the mean force theory, this influences the ion-ion radial distribution function $g_{ii}(r)$ that is required as input to the theory. Since this quantity is related to the equation of state properties, much work has been devoted to modeling it. The right panel of Fig. 3 shows the results obtained by using one such model, called the average-atom two-component plasma model,^{81,97} to provide the ion-ion radial distribution function used as input to the mean force theory.⁸⁵ Results are compared with a variety of sophisticated quantum molecular dynamics simulations for aluminum at solid density and ten times compressed, over a range of temperatures spanning the warm dense matter (WDM) regime (see Fig. 2). The average ion charge state at these conditions ranges from $\bar{Z} = 3$ to 12, the effective ion coupling parameter from $\Gamma \approx 72$ to 2, and the electron degeneracy parameter from $\Theta = k_B T/E_F = 0.05$ to 17.

The good agreement shows that the theory accurately models ion transport in warm dense matter, in comparison to models that are considered to be essentially first principles calculations. The theory provides insights into the relevant physical processes influencing ion transport. It also provides a practical utility in that the computations are computationally inexpensive, being done on a laptop in a matter of minutes, whereas the quantum molecular dynamics simulations require high-performance computing resources, and even become

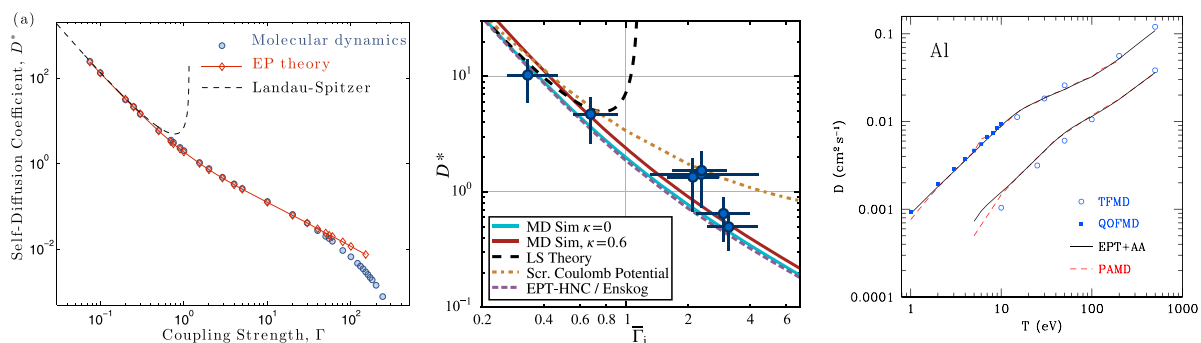


FIG. 3. Left: Comparison of the self-diffusion coefficient of the OCP computed from MD simulations (circles) and effective potential theory (diamonds). Reproduced with permission from Baalrud and Daligault, AIP Conf. Proc. **1786**, 130001 (2016). Copyright 2016 AIP Publishing LLC.⁸⁴ Middle: Comparison of the self-diffusion coefficient⁶⁴ measured in an UNP experiment (circles) with the effective potential theory and MD simulations. Reproduced with permission from Strickler *et al.*, Phys. Rev. X **6**, 021021 (2016). Copyright 2016 American Physical Society. Right: Comparison of the self-diffusion coefficient of aluminum at a density of 2.7 g/cm^3 (top) and 27 g/cm^3 (bottom) computed from Thomas-Fermi molecular dynamics (hollow circles), quantum orbital free molecular dynamics (filled circles), pseudoatom molecular dynamics (dashed line) and effective potential theory using the average atom two-component model for $g_{ii}(r)$ (solid lines).⁸⁵ Reproduced with permission from Daligault *et al.*, Phys. Rev. Lett. **116**, 075002 (2016). Copyright 2016 American Physical Society.

impossible at the higher temperature regime. Computational efficiency makes it possible to consider incorporating the theory into fluid codes used to model HEDP systems, or to make tables of transport coefficients to be used in those codes.

C. Electron-ion transport

As described above, electron-ion transport processes in UNPs and HEDPs have a fundamental difference regarding the electron statistics. Nevertheless, the aspect of collisions between moderately coupled electrons and strongly coupled ions is common to both systems, and studying this process in UNPs can lead to insights into HEDP transport. We have recently shown that the electron-ion collision rate is influenced by a charge-sign asymmetry that is not predicted by previous theories of weakly or strongly coupled plasmas.⁹⁸ Traditional theories obey a symmetry property that the collision rate is invariant with respect to the sign of the charges involved. That is, it predicts an identical collision rate for an electron-ion interaction as for a positron-ion interaction. The recent work shows that this symmetry is broken at moderate-to-strong Coulomb coupling. This is called the “Barkas effect” in analogy to a similar charge-sign asymmetry that has been observed in the slowing of charged particles in particle physics.⁹⁹

Figure 4 shows an example from classical MD simulations demonstrating that the electron-ion collision rate is substantially higher than the positron-ion collision rate when the electron coupling strength is moderate ($\Gamma_e \gtrsim 0.2$). The solid lines show that the mean force kinetic theory accurately captures the effect. It can be explained as arising from the way screening influences the interaction force. The Rutherford scattering cross section, which is based on the bare Coulomb potential, does not have this property, and it is not captured by the usual methods of limiting the range of interactions to be a certain screening length.¹⁰⁰ It is also not captured by linear response theory because it is a nonlinear effect associated with close collisions.¹⁰⁰

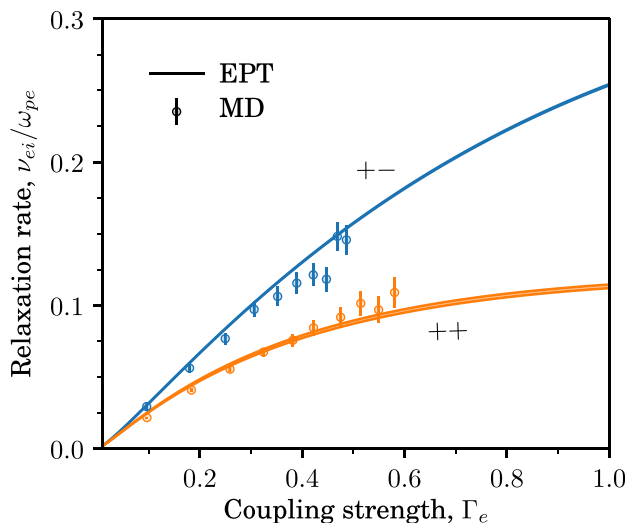


FIG. 4. Comparison of the electron-ion (blue) and positron-ion (orange) momentum relaxation rate obtained from MD simulations (circles) and effective potential theory calculations (lines).⁹⁸ The ion coupling strength is $\Gamma_i = 1$. Reproduced with permission Shaffer and Baalrud, *Phys. Plasmas* **26**, 032110 (2019). Copyright 2019 AIP Publishing LLC.

The charge sign asymmetry demonstrates that it is the effective interaction force itself that is modified by screening.

Several developments were necessary to obtain this result. These included developing numerical methods to conduct classical MD simulations of electron-ion transport properties at conditions for which they recombine¹⁰¹ as well as a model for the electron-ion radial distribution function in a nonequilibrium plasma with differing electron and ion temperatures.^{31,102–105} There are hints that this effect may be present in measurements of electron-ion collisions in UNPs,^{106,107} but it has not yet been possible to isolate and test the predictions experimentally (see Sec. VII D). Although analysis to date has considered classical statistics, the effect is expected to also carry over to weakly degenerate electrons in HEDP systems.⁹⁸

D. Magnetized plasmas

Understanding the transport properties of magnetized plasmas that are in or near the strong coupling regime is another area in which UNPs may contribute to advancing HEDP science. Some of the most interesting recent trends in HEDP science, such as magnetized inertial confinement fusion,¹⁰⁸ are enabled by focusing particle and energy transport using applied magnetic fields. In HEDP experiments, the fields are typically enormous, approaching 10^4 T. We have recently made the point that UNPs lie in a unique position of parameter space in which both magnetization and strong coupling physics can, potentially, be accessed simultaneously at modest magnetic field strengths.¹⁰⁹ For example, the magnetization regime relevant to electrons at HEDP conditions requires a magnetic field near 10^4 T, whereas the same physical processes can be accessed in a UNP at a much more modest 10^{-3} T. This, coupled with the sensitivity characteristic of UNP measurements, presents the possibility of significant crossover¹¹⁰ (see also Sec. VII). Recent work has investigated an example of this potential using MD simulations, where it was shown that a strongly magnetized UNP is expected to develop a large temperature anisotropy because magnetization dramatically slows disorder induced heating perpendicular to the field.¹¹¹ This may provide an avenue to access energy relaxation processes at conditions of strong coupling and magnetization. Much recent work has presented MD simulations of transport in the magnetized OCP or YOCP, including diffusion,¹¹² heat conductivity,¹¹³ and temperature anisotropy relaxation.¹¹⁴

III. IONIC TRANSPORT CALCULATIONS IN NONIDEAL PLASMAS USING AN EFFECTIVE BOLTZMANN EQUATION

In this section, we describe an effective Boltzmann approach to calculating ion transport in strongly coupled plasmas. The large-impact-parameter divergence is eliminated by incorporating many-body effects into the Boltzmann equation directly. We show that this leads to a Yukawa-type ion interaction and give a physically motivated representation of the screening length. The goal of the effective Boltzmann equation approach is to generate ionic transport coefficients that do not rely on Coulomb logarithms, in favor of numerically generated cross sections. The model has been validated with MD across the moderately coupled regime, and the fits are extremely easy to implement into hydrodynamic modeling codes with essentially zero computational cost.^{115–119} The de Broglie wavelength of ions in the plasmas we are considering is negligibly small [see Figs. 1 and 2 and

Eqs. (10) and (11)], and we therefore implement a classical approach for ion transport.

This approach is complementary to the presentation of Sec. II. In that section, we described a kinetic theory that uses the potential of mean force to calculate plasma transport in the strongly coupled plasma regime with $\Gamma \leq 20$. There we presented encouraging comparisons between this theory and MD simulations, UNP measurements, and other approaches. In the weakly coupled limit, $\Gamma \ll 1$, the potential of mean force reduces to the Yukawa potential of Eq. (1).

Transport processes in hydrodynamic equations are typically described using linearized flux models. The leading order coefficient associated with each process is known as a “transport coefficient.” While the underlying symmetries of a given system will determine the general form of hydrodynamic equations, the actual transport coefficients (along with any equation of state information) must be determined by the microphysics at the particle scale. For this reason, there are several approaches to calculate transport coefficients, each of which requires connecting microphysics processes to a particular hydrodynamic model. Molecular dynamics simulations are, of course, used to calculate the evolution of particle trajectories, distribution functions, and transport coefficients. However, solutions that are less computationally intense are helpful. Calculations of transport coefficients fall into two main branches.¹²⁰ The first branch begins with a hydrodynamic model determined by symmetries and conservation laws, where microphysics calculations are used to determine the transport coefficients. Meanwhile, the second branch uses a kinetic equation to derive a hydrodynamic model and connects transport coefficients to microphysics quantities in the process. This section, as does Sec. II, pursues this latter approach.

A. Boltzmann equation

When using a kinetic equation to derive transport coefficients, the choice in the equation is not unique. Most approximations made in the collision operator are of two types, either binary-collision approximations are used (Boltzmann equation), which handle strong collisions well using a cross section, or correlation expansions are used (Lenard-Balescu equation), which include many-body physics but in the weak-scattering limit. Here, we aim to exploit both avenues via the use of an effective potential, motivated by the Lenard-Balescu equation, in a numerically computed cross section from the Boltzmann equation. The effective potential used here will be a Yukawa-screened Coulomb interaction, with a physically motivated screening length. This is an alternative to the method used in Sec. II, where the effective potential was derived from thermodynamic considerations.

The Boltzmann kinetic equation was originally designed for gaseous mixtures that are well-described by binary collisions, so the application of this model to plasmas can unfortunately introduce mathematical divergences due to the long-range nature of Coulomb interactions. An “effective” Boltzmann approach is thus required,^{89,94,121,122} in which strong scattering physics is built into a cross section numerically by capturing long-range screening effects through an effective potential. Such an approach yields a convergent kinetic model for the subsequent transport coefficients derived for the hydrodynamic description of a dense plasma. This effective Boltzmann approach is described through a set of coupled Boltzmann equations for each species j of the form

$$\frac{\partial f_j}{\partial t} + \mathbf{v} \cdot \nabla f_j + \frac{1}{m_j} \mathbf{F}_j^{\text{ext}} \cdot \nabla f_j = \sum_l C_{jl}[f_j, f_l], \quad (28)$$

$$C_{jl}[f_j, f_l] = \iint d\tilde{\mathbf{v}} d\Omega g I(g, \theta) (\tilde{f}_j \tilde{f}_l - f_j f_l). \quad (29)$$

Here, $\mathbf{F}_j^{\text{ext}}$ is any external force, $g = |\mathbf{v} - \tilde{\mathbf{v}}|$ is the relative velocity, Ω is the solid angle, the tildes denote functions of $\tilde{\mathbf{v}}$, and the differential cross section is defined as

$$I(g, \theta) = \frac{b}{\sin(\theta)} \frac{db}{d\theta}, \quad (30)$$

for an impact parameter b . Strong scattering is well described in this model through the cross section, which is only a well-defined quantity for binary collisions where the initial and final states are distinct and separated. Note that the time evolution of the scattering event does not appear in Boltzmann descriptions. For example, if $\mathbf{F}_j^{\text{ext}}$ were to include a Vlasov-type contribution, the resulting dynamical fluctuations could not modify the cross section in any simple way.

B. Transport coefficients

Within the binary approximation, a pair interaction $u_{ij}(r)$ between particles of species i and j must be chosen. Given this scheme, it remains to generate the relevant coefficients. The standard procedure¹²³ is the Chapman-Enskog (CE) expansion, which yields a solution of Eq. (28) that can be used to construct hydrodynamic moments and, importantly, closed form expressions for the fluxes associated with these moments. This method proceeds by using a method of successive approximations for the distribution functions f_j ,

$$f_j = \frac{1}{\epsilon} f_j^{(0)} + f_j^{(1)} + \epsilon f_j^{(2)} + \dots, \quad (31)$$

where ϵ is an ordering parameter. The lowest-order solution $f^{(0)}$ can be shown to be a local, drifting Maxwellian. In turn, higher order corrections can be systematically obtained by substituting the full CE expansion of Eq. (31) into the Boltzmann equations, Eq. (28). From the relevant fluxes computed using the solution Eq. (31), leading order expressions for the transport coefficients can be obtained.

Within a classical approximation, the scattering angle between the collision of two particles can be calculated as

$$\theta_{ij}(b, v) = \pi - 2b \int_{r_0}^{\infty} \frac{dr}{r^2 \sqrt{1 - \left(\frac{b}{r}\right)^2 - \frac{2}{\mu_{ij} v^2} u_{ij}(r)}}, \quad (32)$$

where b is the impact parameter of the collision, v is the relative velocity between the particles, and the reduced mass is given by $\mu_{ij} = m_i m_j / (m_i + m_j)$, with m_k being the mass of the k th particle. The lower limit of integration r_0 is the distance of closest approach, which is the largest root of the equation,

$$1 - \left(\frac{b}{r_0}\right)^2 - \frac{2}{\mu_{ij} v^2} u_{ij}(r_0) = 0. \quad (33)$$

Once this integral is evaluated, the scattering angle can be used to calculate the momentum-transfer cross sections

$$\sigma_{ij}^{(n)}(v) = 2\pi \int_0^\infty db b [1 - \cos^n(\theta_{ij}(b, v))]. \quad (34)$$

For first-order Chapman-Enskog (CE) theory, only the values $n = \{1, 2\}$ are needed. Finally, the relevant collision integrals are given by

$$\Omega_{ij}^{(n,m)} = \left(\frac{T}{2\pi\mu_{ij}}\right)^{1/2} \int_0^\infty dV e^{-V^2} V^{2m+3} \sigma_{ij}^{(n)}(V), \quad (35)$$

$$V^2 = \frac{\mu_{ij}v^2}{2k_B T}, \quad m = \{1, 2, 3\}. \quad (36)$$

C. Coulomb logarithms

The simplest model for a plasma is to neglect many-body effects and to take the entire interaction between two particles with charges $Z_i e$ and $Z_j e$ as the bare Coulomb potential,

$$u_{ij}(r) = \frac{Z_i Z_j e^2}{4\pi\epsilon_0 r}, \quad (37)$$

where each charge is either the bare nuclear charge or the mean ionization state. The relevant scattering angle of this binary collision is then

$$\theta(b, v) \approx 2 \sin^{-1} \left(\frac{1}{\sqrt{1 + \epsilon^2 b^2}} \right), \quad \epsilon = \frac{4\pi\epsilon_0 \mu v^2}{Z_i Z_j e^2}. \quad (38)$$

If we then use Eq. (38) to calculate the momentum-transfer cross section, we encounter a divergence as $b \rightarrow \infty$ in Eq. (34). If this upper limit is instead truncated at some $b_{\max} = \lambda$, we obtain the finite cross sections for $n = 1$ as

$$\sigma(v) \approx \left(\frac{4\pi}{\epsilon^2}\right) \frac{1}{2} \ln(1 + \epsilon^2 \lambda^2). \quad (39)$$

Before moving on, we should understand what this approximation means physically. It should be emphasized that introducing a truncated range in the impact parameter is “not equivalent” to truncating the range of the Coulomb interaction. All particles with a sufficiently small impact parameter will interact throughout their “entire” trajectory, while the remaining particles will never interact with each other. Before Eq. (35) is used to calculate the collision integrals for binary, Coulomb interactions, it is common to make two “additional” approximations. First, the explicit velocity dependence of the logarithms in Eq. (39) is usually neglected and replaced by some thermal velocity

$$\sigma(v) \approx \frac{1}{2} \left(\frac{4\pi}{\epsilon^2}\right) \ln \left[1 + \left(\frac{8\pi\epsilon_0 k_B T \lambda}{Z_i Z_j e^2}\right)^2 \right]. \quad (40)$$

Next, weak coupling is also assumed in the argument of the logarithm to yield

$$\sigma(v) \approx \left(\frac{4\pi}{\epsilon^2}\right) \ln \Lambda, \quad \ln \Lambda \equiv \ln \left(\frac{8\pi\epsilon_0 k_B T \lambda}{Z_i Z_j e^2}\right). \quad (41)$$

The Coulomb logarithm (CL) in Eq. (41) is in the form $\ln \Lambda = \ln(b_{\max}/b_{\min})$, where $b_{\max} = \lambda$ and $b_{\min} = Z_i Z_j e^2 / (8\pi\epsilon_0 k_B T)$, but it can be negative for certain parameters. As the CL in Eq. (40) still

contains some information about the hyperbolic trajectories of the collisions (rather than straight line trajectories), positivity of the logarithm is maintained. Either form results in the following simple expression for the first-order collision integral:

$$\Omega_{wc}^{(11)} = \frac{\sqrt{\pi} Z_i^2 Z_j^2 e^4}{2(4\pi\epsilon_0)^2 \sqrt{2\mu(k_B T)^3}} \ln \Lambda. \quad (42)$$

However, each CL can introduce spurious and even pathological physics into the model. As already mentioned, the weak-coupling approximation seen in Eq. (41) can yield negative cross sections and thus negative collision integrals for sufficiently large values of the plasma parameter,

$$g = \frac{Z_i Z_j e^2}{4\pi\epsilon_0 \lambda k_B T} = \frac{a_{ws}}{\lambda} \Gamma, \quad (43)$$

such that $g > 2$. Second, the thermal approximation in Eq. (40), while always positive, lacks a velocity dependence in the logarithmic term that cannot be approximated with a constant value in the collision integrals even for $g \ll 1$. It can be seen that the thermal approximation is a “singular” perturbation to the collision integral; thus, there is a significant deviation from the Coulomb result for any finite g . Finally, CLs are often treated as transferable between different transport processes, which is clearly not justified by the physics.

D. Effective Boltzmann equation

As shown in Subsection III C, the use of the bare Coulomb interaction introduces a divergence to the cross section at a large impact parameter that is typically handled by introducing the uncontrolled approximation of a b_{\max} . We can instead resolve this issue by incorporating many-body effects into the Boltzmann equation in the spirit of the Lenard-Balescu equation. Rather than neglecting the three-body distribution function of a given species, we can approximate it as

$$f_3(\mathbf{r}_{1,2,3}, \mathbf{v}_{1,2,3}, t) \approx f_1(\mathbf{r}_3, \mathbf{v}_3, t) f_2(\mathbf{r}_{1,2}, \mathbf{v}_{1,2}, t), \quad (44)$$

where f_1 is the one-particle distribution function and f_2 is the pair distribution function of a given species. This allows particles at \mathbf{r}_1 and \mathbf{r}_2 to be strongly interacting but still weakly coupled to particles at \mathbf{r}_3 . Hence, we have maintained strong, binary scattering as well as many-body screening effects. Further, we can exploit the weak coupling between the self-consistent density and the interacting pair and employ linear response theory to express the density in terms of a response function and the external potential induced by the pair as

$$\int d\mathbf{v}_3 f_1(\mathbf{r}_3, \mathbf{v}_3, t) = n(\mathbf{r}_3, t) \approx \chi * v_{\text{ext}}. \quad (45)$$

The density-density response function can be made as complex as necessary; however, to minimize the parameter space, we can use the long-wave expansion in Fourier space

$$\chi^{-1}(k) \approx -v(k)(1 + \lambda^2 k^2 + \dots), \quad v(k) = \frac{4\pi}{k^2}. \quad (46)$$

The result is that the original Coulomb interaction is modified as

$$u_{ij}(r) = \frac{Z_i Z_j e^2}{4\pi\epsilon_0 r} e^{-r_{ij}/\lambda}, \quad (47)$$

which is none other than the screened Coulomb Yukawa potential of Eq. (1). Despite this seemingly simple modification, the calculation of the scattering angle, momentum transfer cross sections, and collision integrals can now only be obtained numerically.

E. Numerical fits

To facilitate the mathematics, we will introduce the dimensionless parameters,

$$\rho = \frac{b}{\lambda}, \quad \text{and} \quad w^2 = \frac{\mu\lambda 4\pi\epsilon_0}{2Z_i Z_j e^2} v^2. \quad (48)$$

The momentum-transfer cross sections now take the form

$$\sigma_{ij}^{(n)}(w, \lambda) = 2\pi\lambda^2 \phi_n(w), \quad (49)$$

$$\phi_n(w) = \int_0^\infty d\rho \rho [1 - \cos^n(\theta_{ij}(\rho, w))]. \quad (50)$$

Importantly, the cross section can now be fit in terms of the dimensionless velocity w , and we can construct a suitable fit that obeys the appropriate asymptotic limits. Similarly, the collision integrals can be expressed in terms of the transformed variables as

$$\Omega_{ij}^{(n,m)} = \sqrt{\frac{2\pi [Z_i Z_j e^2 / (4\pi\epsilon_0)]^2}{\mu_{ij} (k_B T)^{3/2}}} \mathcal{K}_{nm}(g), \quad (51)$$

$$\mathcal{K}_{nm}(g) \equiv g^m \int_0^\infty dw e^{-gw^2} w^{2m+3} \phi_n(w), \quad (52)$$

where we need only to generate a fit in terms of the dimensionless coupling parameter g defined in Eq. (43). Details of the numerical schemes and fitting functions for both Eqs. (50) and (52) can be found in Ref. 124. It is important to note that all macroscopic transport coefficients can now be obtained in terms of a microscopic screening length, λ , which is yet to be defined. A model that incorporates both the high-temperature limits and strong-coupling effects is given by

$$\lambda = \left[\frac{1}{\lambda_e^2} + \sum_{i=1}^N \frac{1}{\lambda_i^2} \left(\frac{1}{1 + 3\Gamma_i^{\text{IS}}} \right) \right]^{-1/2}, \quad (53)$$

where λ_e and λ_i are electron and ion screening lengths, respectively, and the ion-sphere coupling parameter is defined as

$$\Gamma_i^{\text{IS}} = \frac{(Z_i e)^2}{4\pi\epsilon_0 k_B T} \left(\frac{4\pi\rho_{\text{tot}}}{3Z_i e} \right)^{1/3}, \quad (54)$$

with ρ_{tot} being the total charge density. Molecular dynamics simulations have validated this choice in screening length model over a large range of coupling parameters. In fact, this model can be further generalized to include dynamic screening effects, which is necessary when calculating quantities such as stopping power.^{89–93}

F. Connection to UNPs

The foregoing treatment was developed with HEDP considerations in mind; however, this model can be applied to UNPs as well. While UNPs exist in a very different regime of the temperature-density space, the connection between the two states of matter is illuminated when examining them in terms of the plasma parameters Γ and κ ; as

shown in Fig. (1), a crossover between the two plasmas is seen for low Γ and κ . UNP experiments can thus be viewed as a proxy for HEDPs within these regimes and therefore be used to validate theoretical models. In particular, the uncertainties that remain in the HEDP community rely within transport in mixtures, nonstandard transport processes (thermal diffusion, barodiffusion, etc.), and kinetic effects at interfaces.¹²⁴ As a recent example of validating these transport coefficients, the above models have been tested with UNPs using momentum-transfer cross sections in a fluid code simulation for an expanding dual-species UNP of Ca^+ and Yb^+ ions,¹¹⁵ as seen in Sec. VIII. This provides another example of the synergy possible in the combination of HEDP and UNP science.

IV. NEW TRANSPORT MODELS IN THE ARES MULTIPHYSICS CODE

Plasma transport properties generated using kinetic calculations, such as those presented in Secs. II and III, or other sources, can be incorporated into large multiphysics radiation hydrodynamics codes to better understand the temperatures and densities in fusion-class plasmas. These calculations can be used to design and gain greater insights into these HEDP systems.¹²⁵

Multiphysics codes need to include many different physical processes. Radiative (bremsstrahlung, inverse bremsstrahlung, Compton scattering, radiation pressure, opacity, transport), atomic (photo-ionization, recombination), collisional (ionization, recombination, stopping power), and thermonuclear processes are all important.^{126–129} Source terms must also be included, both from external drivers and from internal thermonuclear ignition. In multispecies plasmas, low- Z species tend to be weakly coupled while higher Z species can be strongly coupled because of the Z^2 -dependence of the strong coupling parameter Γ .^{130,131} For ICF experiments, like the blue trace shown in Fig. 2, these processes need to be accurately and efficiently modeled across a wide range of parameter space.

In this section, we describe recent improvements to transport models in the Ares code developed at Lawrence Livermore National Lab.^{125,132,133} The code solves single-fluid multicomponent multivariate Navier-Stokes equations on a structured ALE (arbitrary Lagrangian-Eulerian) AMR (adaptive mesh refinement) grid. Ares offers a variety of physics packages, including radiation transport, laser ray trace and energy deposition, and thermonuclear burn to model high energy density systems including those created at the National Ignition Facility.

Recently, improved models for plasma viscosity and electron-ion temperature equilibration rates have been implemented in Ares. The new models build upon microphysics molecular dynamics simulations and analytic developments. In the case of plasma viscosity, we employ the effective Boltzmann technique of Sec. III to improve accuracy in the weak coupling regime and more accurately model multicomponent plasmas relative to one-component-plasma-based descriptions. For electron-ion coupling, we eliminate explicit choice of a Coulomb log by using an efficient approximation to a quantum Lenard-Balescu equilibration rate. We summarize the newly adopted models, compare against high-fidelity microphysics calculations, and quantify the modifications to the transport coefficients relative to existing models.

A. Plasma viscosity

Plasma viscosity and diffusion^{134,135} affect the development of turbulence in laser-driven ICF implosions. Because turbulence can

limit the development of high densities and temperatures in fusion-class plasmas, it is critical to model it accurately. Recent work has attracted interest in high resolution simulations of ICF implosions^{136,137} and the role of plasma viscosity in determining the spatial scale of those structures.¹³⁷ In the interest of accurately modeling these processes, an improved plasma viscosity model has recently been implemented. To span the parameters of interest, the new model is a hybrid of the Yukawa viscosity model (YVM), tailored to the warm dense matter regime and the effective Boltzmann model of Sec. III. The effective Boltzmann model more readily generalizes to the treatment of mixtures than the YVM, which requires representing the multicomponent plasma with a single effective coupling parameter Γ and Yukawa screening length κ . Here we present the hybrid model, compare the model against MD data for mixtures, and quantify the differences between the new and previous models for representative one- and multicomponent plasmas of interest.

In the strong coupling regime, Ares uses the Yukawa viscosity model (YVM) developed by Murillo.¹³⁸ In this model, the viscosity is given by a function Γ and κ as

$$\eta_{YVM}^*(\kappa, \Gamma) = 0.0051 \frac{\Gamma_m}{\Gamma} + 0.374 \frac{\Gamma}{\Gamma_m} + 0.022, \quad (55)$$

where Γ_m is the melt boundary approximated as

$$\Gamma_m(\kappa) = 171.8 + 82.8(e^{0.565\kappa^{1.38}} - 1), \quad (56)$$

$\eta^* = \eta/\eta_0$ is the viscosity normalized by the characteristic viscosity,

$$\eta_0(\kappa) = \sqrt{3}\omega_E(\kappa)m_i n a_i^2, \quad (57)$$

and the Einstein frequency ω_E is approximated as

$$\sqrt{3}\omega_E(\kappa) = \omega_p^{(i)} e^{-0.2\kappa^{1.62}}, \quad (58)$$

where $\omega_p^{(i)}$ is the ion plasma frequency. These approximations were chosen to yield accurate fits to molecular dynamics simulations of one-component plasmas. The molecular dynamics data used for the fits span coupling strengths in the range $\Gamma = 5-300$, making the model applicable to liquid metals and warm dense matter.

As the plasma transitions into the weakly coupled regime, for instance due to heating during an ICF implosion, the Yukawa viscosity model is no longer accurate and the weakly coupled plasma theory may be used instead. The previous plasma viscosity model in Ares used an extension the Yukawa viscosity model developed by Rudd,^{139,140} which we will refer to as eYVM, to recover the $\eta \sim T^{5/2}$ scaling in the weak coupling limit. However, more detailed models have now been adopted for the weak coupling regime.

In particular, Ares now calculates a weakly coupled plasma viscosity using the effective Boltzmann treatment developed by Stanton and Murillo¹²¹ and described in Sec. III. The viscosity is given by

$$\eta_{SM}^* = \frac{5\sqrt{3}}{36\Gamma^{5/2}K_{22}(g)}, \quad (59)$$

where K_{22} is the collision integral of Eq. (52) with a fit provided in Ref. 121, g is the plasma parameter of Eq. (43), and λ is the Yukawa screening length from Eq. (53).

To calculate the viscosity of a plasma at an arbitrary coupling parameter, the weak- and strong-coupling models are each evaluated. The two are then combined by adding them in quadrature

$$\eta_{YVM-SM}^* = \sqrt{(\eta_{YVM}^*)^2 + (\eta_{SM}^*)^2}. \quad (60)$$

In Fig. 5, we show that a simple quadrature addition of the two viscosity models gives excellent agreement with the molecular dynamics calculations of viscosity of a binary deuterium-argon system given in Ref. 140. The key observation to this method of combining viscosities is that each viscosity model is dominant in their respective regimes of validity; in the strong coupling regime, the weakly coupled plasma viscosity calculation is small relative to the Yukawa viscosity model, for instance. Alternative means of combining the viscosities, including a plasma coupling-dependent average of the two, were tested, but they were found to agree less well with the molecular dynamics data than the simple quadrature addition of the two viscosities.

To assess the impact of the new viscosity model, Fig. 6 shows the ratio of the new viscosity model to the previous model across a range of densities and temperatures for a single component hydrogen plasma. For reference, a time history of the mass-averaged density and temperature of the gas region of an igniting 1D simulation of a NIF capsule is imposed on the figure. The new model increases the viscosity by approximately 20% over the regime of interest.

The new viscosity model has a larger impact for multicomponent plasmas. In the previous model,¹³⁹ the one-component plasma expressions were generalized to multicomponent systems by calculating a mixture averaged coupling parameter and screening length. With the effective Boltzmann theory, the multicomponent viscosity is given by^{140,141}

$$\eta = \sum_i \eta_{(i)}, \quad (61)$$

where $\eta_{(i)}$ are the partial viscosities contributed by the i th constituent of the mixture and determined according to the linear system,

$$\begin{aligned} \frac{5}{3}n_i T &= \eta_{(i)} \sum_j \nu_{ij} \\ &+ \sum_j \frac{m_i m_j}{m_i + m_j} \left(\frac{\eta_{(i)} \nu_{ij}}{m_j} - \frac{\eta_{(j)} \nu_{ji}}{m_i} \right) \left(\frac{10}{3} z_{ij}'' - 1 \right), \end{aligned} \quad (62)$$

where $z_{ij}'' = \Omega_{ij}^{(22)}/\Omega_{ij}^{(11)}$ and

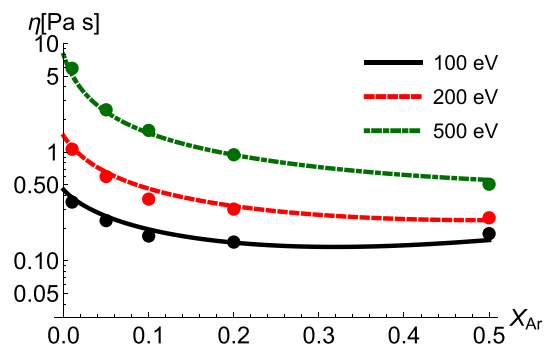


FIG. 5. Comparison of the viscosity model of Eq. (60), shown in lines, with the molecular dynamics simulation data of Ref. 140, shown in circles, for a D-Ar plasma. The black, red, and green lines show our calculations at temperatures of 100, 200, and 500 eV.

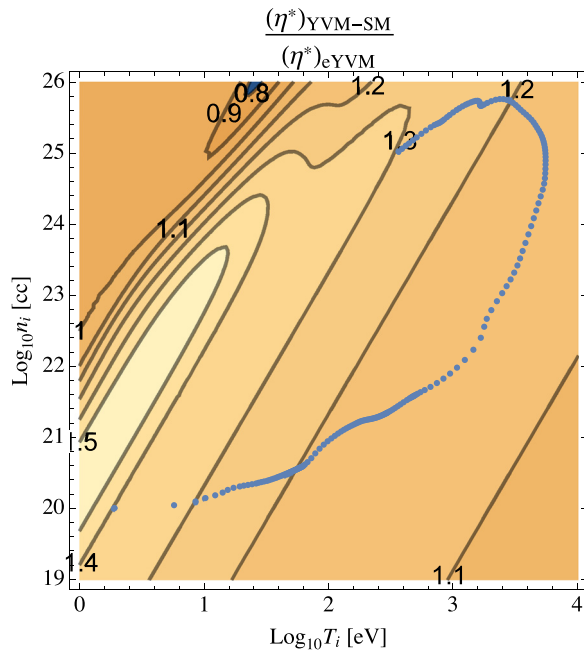


FIG. 6. Ratio of the hybrid viscosity of Eq. (60) to the extended YVM viscosity of Ref. 139 for a $Z=1$ plasma. The blue dots represent the mass-averaged density and temperature of the gas region of a 1-D imploding NICrev5 capsule.

$$\nu_{ij} = \frac{16n_j m_j \Omega_{ij}^{22}}{3(m_i + m_j)}. \quad (63)$$

This constitutes an $N \times N$ linear system for the partial viscosities, where N is the number of components in the mixture. Although inversion of linear systems is straightforward to compute, this must be performed on a zone-by-zone basis every time step and is a notable increase in complexity relative to the calculation of a scalar viscosity. To mitigate this complexity, Ares instead employs an approximation due to Burgers, given by

$$\eta \approx \frac{5}{3} \sum_i n_i T \left(\sum_j \nu_{ij} \right)^{-1}. \quad (64)$$

This approximation neglects the final summation in Eq. (62), which is justified when $\sum_j \nu_{ij}$ is approximately the same for all i . In Ref. 142, this approximation was found to be valid to 0.2% for a D-Ar mixture over a range of warm dense matter parameters. Figure 7 compares the new and previous plasma viscosity models for a 90%/10% D-Ar mixture, revealing that the improved multicomponent treatment changes the plasma viscosity by up to a factor of 4.

The main point of this section is to emphasize the importance of accurately verifying plasma models in table-top experiments. Viscosity based on the model of Sec. III, for example, is used in the Ares code. This model makes it possible to define “partial viscosities” in a multicomponent plasma. Over the density and temperature range of NIF-relevant experiments, this model yields viscosities that are larger by factors of up to 4, with significant implications for the development of turbulence. It is encouraging that other aspects of this model have been confirmed by MD simulations and by UNP experiments

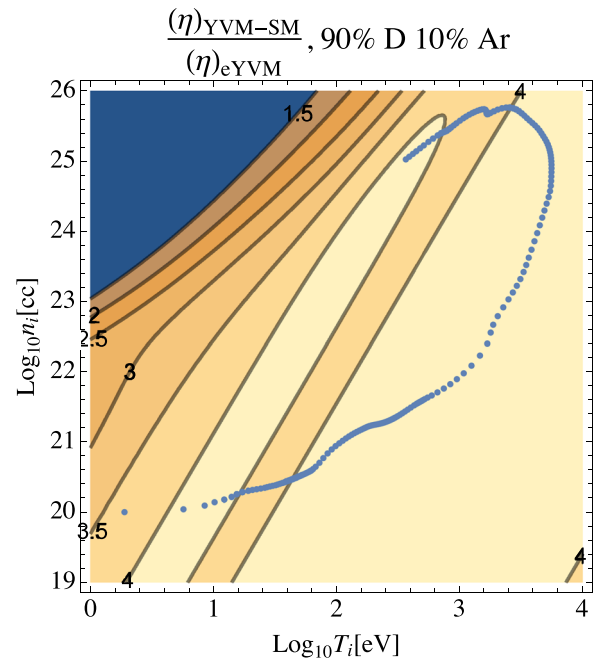


FIG. 7. Ratio of the hybrid viscosity of Eq. (60) to the extended YVM viscosity of Ref. 139 for a D-Ar plasma. The Ar has been assumed to be fully ionized. The blue dots again depict a density-temperature trajectory of the gas of a 1-D NICrev5 imploding capsule.

(see Sec. VIII). Such confirmations lend confidence to Ares code calculations based on this model.

B. Electron-ion coupling

Another important process in HEDP is the collisional temperature equilibration between electron and ion populations. Ares has the ability to track separate electron and ion temperatures, with all ion species in a multicomponent material assumed to be in temperature equilibrium with each other. Because the cross section for thermonuclear fusion is a strong function of temperature—and because laser heating, shock heating, and alpha energy deposition asymmetrically heat electron and ion populations—it is important to accurately model the flow of heat between electrons and ions.

Electron-ion coupling rates in the plasma phase can be calculated using kinetic or many-body models. An early result due to Landau applied a Fokker-Planck collision operator to approximate binary collisions in a classical two-component electron-ion plasma in the limit of small scattering angles.¹⁴² ICF simulations often employ a modification of the Landau-Spitzer equilibration rate due to Brysk,¹⁴³ which includes electron degeneracy. Preceding this work, Ares used the Brysk model for electron-ion equilibration.

Whereas both the Landau-Spitzer and Brysk models employ a Coulomb logarithm due to divergent integral of the Rutherford scattering cross section over impact parameter, modern treatments incorporate the relevant physics to truncate the interaction at long- and short-wavelengths. Examples include a many-body Green’s function approach,¹⁴⁴ dimensionally regularized kinetic theory,¹⁴⁵ and quantum Lenard-Balescu theory.^{146,147}

In this section, we summarize a computationally efficient approximation to the quantum Lenard-Balescu (QLB) equilibration rate (presented in Ref. 150) and compare the equilibration rate to that of Brysk for hydrogenic plasmas in the ICF regime. The QLB rate has been shown to agree well with molecular dynamics simulations^{146,151,152} up to moderate plasma coupling ($\Gamma \approx 20$). The model includes electron degeneracy, quantum diffraction (via the response function), and screening (via the dielectric function). Aside from very large plasma coupling, the expression is not expected to be accurate in the coupled mode regime, wherein the temperature separation is sufficiently large for the ion acoustic oscillation to impact the equilibration rate. The coupled mode regime has been a topic of recent interest,^{147,152} and its importance in electron-ion coupling remains open.

In the QLB approach, the collision integral of Eq. (29) is replaced by a form that is derived from a correlation expansion. This introduces a dependency on the many-body frequency- and wavevector-dependent dielectric response function rather than the binary cross section. The kinetic equations of motion in Eq. (28) are replaced by^{148,149}

$$\frac{\partial f_e}{\partial t} = C_{ee}(f_e) + C_{ei}(f_e, f_i), \quad (65)$$

$$\frac{\partial f_i}{\partial t} = C_{ii}(f_i) + C_{ie}(f_e, f_i). \quad (66)$$

The QLB collision operator is given by

$$C_{ei}(f_e, f_i) = -\frac{1}{4\pi^2 \hbar^2} \iint d^3 \mathbf{v}' d^3 \mathbf{k} \Phi(\mathbf{k}, \mathbf{v}) \mathcal{D}(\mathbf{k}, \mathbf{v}, \mathbf{v}'), \quad (67)$$

$$\Phi(\mathbf{k}, \mathbf{v}) = \frac{|\phi_{ei}(k)|^2}{\left| \epsilon \left(k, \mathbf{k} \cdot \mathbf{v} + \frac{\hbar k^2}{2m_e} \right) \right|^2}, \quad (68)$$

$$\mathcal{D}(\mathbf{k}, \mathbf{v}, \mathbf{v}') = \delta[\mathbf{k} \cdot (\mathbf{v} - \mathbf{v}') + \hbar k^2 / 2\mu] [f_e(\mathbf{v}) f_i(\mathbf{v}') - f_e(\mathbf{v} + \hbar \mathbf{k} / m_e) f_i(\mathbf{v}' - \hbar \mathbf{k} / m_i)], \quad (69)$$

where δ is the Dirac delta function, \mathbf{k} is the wave vector, ϵ is the dielectric response function in the random phase approximation,^{146,153} μ is the electron-ion reduced mass, and

$$\phi_{ie}(k) = \frac{4\pi Z e^2}{k^2} \quad (70)$$

is the Fourier-transformed Coulomb potential. From this expression, one can construct an ion temperature equilibration rate,¹⁵⁰

$$\frac{dT_i}{dt} = -\frac{\hbar}{3\pi^2 n_i} \int_0^\infty dk k^2 \int_0^\infty d\omega \omega \left| \frac{\phi_{ei}(k)}{\epsilon(k, \omega)} \right|^2 \times \left\{ N\left(\frac{\hbar\omega}{2T_i}\right) - N\left(\frac{\hbar\omega}{2T_2}\right) \text{Im}[\chi_e^0(k, \omega)] \text{Im}[\chi_i^0(k, \omega)] \right\}, \quad (71)$$

where ω is the frequency, $N(x) = \coth(x)$, and $\chi_j^0(k, \omega)$ is the free-particle response function of species j . The free-particle response functions and dielectric function are related via

$$\epsilon(k, \omega) = 1 - \frac{4\pi e^2}{k^2} [\chi_e^0(k, \omega) + Z^2 \chi_i^0(k, \omega)]. \quad (72)$$

Given the ion temperature time rate of change, the corresponding electron equilibration rate may be determined from conservation of energy and quasineutrality ($n_e \approx Zn_i$).

Although this expression may be evaluated numerically, it is too expensive to evaluate for each zone and each time step in a multiphysics simulation. An in-line approximation for evaluating this integral has recently been presented by Scullard *et al.*¹⁵⁰ The in-line expression neglects quantum diffraction effects in the dielectric function and assumes $\alpha = m_e T_i / m_i T_e \ll 1$. The result involves no explicit Coulomb logarithm due to the convergent integrals in the QLB theory.

The in-line QLB equilibration rate implemented in Ares is¹⁵⁰

$$\frac{dT_i}{dt} = -\frac{4Z^2 e^4 m_e^2 e^{-\mu T_e}}{3\pi \hbar^3 m_i} \left(\frac{T_i}{T_e} - 1 \right) \tilde{f} \left(\frac{1}{\Lambda} \right), \quad (73)$$

where μ is the chemical potential,

$$\frac{1}{\Lambda} = \frac{1}{Z} \frac{T_i}{T_{\text{eff}}} \frac{\pi \hbar^2 Z^2 e^2 n_i}{2m_e T_i^2} \left(\frac{m_e}{m_i} + \frac{T_i}{T_e} \right), \quad (74)$$

T_{eff} is the effective temperature,

$$T_{\text{eff}} = \left(T_e^{9/5} + \left(\frac{2}{3} E_F \right)^{9/5} \right)^{5/9}, \quad (75)$$

E_F is the Fermi energy, and \tilde{f} is the special function,

$$\tilde{f}(x) = \int_0^\infty \frac{te^{-t}}{(1 + e^{-\mu-t})(t+x)^2} dt. \quad (76)$$

In-line approximations for \tilde{f} are provided in Ref. 150, but they are unnecessary to detail here.

The in-line QLB model accurately approximates the full QLB expression, as shown in Fig. 8. Here we calculate the electron-ion equilibration rate using accurate numerical evaluations of the QLB collision operator, the in-line QLB model, and a Boltzmann-based expression due to Brysk.¹⁴³ Differences between the in-line model and the full expression are imperceptible on this scale.

In Fig. 9, we compare the equilibration rates calculated by the Brysk and in-line QLB expressions, both of which are available in Ares. The QLB model reduces the electron-ion coupling rate by 10%–20% for the parameters sampled by the gas region of the imploding capsule.

Here again is an opportunity for table-top experiments to accurately measure equilibration rates based on the foregoing models. The

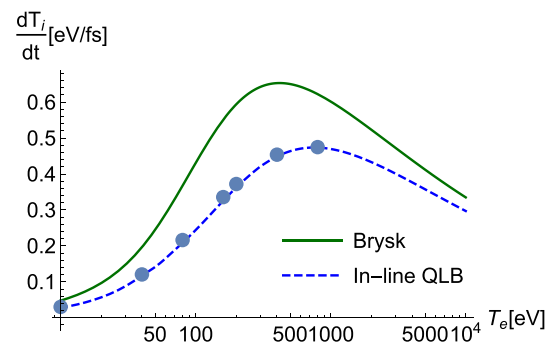


FIG. 8. Electron-ion equilibration rate for a $Z = 1$ plasma at a density of $10^{25}/\text{cm}^3$ and $T_i = 0.8T_e$. Accurate numerical evaluations of the QLB collision operator are shown with blue markers; the in-line approximation is shown to agree well.

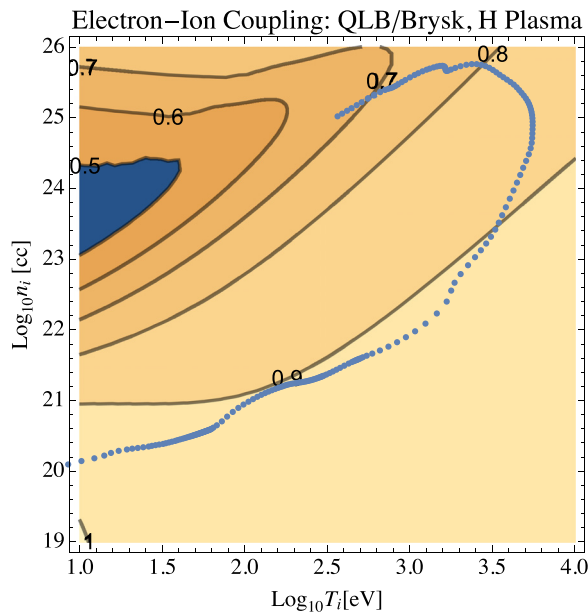


FIG. 9. Ratio of the electron-ion coupling rate of Eq. (73) to that of Ref. 143 for a H plasma. The blue dots again depict a density-temperature trajectory of the gas of a 1-D NlCrev5 capsule.

equilibration experiments described in this paper could potentially provide such a measurement.

C. Discussion

The goal of this section is to provide an illustration of the interplay between models, simulations, and experimental measurements and to give a few examples of how UNP measurements might be helpful for HEDP simulations. Multiphysics simulations involve dozens of interacting processes, each of which requires a number of approximations and discretization choices to lend an efficient computational model. Vetting these approximations can be particularly challenging in the HEDP context where experiments are typically highly integrated and difficult to diagnose.

For multiphysics code development, data for multicomponent plasmas are particularly important. When transport coefficients for single component plasmas are the only available data, averaging rules must be used when applied to multicomponent systems. One important opportunity for UNPs is to scrutinize these averaging rules in systems with high-precision diagnostic capability.

UNPs could measure the electron-ion temperature relaxation rate in HEDP-relevant scaled parameter space (see Sec. VII). While the electrons in UNPs are nondegenerate, the momentum transfer calculations would give greater confidence to Eq. (73). Measurements of viscosity and diffusion in the strongly coupled regime are also important, and some UNP measurements have been made (see Sec. VI). UNP measurements ion friction, which is related to momentum transfer, and stopping power would also be important (see Sec. VIII). The nonequilibrium process of energy relaxation, specifically for bump-on-tail distributions, and stopping power are important for understanding the thermalization of neutrons, alpha particles, ions, and electrons in HEDP systems.

Additional focused experimental efforts and high-fidelity micro-physics calculations are essential for validating approximations and/or identifying improved models. The dependence of transport processes on dimensionless parameters, which can be the same for very hot and very cold systems, allows ultracold plasmas to inform the transport models used in multiphysics codes, ultimately improving our understanding of basic science and supporting important applications such as laboratory ignition.

V. AVALANCHE TO STRONG COUPLING IN A MOLECULAR RYDBERG GAS

This section describes the plasmas formed by cold NO molecules excited to selected electronic states within a few milli-electron-volts of the ionization threshold. In some respects, these molecular plasmas exhibit properties very similar to UNPs formed by photo-ionizing laser-cooled atoms in a magneto-optical trap (MOT), which are described in Secs. VI–VIII. The initial neutral atoms and molecules have subkelvin temperatures and Gaussian initial spatial distributions. However, molecular beam plasmas form with initial densities that can exceed MOT plasmas by several orders of magnitude. Free-jet expansions can also be seeded with any of a large number of chemical substances, providing a unique measure of control of temperature, density, laboratory velocity, and atomic or molecular species. Finally, larger initial densities afford longer plasma lifetimes. These features suggest that atomic and molecular beam plasmas may provide a useful new platform for HEDP simulations.

A. The molecular beam ultracold plasma compared with a MOT

The excitation pathway from cold neutral molecules to ultracold plasma causes the initial dynamics of ionization in the molecular beam Rydberg gas to differ substantially from that in the plasma formed by direct photoionization of atoms in a MOT. Steps of laser excitation prepare a Rydberg gas consisting initially of molecules in a single selected Rydberg state, of hydrogenic principal quantum number, n_0 . The binding energy of this state measured with respect to a state specified ionization threshold is

$$E_{n_0} = -\frac{R}{(n_0 - \delta)^2}, \quad (77)$$

where $R = 13.6 \text{ eV}$ is the Rydberg constant and δ is the quantum defect of that particular series. The quantum defect accounts for the incomplete shielding of the total charge of a core ion by its residual electrons. This shielding becomes more complete for Rydberg electrons with higher orbital angular momentum, ℓ . For example, the $n_0 f(2)$ series in NO converges to the ${}^2\Sigma^+ N^+ = 2$ state of NO^+ with a quantum defect of about 0.03. Note that the formalism in this section will refer to number density using the symbol, ρ to avoid confusion with n , used here to describe the principal quantum number.

When a Rydberg gas of principal quantum number $n_0 > 30$ (with a binding energy less than 15 meV) reaches sufficient density, it undergoes a spontaneous avalanche to form an ultracold plasma as illustrated in Fig. 10.^{38,154,155} Even for Rydberg gas densities at which the average distance between molecules is much larger than the Rydberg orbital radius, some fraction of the distribution of nearest-neighbor distances will fall within a radius for strong interaction and

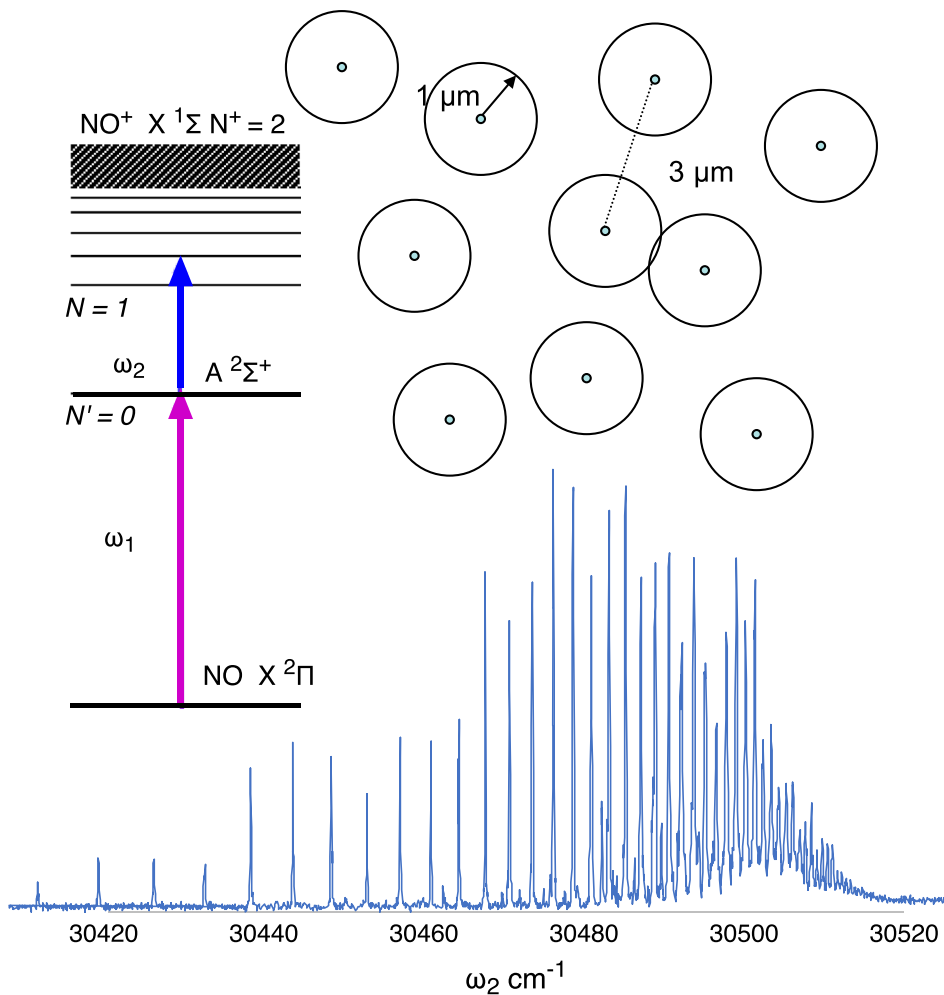


FIG. 10. Diagram illustrating the double-resonant excitation of a molecular Rydberg gas of nitric oxide, and the conditions leading to Penning ionization and avalanche to an ultracold plasma. The spectrum shows an atomiclike structure of $n_0 f(2)$ Rydberg state resonances converging to the $N^+ = 2$ rotational limit of NO^+ . For an initial $n_0 = 50$ Rydberg gas density of 10^{10} cm^{-3} and the orbital radius is about $1 \mu\text{m}$, while the average spacing between Rydberg molecules is $3 \mu\text{m}$. However, some fraction of the population of nearest neighbors is separated by $1 \mu\text{m}$ or less, and these pairs interact by Penning ionization to form prompt electrons, which seed the avalanche to ultracold plasma.

prompt Penning ionization. Following the avalanche that results, a complex interplay between collisional rate processes and ambipolar hydrodynamics governs the evolving properties of this plasma. In the particular case of a molecular Rydberg gas, added channels of neutral fragmentation, linked with electron-impact ionization, three-body recombination, and electron-Rydberg inelastic scattering in an expanding distribution of charged particles, can give rise to striking effects of self-assembly and spatial correlation.^{156,157}

The conditions necessary to form a molecular ultracold plasma require a high mach-number supersonic molecular beam. The hydrodynamic properties of a skimmed, seeded free-jet expansion cause gas to move with relatively high velocity in the laboratory, while attaining an exceedingly well-defined, propagation-distance-dependent density and subkelvin temperature in the local frame.¹⁵⁸ The millikelvin molecular temperature substantially exceeds the sub-100 microkelvin temperature of some laser-cooled atoms in a MOT. But the evolution to plasma tends to erase this distinction because the DIH temperature of the ions in the plasma rises to the order of 1 K, whether measured in a MOT or a beam [see Eq. (14)].

B. Supersonic molecular beam temperature and particle density

In a skimmed supersonic molecular beam, nitric oxide (NO) molecules seeded 1:10 in He forms a phase-space distribution that factors into longitudinal (beam propagation direction) and transverse coordinate dimensions. In the propagation direction, z , the laboratory velocity of this NO beam, u_{\parallel} , rises to a typical limit of 1400 m/s and the distribution of local velocities, v_{\parallel} , narrows to define a local temperature, T_{\parallel} , of approximately 500 mK. Transverse to propagation, the beam forms a Gaussian spatial distribution in x and y . In this plane, the local velocity, $v_{\perp}(r)$, is defined for any radial distance almost entirely by the divergence velocity of the beam, $u_{\perp}(r)$. Phase-space sorting cools the temperature in the transverse coordinates, T_{\perp} , to a much lower value, typically $\sim 5 \text{ mK}$.¹⁵⁸

The stagnation pressure (the pressure behind the nozzle of the beam) and seeding ratio determine a well-defined local density as a function of z . For example, expanding from a stagnation pressure of 500 kPa with a 1:10 seeding ratio, a molecular beam propagates 2.5 cm to a skimmer and then 7.5 cm to a point of laser interaction, where it contains NO at a peak density of $1.62 \times 10^{14} \text{ cm}^{-3}$. At this point, a

perpendicular, crossed-beam alignment of the laser and molecular beam defines a Gaussian ellipsoidal volume in which the transition sequence, $X^2\Pi_{1/2} N'' = 1 \xrightarrow{\omega_1} A^2\Sigma^+ N' = 0 \xrightarrow{\omega_2} n_0 f(2)$, forms a gas of molecules in a single Rydberg state of defined principal quantum number, n_0 , orbital angular momentum, $\ell = 3$, NO^+ core rotational quantum number of $N^+ = 2$ and total angular momentum neglecting spin of $N = 1$.

A typical experiment promotes the first step in a regime of linear absorption.^{38,158} Thus, an ω_1 pulse with an energy of 1.7 μJ and a Gaussian width of 0.2 mm, ideally overlapped by an ω_2 pulse with sufficient fluence to saturate the second step forms a Rydberg gas ellipsoid with an nominal peak density of $5 \times 10^{12} \text{ cm}^{-3}$. Pulse energies and microscopic conditions of overlap fluctuate; thus, real densities typically fall short of ideal ones by as much as a factor of five or ten.

C. Penning ionization

The density distribution of a Rydberg gas defines a local mean nearest neighbor distance between excited molecules, or Wigner-Seitz radius of $a_{ws} = (3/4\pi\rho)^{1/3}$, where ρ refers to the local Rydberg gas density. The probability density for finding the k th nearest neighbor at a distance r in a gas with a number density ρ is given by the Erlang distribution,^{159,160}

$$p_k(r) = \frac{\rho}{k!} \left(\frac{r^3}{a_{ws}^3} \right)^{k-1} \exp \left[- \left(\frac{r}{a_{ws}} \right)^3 \right]. \quad (78)$$

From Eq. (78), it is straightforward to show that the most probable nearest neighbor separation ($k=2$) is $r = a_{ws}$. An initial core density of $\rho_0 = 0.5 \times 10^{12} \text{ cm}^{-3}$, $a_{ws} = 0.8 \mu\text{m}$. A semiclassical model¹⁶¹ suggests that 90 percent of Rydberg molecule pairs separated by a critical distance, $r_c = 1.8 \cdot 2n_0^2 a_0$, or less undergo Penning ionization within 800 Rydberg periods, where $a_0 = 5.29 \times 10^{-11} \text{ m}$ is the Bohr radius. Integrating the Erlang distribution from $r=0$ to the critical distance $r=r_c$ for a Rydberg gas of given principal quantum number n_0 yields the local density of Penning electrons (ρ_e at $t=0$) produced by this prompt interaction, for any given initial local density, ρ_0 ,

$$\rho_e(\rho_0, n_0) = \frac{0.9}{2} \cdot 4\pi\rho_0^2 \int_0^{r_c} r^2 e^{-\frac{4\pi}{3}\rho_0 r^3} dr. \quad (79)$$

Evaluating this definite integral yields an expression in a closed form that predicts the Penning electron density for any particular initial Rydberg density and principal quantum number,

$$\rho_e(\rho_0, n_0) = \frac{0.9\rho_0}{2} (1 - e^{-\frac{4\pi}{3}\rho_0 r_c^3}). \quad (80)$$

Prompt Penning ionization acts on the portion of the initial nearest-neighbor distribution in the Rydberg gas that lies within r_c . A molecule ionizes when its collision partner relaxes to a lower principal quantum number, $n' < n_0/\sqrt{2}$. This close-coupled interaction disrupts the separability of Rydberg orbital configurations, redistributing the strongly dissociative character of core penetrating states. As a result, we can expect Penning partners to dissociate, leaving a spatially isolated distribution of ions. We refer to the spatial correlation that results as a Penning lattice.¹⁶² The initial ion pair distribution function $g(r)$ has a hole near $r=0$. The extend of this effect varies depending on the local density and the selected initial principal quantum number.

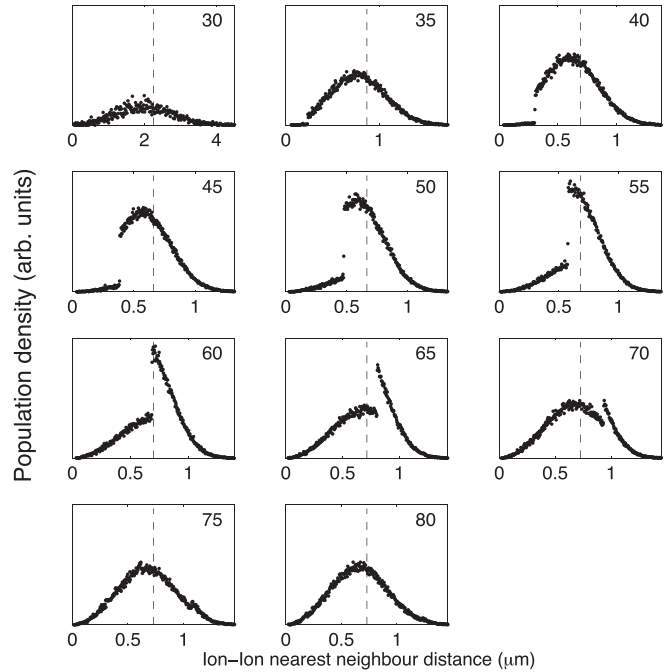


FIG. 11. Simulated distributions of ion-ion nearest neighbors following Penning ionization¹⁶² at a density of 10^{12} cm^{-3} . The number in the upper right-hand corner of each plot denotes the initial principal quantum number, n_0 , of the Rydberg level, ranging from 30 to 80. These distributions are calculated by counting ion distances after relaxation to plasma in 10^6 -particle stochastic simulations. Starting when $n_0 = 35$, the shape of the nearest neighbor distribution from Eq. (79) is depleted at small- r due to Penning ionization. Reproduced with permission from Sadeghi *et al.*, Phys. Rev. Lett. 112, 075001 (2014). Copyright 2014 American Physical Society.

Figure 11 shows the degree to which Rydberg gases with initial principal quantum numbers from 30 to 80 form a Penning lattice for an initial density of $1 \times 10^{12} \text{ cm}^{-3}$.

D. Spontaneous electron-impact avalanche

The electrons formed by prompt Penning ionization trigger an electron impact avalanche. The kinetics of this process are well described by coupled rate equations for electron-Rydberg inelastic scattering, electron-impact ionization, and three-body ion-electron recombination^{163–166} using detailed rate coefficients, k_{ij} , $k_{i,ion}$, and $k_{i,thr}$ validated by MD simulations,⁴⁵

$$-\frac{d\rho_i}{dt} = \sum_j k_{ij}\rho_e\rho_i - \sum_j k_{ji}\rho_e\rho_j + k_{i,ion}\rho_e\rho_i - k_{i,thr}\rho_e^3 \quad (81)$$

and

$$\frac{d\rho_e}{dt} = \sum_i k_{i,ion}\rho_e^2 - \sum_i k_{i,thr}\rho_e^3. \quad (82)$$

The relaxation of molecules in the manifold of Rydberg states populated by initial Penning ionization and subsequent three-body recombination balances with the evolving temperature of electrons released by avalanche to conserve total energy per unit volume,

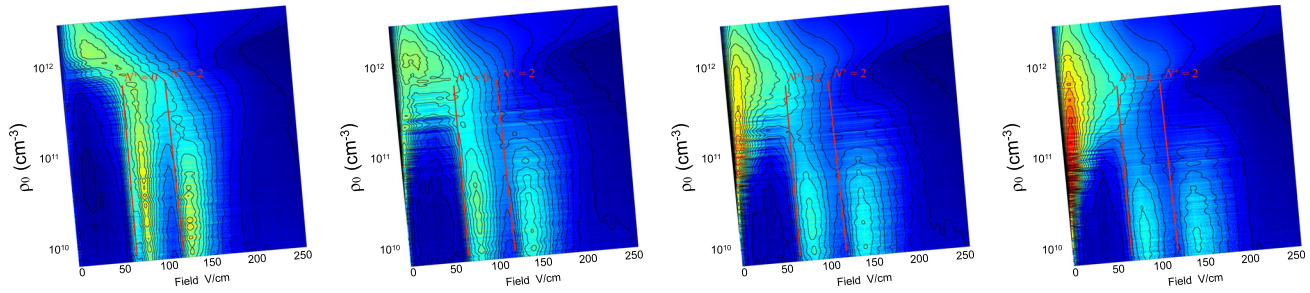


FIG. 12. Contour plots showing SFI signal as a function the applied field for an $nf(2)$ Rydberg gas with an initial principal quantum number, $n_0 = 49$. Each frame represents 4,000 SFI traces, sorted by initial Rydberg gas density. Ramp field potential applied to G_1 , beginning from left to right 0, 150, 300, and 450 ns after the ω_2 laser pulse. The two bars of signal most evident at early ramp field delay times represent the field ionization of the $49f(2)$ Rydberg state, respectively, to $\text{NO}^+ X \ ^1\Sigma^+$ cation rotational states, $N^+ = 0$ and 2. The signal waveform extracted near zero applied field represents the growing population of plasma electrons.

$$E_{tot} = \frac{3}{2} k_B T_e(t) \rho_e(t) - R \sum_i \frac{\rho_i(t)}{n_i^2}, \quad (83)$$

where, for simplicity, we neglect the longer-time effects of Rydberg predissociation and electron-ion dissociative recombination.¹⁶⁵

Such calculations show that the conversion from Rydberg gas to plasma occurs on a time scale determined largely by the local Penning electron density, or Penning fraction, $P_f = \rho_e / \rho_0$, which depends on the local density of Rydberg molecules and their initial principal quantum number.

Avalanche times predicted by coupled rate equation calculations range widely. For example, in a model developed for experiments on xenon, simulations predict that a Rydberg gas with $n_0 = 42$ at a density of $8.8 \times 10^8 \text{ cm}^{-3}$ ($P_f = 6 \times 10^{-5}$) avalanches with a half time of $40 \mu\text{s}$.¹⁶⁷ At an opposite extreme, rate equations estimate that a Rydberg gas of NO with $n_0 = 60$ at a density of $1 \times 10^{12} \text{ cm}^{-3}$ ($P_f = 0.3$) rises to plasma in about 2 ns.¹⁶⁵

Selective field ionization (SFI) probes the spectrum of binding energies in a Rydberg gas. Applied as a function of time after photoexcitation, SFI maps the evolution from a state of selected initial principal quantum number, n_0 , to plasma.¹⁵⁷ Figure 12 shows SFI spectra taken at a sequence of delays after the formation of $49f(2)$ Rydberg gases of varying density.

Here, we can see that a $49f(2)$ Rydberg gas with an estimated initial density $\rho_0 = 3 \times 10^{11} \text{ cm}^{-3}$ relaxes to plasma on a time scale of about 500 ns. Observations such as these agree well with the predictions of coupled rate-equation calculations. We can understand this variation in relaxation dynamics with ρ_0 and n_0 quite simply in terms of the corresponding density of prompt Penning electrons these conditions afford to initiate the avalanche to plasma.

Figure 13 illustrates this, showing how rise times predicted by coupled rate-equation simulations for a large range of initial densities and principal quantum number match when plotted as a function of time scaled by the ultimate plasma frequency and fraction of prompt Penning electrons. The dashed line gives an approximate account of the scaled rate of avalanche under all conditions of Rydberg gas density and initial principal quantum number in terms of the simple sigmoidal

$$\frac{\rho_e}{\rho_0} = \frac{a}{b + e^{-c\tau}}, \quad (84)$$

where

$$\tau = t\omega_p^{(e)} P_f^{3/4}, \quad (85)$$

in which $\omega_p^{(e)}$ is the electron plasma frequency after avalanche, P_f is the fraction of prompt Penning electrons, and $a = 0.00062$, $b = 0.00082$, and $c = 0.075$ are empirical coefficients.

E. Plasma evolution in a Rydberg gas Gaussian ellipsoid

Local density and principal quantum number serve in a straightforward way to determine the rate at which a Rydberg gas avalanches to plasma. A TEM_{00} laser pulse crosses a cylindrically Gaussian

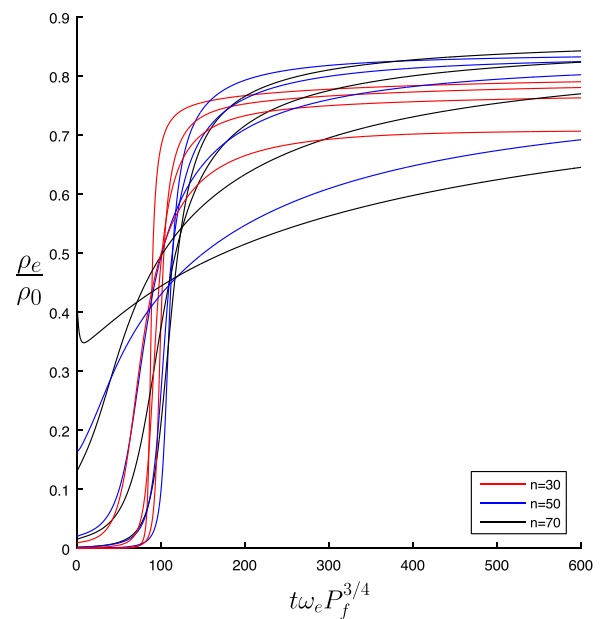


FIG. 13. Rise in fractional electron density as a function of time scaled by the electron plasma frequency, $\omega_p^{(e)}$ and fraction, $\rho_e(t=0) / \rho_0 = P_f$, of prompt Penning electrons. Simulation results shown for $n_0 = 30, 50$ and 70 with initial densities, $\rho_0 = 10^9, 10^{10}, 10^{11}$, and 10^{12} cm^{-3} .

molecular beam to prepare a Rydberg gas in a single $n_0f(2)$ initial state with a Gaussian ellipsoidal distribution of initial density. We can represent this distribution by a system of concentric ellipsoidal shells of varying density.¹⁶⁸ Avalanche occurs within a given shell at a rate that is well-defined by the local density as detailed above. Conversion of Rydberg molecules to a rising population of ions conserves the particle number in a shell (neglecting dissociation). The local space charge confines electrons, conserving quasineutrality. Electrons exchange kinetic energy at the boundaries of each shell, sustaining a single plasma electron temperature.

This situation describes the first few tens of nanoseconds, during which time the ions are approximately stationary. The quasineutral approximation calls for a radial electric potential gradient, which gives rise to a force, $-e\nabla\phi_{k,j}(t)$, that accelerates the ions in shell j in direction k according to¹⁶⁹

$$\frac{-e}{m'} \nabla \phi_{k,j}(t) = \frac{\partial u_{k,j}(t)}{\partial t} = \frac{k_B T_e(t)}{m' \rho_j(t)} \frac{\rho_{j+1}(t) - \rho_j(t)}{r_{k,j+1}(t) - r_{k,j}(t)}, \quad (86)$$

where $\rho_j(t)$ represents the density of ions in shell j .

The instantaneous velocity, $u_{k,j}(t)$ determines the change in the radial coordinates of each shell, $r_{k,j}(t)$,

$$\frac{\partial r_{k,j}(t)}{\partial t} = u_{k,j}(t) = \gamma_{k,j}(t) r_{k,j}(t), \quad (87)$$

which in turn determines shell volume and thus its density, $\rho_j(t)$. The electron temperature supplies the thermal energy that drives this ambipolar expansion. Ions accelerate and T_e falls according to

$$\frac{3k_B}{2} \frac{\partial T_e(t)}{\partial t} = - \frac{m'}{\sum_j N_j} \sum_{k,j} N_j u_{k,j}(t) \frac{\partial u_{k,j}(t)}{\partial t}, \quad (88)$$

where we define an effective ion mass, m' ,

$$m' = \left(1 + \frac{\rho_j^*(t)}{\rho_j(t)} \right) m, \quad (89)$$

in which $\rho_j^*(t)$ represents the instantaneous Rydberg density in shell j . This effective mass accounts for the redistribution of ion momentum by free-electron-mediated resonant ion-Rydberg charge exchange, which occurs with a very large cross section.¹⁶³

The initial avalanche in the high-density core of the ellipsoid leaves few Rydberg molecules, so this term has little initial effect. Rydberg molecules predominate in the lower-density wings. There, the redistribution of momentum by charge exchange assumes a greater importance.

Ambipolar expansion quenches electron kinetic energy on a hundred nanosecond time scale. Core ions follow electrons into the wings of the Rydberg gas. There, the charge between NO^+ ions and NO^* Rydberg molecules recurs, equilibrating ion and Rydberg velocities and channeling electron energy through ion motion into $\pm x$ motion of gas volumes in the laboratory. The temperature of the plasma, defined almost entirely by the ion-Rydberg relative motion, falls as spatial correlation develops, and over a period of 500 ns, the system forms the plasma/high-Rydberg quasiequilibrium dramatically evidenced by the SFI results in Fig. 12.

In the wings, momentum redistribution owing to continuing charge transfer with the residual high-Rydberg population retards axial

expansion.^{163,170} By redirecting electron energy from ambipolar acceleration to $\pm x$ plasma motion, NO^+ to NO^* charge exchange dissipates electron thermal energy. This redistribution of energy released in the avalanche of the Rydberg gas to plasma causes the ellipsoidal Rydberg gas to bifurcate,^{156,157} forming very long-lived, separating charged-particle distributions, which we can capture on an imaging detector as pictured in Fig. 14. Here, momentum matching preserves density and enables ions and Rydberg molecules to relax to positions that minimize potential energy and build spatial correlation.

The semiclassical description of avalanche and relaxation outlined above forms an important point of reference from which we interpret our experimental observations. The laser crossed molecular beam illumination geometry creates a Rydberg gas with a distinctively shaped high-density spatial distribution. This initial condition has an evident effect on the evolution dynamics. We have developed semiclassical models that explicitly reckon with the coupled rate and hydrodynamic processes governing the evolution from Rydberg gas to plasma using a realistic, ellipsoidal representation of the ion/electron and Rydberg densities.¹⁶⁸ We find no combination of initial conditions that conforms classically with the state of arrested relaxation observed experimentally.

F. A molecular ultracold plasma state of arrested relaxation

Thus, we find that spontaneous avalanche to plasma splits the core of an ellipsoidal Rydberg gas of nitric oxide. Ambipolar expansion first quenches the electron temperature of this core plasma. Then, long-range, resonant charge transfer from ballistic ions to frozen Rydberg molecules in the wings of the ellipsoid quenches the center-of-mass ion/Rydberg molecule velocity distribution. This sequence of steps gives rise to a remarkable mechanics of self-assembly, in which the kinetic energy of initially formed hot electrons and ions drives an observed separation of plasma volumes. These dynamics redistribute ion momentum, efficiently channeling electron energy into a reservoir of mass-transport. This starts a process that evidently anneals

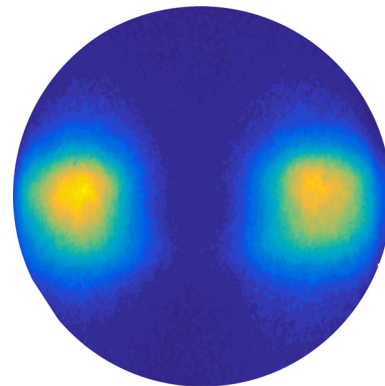


FIG. 14. A late-time x, y detector image of an ultracold plasma. The plasma was formed from an ellipsoidal Rydberg gas with an aspect ratio of 2:1. The initial Rydberg state was $40f(2)$ with $n_0 = 40$, the state with the highest depletion in the nearest-neighbor distribution (see Fig. 11). This image was taken after a plasma evolution time of $402 \mu\text{s}$, corresponding to a flight distance of 575 mm. Reproduced with permission from Haenel *et al.*, Phys. Rev. A **96**, 023613 (2017). Copyright 2017 American Physical Society.

separating volumes to a state of cold, correlated ions, electrons, and Rydberg molecules.

We have devised a three-dimensional spin model to describe this arrested state of the ultracold plasma in terms of two-, three-, and four-level dipole-dipole energy transfer interactions (spin flip-flops), together with Ising interactions that arise from the concerted pairwise coupling of three dipoles.^{171,172} The Hamiltonian includes the effects of onsite disorder owing to the broad spectrum of states populated in the ensemble and the unique electrostatic environment of every dipole. Extending ideas developed for simpler systems,^{173,174} one can make a case for slow dynamics, including an arrest in the relaxation of NO Rydberg molecules to predissociating states of lower principal quantum number.

G. Applications of molecular plasmas to HEDP

This section presents several aspects of molecular beam UNPs. We describe the evolution dynamics when the initial spatial density distribution is an ellipsoidal Gaussian. We show that the initially ellipsoidal spatial distribution separates into two well-defined spherical distributions, and we speculate about the resulting plasma state.

The density, species control, and comparatively long observation time should enable experiments relevant to HEDP science. We recently measured the expansion of two colliding plasmas.¹⁷⁵ The experiment is similar to atomic experiments described in Sec. VIII. With some improvements in modeling and diagnostics, these experiments could shed light on thermalization, diffusion, and momentum transfer in strongly coupled systems.

VI. STUDYING COLLISIONAL PROCESSES IN STRONGLY COUPLED STRONTIUM UNPS

In this section, we describe experiments using UNPs generated by photo-ionizing laser-cooled atoms in a MOT. Contrary to the molecular Rydberg plasmas of Sec. V, atoms are photo-ionized directly into the continuum. The electron temperature is given by the difference between the photo-ionization laser photon energy and the ionization energy, and it is typically in the $T_e = 5$ to 500 K range. We will describe fluorescence measurements, including the powerful capability of “spin-tagging” ions and tracking their velocities. This makes it possible to perturb the distributions using optical forces and to watch the perturbed distributions relax to match the surrounding background plasma.^{64,96}

A. Strontium ultracold neutral plasmas

For experiments, strontium atoms are photoionized with a two-photon process involving one photon at the wavelength of the laser-cooling transition (461 nm) and a second from a 10 ns pulsed dye laser tuned just above the ionization threshold at ~ 412 nm. This process ionizes $\sim 50\%$ of the atoms, creating an ultracold neutral plasma with initial electron and ion densities ($n_{0e} \approx n_{0i} \equiv n_0$) as high as $\sim 10^{10} \text{ cm}^{-3}$. The plasma inherits the density profile of the neutral atoms, which is typically Gaussian, with characteristic size $\sigma_0 \sim 1$ mm. All ions are formed in the $^2S_{1/2}$ electronic ground state. Effects of unionized atoms on the plasma are not significant because of the fast time scale of the experiment and small neutral-ion collision cross sections. Due to their relatively small mass, the electrons acquire most of the excess energy from the photoionizing photons, while the ion kinetic

energy is initially similar to that of the neutral atoms.¹⁷ In these experiments, ions equilibrate within $\sim 1 \mu\text{s}$, experiencing disordered-induced heating as short-range correlations develop.⁵⁹ This yields $1 \text{ K} \geq T_i \geq 0.2 \text{ K}$ and $5 \geq \Gamma_i \geq 1$. Electrons are kept warm ($T_e \geq 10 \text{ K}$) and relatively weakly coupled $\Gamma_e \leq 0.2$ to avoid recombination. The ions thus provide a highly accurate realization of a YOCP as described in Sec. I.⁵⁶ Transport measurements are performed during the expansion of the plasma into surrounding vacuum, which occurs on a relatively longer hydrodynamic time scale ($t_{\text{hydro}} > 100 \mu\text{s}$).

B. Optical probes and manipulations of strontium ions in ultracold neutral plasmas

To study the collisional and transport processes in a UNP, optical pumping is used to perturb the velocity distribution of a population of ions in the plasma. The relaxation of the perturbed velocity distribution is monitored using spatially resolved laser-induced-fluorescence (LIF) spectroscopy.⁹⁶ All laser excitations are near resonance with the $^2S_{1/2} - ^2P_{1/2}$ transition of Sr^+ at $\lambda = 422 \text{ nm}$, which has an excited-state lifetime of 7 ns and decay rate $\gamma/2\pi = 21 \text{ MHz}$. Optical pumping takes advantage of the fact that ground-state Sr^+ has an unpaired electron, with spin-projection quantum number $m = \pm 1/2$. It is important to note that the ions as a whole have close to a Maxwell-Boltzmann velocity distribution during the entire measurement.

Figure 15 depicts the optical pumping scheme and fluorescence diagnostic. In a typical configuration, two circularly polarized pump beams, with opposite polarization and propagation direction and the same frequency detuning $\Delta_{\text{pump}} \sim -\gamma$, interact with the plasma for a short time compared to ion dynamics ($\sim 100 \text{ ns}$). Because of the optical excitation selection rules and Doppler shifts associated with the different laser beams, ground-state ions with $m = 1/2$ and negative velocity $v \sim \Delta_{\text{pump}}\lambda/2\pi$ are resonant with the σ^- pump beam and are optically pumped from the $m = 1/2$ to the $m = -1/2$ state. Ions with positive velocity $v \sim -\Delta_{\text{pump}}\lambda/2\pi$ are resonant with the σ^+ pump beam and are optically pumped from the $m = -1/2$ to the $m = 1/2$ state. This produces a velocity distribution for $m = 1/2$ ions that is skewed to higher velocity. The distribution for $m = -1/2$ ions is skewed to lower velocity.

At an adjustable time after optical pumping, a third, less intense σ^- circularly polarized probe beam, near resonance with the transition, propagates through the plasma and induces fluorescence from $m = 1/2$ ions. Optical pumping during the probe beam is negligible. Laser induced fluorescence in a perpendicular direction is captured by a CCD camera.

A great deal of work has gone into developing laser-induced fluorescence (LIF) as a powerful probe of UNPs.^{176,177} The fluorescence intensity is proportional to the ion density. Scanning the LIF probe beam detuning yields the excitation spectrum, $S(\Delta_{\text{probe}})$, which is a convolution of the Lorentzian for the natural linewidth with the Doppler profile from the $m = 1/2$ ion velocity distribution. Deconvolution yields the time-resolved distribution of ion velocities along the LIF probe beam direction (\hat{z}) for $m = 1/2$ ions, $f_+(v_z, t)$.¹⁷⁸ From $f_+(v_z, t)$, one can extract various collisional and transport parameters. For example, the average velocity of the “tagged” population of ions ($m = 1/2$), $\bar{v}_z(t) = \int v_z f_+(v_z, t) dv_z$, relaxes toward the average background plasma velocity due to collisions (Fig. 16). Such data were used in Ref. 97 to measure velocity-relaxation rates for

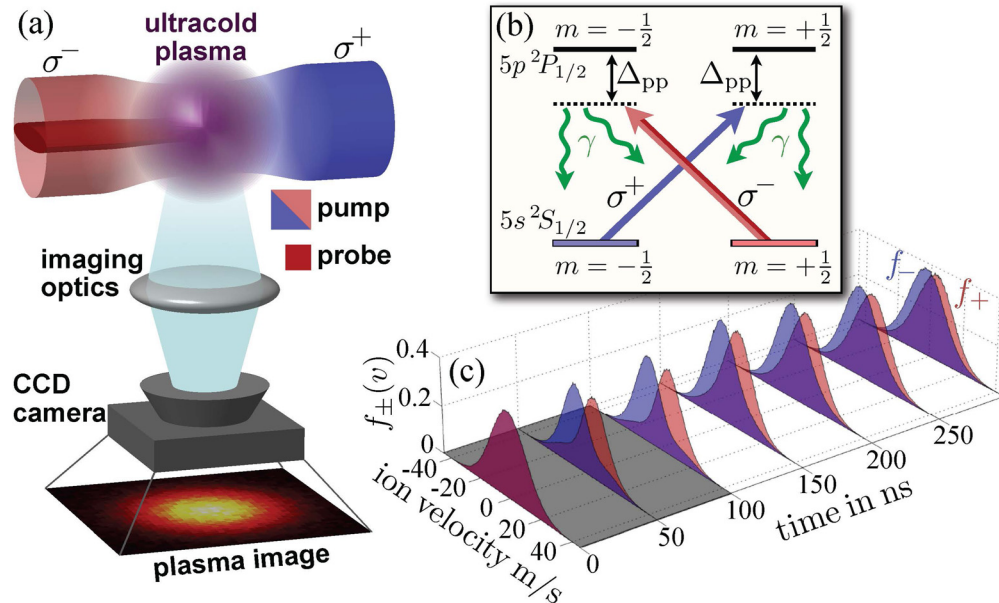


FIG. 15. (a) Experimental probe of ion relaxation in an ultracold plasma. Two counterpropagating, circularly polarized lasers, detuned by Δ_{pp} from the $5s^2S_{1/2} - 5p^2P_{1/2}$ transition, optically pump population between the two ground-state sublevels ($m = \pm 1/2$) of Sr ions. The corresponding level-scheme is shown in (b). The optical pumping produces skewed velocity distributions $f_{\pm}(v)$ for ions in each of the ground states. A σ_{-} circularly polarized light sheet, applied at a variable time after optical pumping, induces ion fluorescence that is recorded on a CCD camera to probe $f_{+}(v)$. A typical, simulated time evolution of the velocity distributions, f_{+} (red) and f_{-} (blue), during the optical pumping stage (gray) and subsequent relaxation is shown in (c). Reproduced with permission from Bannasch *et al.*, Phys. Rev. Lett. **109**, 185008 (2012). Copyright 2012 American Physical Society.⁹⁶

strongly coupled ions in UNPs. This method was used in Ref. 64 to observe non-Markovian dynamics and measure the self-diffusion rate.

C. Velocity equilibration beyond Landau-Spitzer

In Ref. 96, the velocity relaxation rate γ_v was determined by fitting $\bar{v}_z(t)$ with a non-Markovian damping model

$$\frac{d}{dt} \bar{v}_z(t) = - \int_0^t \mathcal{M}(t') \bar{v}_z(t-t') dt'. \quad (90)$$

Here the memory kernel $\mathcal{M}(t)$ accounts for retardation effects due to the strongly coupled nature of the equilibrium plasma.

The memory time vanishes in weakly coupled plasmas, for which $\mathcal{M}_z(v_z, t) = 2\gamma_v \delta(t)$. This yields exponential relaxation with a damping constant γ_v following the familiar Landau-Spitzer form,

$$\gamma_v = a \Gamma_i^{\frac{3}{2}} \omega_p^{(i)} \ln \Lambda, \quad \Lambda = \frac{b}{\sqrt{3} \Gamma_i^3}, \quad (91)$$

of the relaxation rate, with $a = 0.46$ and $b = 0.53$ ^{96,142,179} and Coulomb logarithm $\ln \Lambda$.

However, for the strong coupling conditions of ions in UNPs, the Landau-Spitzer treatment^{142,179} breaks down, as discussed in Sec. III C. The simple Landau-Spitzer $\ln \Lambda$ is negative for $\Gamma > 0.45$, reflecting the importance of large-angle scattering,¹²² correlation effects,^{180,181} and collective mode coupling.^{146,149} In addition, particle-particle forces display short-time correlations, which can be described with a Gaussian memory kernel,¹⁸²

$$\mathcal{M}_z(t) = \frac{2\gamma_v}{\sqrt{2\pi\tau^2}} \exp\left(-\frac{t^2}{2\tau^2}\right). \quad (92)$$

with a memory time τ . Using this theoretical framework, data from optical pumping and LIF of strontium ions in a UNP were used to determine γ_v for $3 > \Gamma_i > 1$. As shown in Fig. 17, the results were compared with molecular dynamics simulations and various theories and phenomenological formulas that extend the Landau-Spitzer (LS) formalism into the strongly coupled regime.⁹⁶ Later work also directly resolved the non-Markovian evolution of $v_z(t)$ for short times after optical pumping, as seen in Fig. 16.⁶⁴

D. Self-diffusion

The optical pumping and LIF technique were used to measure the ion self-diffusion constant in Ref. 64. This work established the equivalence of the normalized curve for relaxation of the average velocity, $\langle \Delta v_z(t) \rangle_{+}$, as shown in Fig. 16, with the ion velocity autocorrelation function (VAF),

$$Z(t) = \frac{1}{3} \langle \mathbf{v}_k(t) \cdot \mathbf{v}_k(0) \rangle. \quad (93)$$

Here, \mathbf{v}_k is the velocity of particle k , and brackets indicate an equilibrium, canonical-ensemble average. The VAF captures the effects of correlated collision dynamics and system memory on individual particle trajectories, and it plays an important role in the statistical physics of many-body systems. A Green-Kubo relation¹⁸³ was used to extract the ion self-diffusion constant from the VAF. Results were compared

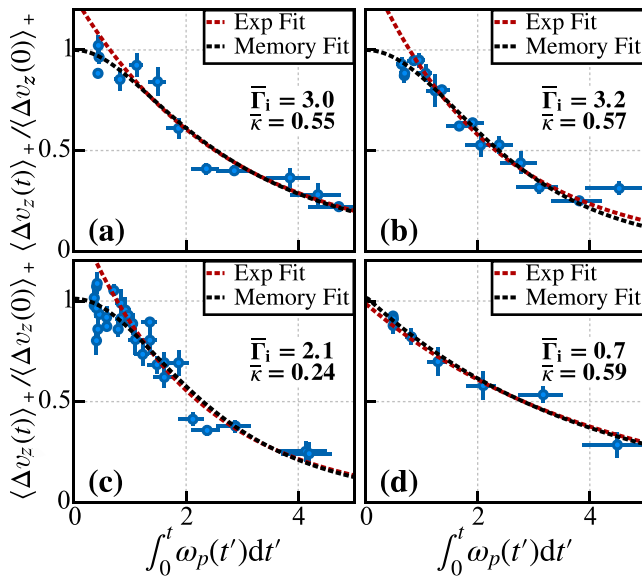


FIG. 16. Evolution of the normalized average velocity after optical pumping for ions in the $m = 1/2$ spin state in a strontium UNP. ($\langle \Delta v_z(t) \rangle_+ \equiv \langle v_z(t) \rangle_+ - \langle v_z(t) \rangle_{total}$ where $\langle v_z(t) \rangle$ is the average velocity of all the ions.) Specific experimental conditions are described in Ref. 64. Memory-function and exponential fits are indicated by the lines. The deviation from exponential decay, which is more significant for more strongly coupled plasmas, reflects memory-effects and non-Markovian dynamics. Time is normalized by the ion plasma oscillation frequency $\omega_p^{(i)}$. Reproduced with permission from Strickler *et al.*, Phys. Rev. X **6**, 021021 (2016). Copyright 2016 American Physical Society.

with molecular dynamics and theoretical models often used for describing high-energy-density plasmas.

The middle panel of Fig. 3 shows the normalized self-diffusion constant (D^*) plotted vs the ion Coulomb Coupling Constant, Γ_i . Traditional transport theory (dotted black line) breaks down in the strongly coupled regime. Measurement of the relaxation of the ion velocity (Fig. 16) can be used to extract the diffusion coefficient $D = D^* a^2 \omega_p^{(i)}$, which can be compared with MD simulations beyond the regime of validity of classic plasma theory. Measurements, shown using data symbols, agree with numerical calculations from Ref. 184 (blue and red lines). Results of two effective-potential calculations (yellow and purple dashed lines) are also shown.

E. Future prospects

There are many future directions open for investigation with the techniques described in this section. The ion Coulomb coupling in UNPs formed by photoionizing laser cooled atoms is typically limited by disorder-induced heating⁵⁹ to $\Gamma_i \lesssim 5$, and an important goal for this research is to push toward stronger coupling. A step in this direction was recently taken by applying laser cooling to ions in the plasma, which yielded $\Gamma_i = 11$.⁴⁷ With different experimental configurations, it should be possible to use the forces from these laser beams to create thermal or velocity gradients, which would enable measurement of thermal conductivity and viscosity respectively, which are discussed in Sec. IV. It may be possible to explore connections between the theoretical tools of the memory function approach and the mean field kinetic

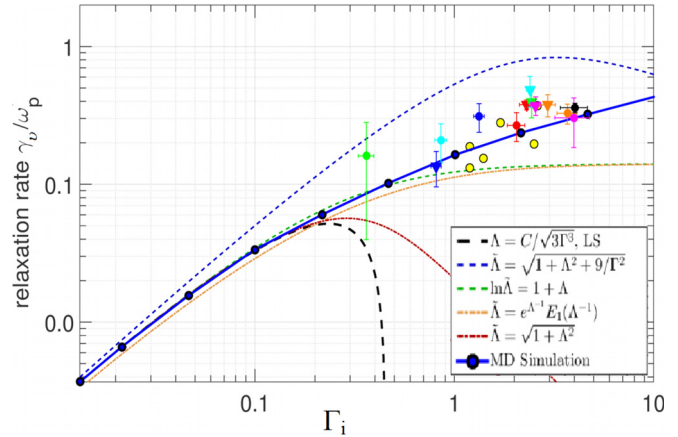


FIG. 17. Velocity relaxation rate γ_v as a function of ion coupling strength Γ_i measured in a strontium UNP using optical pumping and LIF. γ_v is normalized by the ion plasma oscillation frequency $\omega_p^{(i)}$. Data points are from Refs. 64 and 96. The thick solid line, which is obtained from MD simulations, approaches the LS form for the collision rate [Eq. (91)] in the weak-coupling limit (dotted line). Proposed replacements of Λ with $\tilde{\Lambda}$ given in the legend to extend (91) into the strongly coupled regime are discussed in Ref. 96. Reproduced with permission from Bannasch *et al.*, Phys. Rev. Lett. **109**, 185008 (2012). Copyright 2012 American Physical Society.

theory of Sec. II. We expect that using UNPs to measure transport properties of strongly coupled plasmas will be a productive area of research for many years to come.

VII. ELECTRON-ION COLLISION PHYSICS

Electron-ion collisions are a fundamental property of plasmas. Like HEDPs, UNPs are composed of electrons and ions, both of which can be influenced by strong-coupling physics, allowing the study of such strong coupling on electron-ion collision rates. These rates are relevant for electron-ion thermalization rates,¹⁸⁰ plasma stopping power,^{89–93} and transport properties.^{121,181,185} In particular, stopping power is relevant to HEDP experiments under fusion conditions.^{186,187} Sections II–IV in this review touch on these topics in different ways and discuss how strong coupling creates challenges in terms of proper understanding and theoretical treatment. UNPs provide an experimental system where these collision rates can be measured in an accessible manner. These UNPs are also straightforward to model numerically. This allows for tests of measured electron-ion collision rates as compared to predictions. Measurements of these rates under the influence of electron strong coupling are reviewed in this section. We show that even modest coupling in the electron system ($\Gamma_{ee} \lesssim 1$) influences the electron-ion collision rate.

A. Advantages of lower density UNPs

In our experiments, we formed UNPs through photoionizing a gas of ultracold atoms.¹⁰⁷ Using standard laser cooling and trapping techniques, we obtain a finite-spatial-extent gas in about a mm^3 volume consisting of approximately 10^7 ^{85}Rb atoms at a temperature of around $200 \mu\text{K}$. This gas was located in a UHV vacuum system where it was surrounded by a series of electrodes and open-area wire grids that can guide charges to a detector. In order to form the UNP, all the

trapping fields were removed and a controllable fraction of the atoms were photoionized in a two-step photoionization process. By tuning the frequency of the photoionization laser with respect to the ^{85}Rb ionization threshold, the initial kinetic energy of the free electrons produced in the photoionization was controlled. Given the finite extent of the gas, after photoionization some of the free electrons escaped and a space charge was produced that created a potential that confined the remaining electrons and formed the UNP. We deliberately worked with a small number of ions and electrons so that the UNPs that were created had lower densities.¹⁸⁸

In fact, in Refs. 107 and 189, UNPs have been created with a range of average densities, with average densities of 10^7 cm^{-3} and much higher. Working at higher or lower densities requires evaluating practical tradeoffs, but for measuring electron-ion collision rates and the influence of electron strong coupling on those rates lower densities are advantageous. The time scale for electron dynamics, the inverse of the electron plasma frequency, is longer at lower densities. This results in dynamics that are accessible to the speed of easily available electronics. Additionally, the way heating processes such as Rydberg atom formation and cooling mechanisms such as UNP expansion scale with changes in density mean that lower densities allow for higher electron values of Γ at both shorter and longer times.^{49,190,191} Further, electron evaporative cooling is more powerful at lower densities¹⁹² and it also contributes to larger electron Γ . Finally, given the constraints on the spatial size of the systems, lower densities mean lower number of electrons and ions, and this is advantageous for numerical modeling.

For instance, in our recent experiments,¹⁰⁷ the electron and ion numbers (N) have been on the order of 10^5 . The long-range nature of the Coulomb force complicates numerical modeling of plasmas by requiring either the calculation of $O(N^2)$ pairwise forces in each time step or using more sophisticated algorithms^{193,194} to reduce this scaling substantially. In either case, having a small N is a real advantage in performing calculations in a reasonable amount of time. To model our experiments, we chose to use GPUs and an OpenCL software implementation to perform $O(N^2)$ calculations rapidly, using a hardware solution to allow for an easier code implementation. Our typical simulation running time is a few hours for a single set of UNP conditions.

B. Initiating and measuring center-of-mass electron oscillations for electron-ion collision measurements

To measure the electron-ion collision rate, we induce a center-of-mass oscillation of the electrons by applying a short electric field pulse to create an impulse acceleration to “kick” the electrons on a time scale shorter than $1/\omega_p^{(e)}$. The UNP electrons oscillate in space with respect to the UNP ions, and that oscillation amplitude decreases with time. An example of the measured oscillation and decay rate obtained this way is shown in Fig. 18. The oscillation amplitude is determined by using a second kick for a controlled time after the first and then measuring the electrons ejected from the UNP with a charged particle detector.¹⁸⁸ The ejected electron number is a function of the phase and amplitude of the oscillation at the time of the second kick.

For most accessible UNP experimental conditions, this damping of the oscillation amplitude is not due to collisions but is rather due to the fact that the UNP density is not uniform throughout,¹⁰⁶ being peaked at the center and falling off with distance from the center. The nonuniformity in density leads to a coupling of the center-of-mass oscillation to other types of motion of the electrons. For instance, as

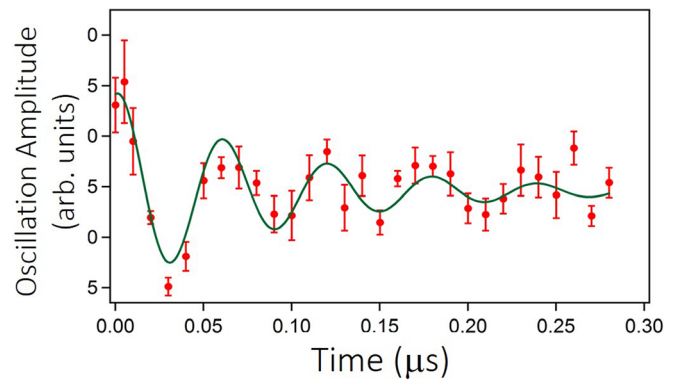


FIG. 18. Example electron center-of-mass oscillation decay signal. The red points represent the measured oscillation amplitude using a second kick as described in the main text. The solid green line is a damped cosine fit to the data.

the electrons oscillate into a region of lower ion density, the reduction in the confining force leads to an increase in the overall spatial size of the electron extent. The coupling of center-of-mass motion to other electron motion transfers energy and results in an effective damping (really a dephasing) of the center-of-mass oscillation.

However, through a careful arrangement of experimental conditions, the damping rate is instead dominated by electron-ion collision rates. The main arrangements needed are manipulating UNPs to produce a large charge imbalance such that the electrons are confined to the center of the UNP where the density is sufficiently uniform and working at cold enough electron temperatures. These conditions were implemented and electron-ion collision rates were determined from oscillation decay rates.¹⁰⁷

Relating the measured decay rate to predicted electron-ion collisions rates was done in two ways. In the first way, the damping rates were compared to a full molecular dynamics (MD) simulation that included both electrons and ions as pairwise interacting particles. Experimental damping measurements matched this molecular dynamics simulation with no free parameters, indicating that the molecular dynamics simulation included the relevant physics needed to model our UNPs.

While the full molecular dynamics model is useful for characterizing and understanding the UNP system, it does not in and of itself allow for comparison of the measured decay rates to general theoretical models of electron-ion collisions. In order to accomplish that task, separate simulations were performed where the electrons were all modeled as Coulomb-interacting point particles but the ions were not. Instead, the overall confinement of the electrons by the ions was modeled via a continuous charge distribution that matched the average ion density distribution. Then, electron-ion collisions were modeled as binary collisions that had a probability of occurring randomly in each time step of the simulation. The cross section for the binary collision and the resulting distribution of scattering angles can be computed from any particular theory of electron-ion collisions, allowing a comparison to experimental results.

C. Comparison of measured electron-ion collision rates to theoretically predicted rates

The computation of cross section and scattering angle is not without difficulty owing to commonly made approximations used to

obtain electron-ion collision rates, however. As discussed in Secs. II and III, the long-range nature of the Coulomb force produces a divergence in the computation of the collision cross section. The most common result is to include a Coulomb logarithm in the collision rate.

Having an experimental measurement of electron-ion collision rates under conditions of moderate strong coupling with Γ_{ee} at 0.1 and 0.35 allows an experimental test of expressions for Coulomb logarithms made under often-used sets of assumptions. Given that this coupling is not that strong, it is reasonable to ask if coupling considerations are relevant in any substantial way—and it turns out they are. We compare our experimentally measured rates to Coulomb logarithm formulations that increasingly incorporate strong coupling considerations and remove common but potentially problematic assumptions [see, in particular, the discussion around Eqs. (39)–(41)]. The steady improvement of the comparison of predictions and experimental results provides validation for the need for the more sophisticated collision treatments described in Secs. II and III.

The comparison of measured electron damping rates at two electron temperatures, full MD simulation-derived damping rates, and predicted damping rates are shown in Table I. For the damping rates, we have used three different formulations of the Coulomb logarithm. The first is

$$CL1 = \ln \left(\frac{0.765}{\sqrt{3}\Gamma^3} \right). \tag{94}$$

This expression is expected to be valid in the weak-coupling limit.¹⁴⁷ It is computed using perturbation theory for energy loss of nonrelativistic particles moving through a highly ionized plasma. The second formulation of the Coulomb logarithm is

$$CL2 = \ln \left(1 + \frac{0.765}{\sqrt{3}\Gamma^3} \right). \tag{95}$$

This expression is consistent with a theoretical treatment that extends stopping power and electron-ion thermalization calculations into the strong-coupling regime.^{89,180,181} It is accurate for $\Gamma \leq 10$. The Coulomb logarithms in Eqs. (94) and (95) are simple analytic functions. While that is convenient, it requires particular approximations

TABLE I. Comparison of measured and calculated oscillation damping rates for two experimental conditions and associated ratios.¹⁰⁷ The rate type of “measured” corresponds to the experimentally measured damping rates for a colder [$\Gamma = 0.35(8)$] and hotter [$\Gamma = 0.15(4)$] experimental condition. The “full MD” rate corresponds to the rate extracted from explicitly modeling all ions and electrons as point charges as described in the main text. The “CL” rate types correspond to calculated rates, given different Coulomb logarithms as defined in the main text. Each number in a ratio column is the ratio of the measured damping rate for the appropriate experimental conditions to the calculated rate immediately to the left, including uncertainties. All rates are in units of μs^{-1} .

Rate Type	$\Gamma = 0.35(8)$	Ratio	$\Gamma = 0.15(4)$	Ratio
Measured	8.53 ± 1.54		3.72 (79)	
Full MD	7.65	1.12 (20)	4.44	0.84 (18)
CL 1	2.69	3.17 (57)	2.42	1.54 (33)
CL 2	3.41	2.50 (45)	2.77	1.34 (29)
CL 3	5.56	1.53 (28)	3.67	1.01 (22)

to prevent having the Coulomb logarithm be expressed as an integral as discussed in Secs. II and III.

The third formulation of the Coulomb logarithm is

$$CL3 = \int_0^\infty \zeta d\zeta \exp \left[-\frac{\zeta^2}{2} \ln \left(1 + \frac{\alpha \zeta^4}{3\Gamma^3} \right) \right]. \tag{96}$$

This is a generalized Coulomb logarithm¹⁸¹ from Sec. II and should be accurate for $\Gamma \leq 20$. The parameter α is a constant that is determined for a given value of Γ by requiring a match to the predictions of Refs. 89, 180, and 181 for electron-ion thermalization rates or stopping power as appropriate. For our measured values of electron, these different expressions predict different oscillation damping rates that can be compared to the experimentally determined values.

The Coulomb logarithms are translated to collision differential cross sections by assuming Rutherford scattering for the electron-ion collisions with a hard maximum limit on the impact parameter. The Coulomb logarithm then determines the value of this impact parameter limit as a function of electron velocity and plasma conditions. This means that the choice of the Coulomb logarithm determines both the magnitude and the functional form of the contribution of different velocity electrons to the oscillation damping. This is illustrated in Fig. 19, which is comparable to Fig. 7 of Ref. 121 and related strongly to the discussion in that work.

While our values of the electron Γ are less than 1, the influence of strong coupling is substantial for the coldest condition and not insignificant for the hottest condition. For the colder measured temperature, the weak coupling Coulomb logarithm is a factor of 3 less than the measured rate.

The simple extension to the Coulomb logarithm to account for strong coupling in “CL 2” does not do much better, however, despite being sufficient for calculations of other plasma quantities. Abandoning the simple expression in a way that allows for a better treatment (“CL 3”), however, produces a much better match.

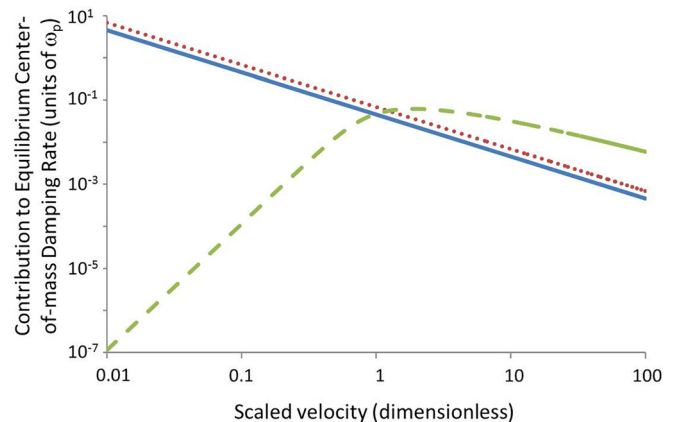


FIG. 19. Center-of-mass damping rate contribution vs electron velocity for different Coulomb logarithms. Integrating this rate over the electron velocity distribution produces the total damping rate. The parameter $\Gamma = 0.35$ for the curves in this plot. The solid (blue) curve corresponds to CL 1, the dotted (red) curve to CL 2, and the dashed (green) curve to CL 3 in Table I. The velocity in units of $\sqrt{\frac{kT}{m}}$ where k is Boltzmann’s constant, T the electron temperature, and m the electron mass.

The explanation for why CL 2 works in other strongly coupled plasma contexts but not this one is the velocity dependence shown in Fig. 19 combined with the fact that for processes like stopping power and electron-ion thermalization, the time scales are longer than the electron dynamics time scale $1/\omega_p^{(e)}$, while for oscillation damping the time scale of the damping is far closer to $1/\omega_p^{(e)}$ for sufficient strong coupling. Integrating the CL 2 and CL 3 curves in Fig. 19 over a thermal equilibrium electron distribution produces the same average instantaneous result. During the time scale of an oscillation, though, lower-velocity-electron collisions can essentially saturate, giving the oscillation damping more sensitivity to higher-velocity collisions. This work thus illustrates the need for caution in applying Coulomb logarithms in any strongly coupled plasma. This caution goes beyond just finding a suitable expression, but also requires an evaluation of dynamical considerations and an appropriate application of commonly used approximations. Even for what might seem to be a mild value of $\Gamma = 0.35$, strongly coupling effects can be substantial, and the need for careful treatment of Coulomb logarithms discussed in Refs. 121 and 181 and Secs. II and III of this paper is illustrated and justified by these measurements.

D. Future investigations

While not yet resolved beyond about two standard deviations by measurement, the remaining $\sim 37\%$ discrepancy between full MD calculation and predicted CL 3 damping rate indicates that relevant considerations have not yet been fully identified. The CL 3 rate is ultimately derived from an approximate model of collisions that has unphysical elements (e.g., a hard limit on impact parameter). A screened Coulomb potential such of that in Ref. 121 and the associated extensions to the Coulomb logarithm would be much better justified, but a naive application of that potential actually increased the discrepancy. However, the electron-ion collisions described here are not likely going to be described accurately by an ion transport theory. In particular, the fact that the collisions are occurring between unlike-signed particles has been found to be significant for these conditions as detailed in Ref. 98 and Sec. II. Using collisions differential cross sections derived from Ref. 98 predicts the damping rate of $5.80 \mu\text{s}^{-1}$ for our experimental conditions. This is a slight numerical improvement in agreement from CL 3. More importantly, though, using the theory from Ref. 98 is far better justified on the basis of being a physically reasonable potential and puts experimental measurement and theory comparison on a much sounder basis.

Further preliminary investigations indicate that the remaining difference is likely due to the fact that in addition to binary collisions, three-body collisions are significant for these values of Γ . The incorporation of the theory of Ref. 98 and the characterization of the importance of three-body collisions are the subjects of present work that are planned to appear in a future publication. Additionally, measurements of electron-ion collisions are being performed in UNPs where the electrons are strongly magnetized, seeking to determine the effect of magnetic fields on these collision rates.¹⁰⁹ The field of transport measurements in magnetized plasmas, such as is mentioned at the end of Sec. II, is an exciting area of future HEDP/UNP overlap. Modest laboratory fields of less than 1 T will fully magnetize the UNP electrons.

VIII. MOMENTUM TRANSFER IN DUAL-SPECIES ULTRACOLD NEUTRAL PLASMAS

As we have seen in this review, the description of transport and thermodynamic properties of plasmas hinges critically on the Coulomb logarithm, $\ln \Lambda$. Operationally, the Coulomb logarithm can be considered as a density- and temperature-dependent correction factor that multiplies two-body collision cross sections and rates in kinetic calculations.¹⁹⁵ In that picture, it represents the averaged contributions of the (typically) millions of Coulomb collision partners at large impact parameters. See Ref. 121 for a detailed discussion.

In the Landau-Spitzer treatment, as discussed in Sec. III C, the Coulomb logarithm is conveniently written as $\ln \Lambda = \ln(\lambda_D/r_0)$, where the λ_D is the electron Debye length and r_0 is the classic distance of closest approach [see Eq. (33)]. Its value ranges from 10 to 20 for weakly coupled plasmas. However, when the plasmas become strongly coupled, the value of the CL becomes small and this simplistic treatment must be modified.

Inherent in the CL are assumptions about how to treat both the electrons and the ion-ion interactions. These assumptions are represented using an effective ion-ion interaction potential. One example is the Yukawa interaction presented in Secs. I and III. Another example is the potential of mean force presented in Sec. II. In this model, the ion pair distribution is determined using thermodynamic considerations, and the resulting potential is used in calculating the cross sections for plasma processes. Both of these treatments have their relative strengths and limitations in different regimes of strong-coupled in the plasma.

Ultracold neutral plasmas (UNPs) span the phase space region where the Coulomb logarithm values are typically less than 1 (see Fig. 1). These systems have enabled the studies of plasma dynamics and evolution in a highly idealized environment,^{17,18} serving, in a way, as high-energy-density plasma simulators.^{55,196}

In this section, we present a recent study comparing simulations and measurements of the velocity distribution in a dual-species UNP, using Ca^+ and Yb^+ ions. The details of this work have been published recently.¹¹⁵ The simulation uses a two-fluid model with two representations of the friction force between the ions. Those simulations reproduce the main features of the measured ion velocity distribution. Surprisingly, we find that at this level of comparison the two different approaches yield similar simulated results and both agree well with the experiment. With more detailed diagnostics, this system will provide a unique platform for future studies of collision physics in strongly coupled plasmas. In this system, it should be possible to study idealized versions of classic plasma problems such as interspecies diffusion,¹⁹⁷ multispecies plasma expansion,¹⁹⁸ two-stream instabilities, the sensitivity of bump-on-tail evolution to electron screening,¹⁹⁹ shock evolution,^{200,201} and evaluations of the Coulomb logarithm when the plasma approaches the nonideal state.^{72,121}

A. Experiment

The experiment begins by trapping 20×10^6 neutral Ca and Yb atoms in a MOT. The spatial density profile is Gaussian, $n = n_0 \exp(-r^2/2\sigma^2)$. In order to minimize spatial inhomogeneities in the neutral atom clouds stemming from imperfect laser beams and unbalanced radiation pressure, the neutral atoms are allowed to expand for 100 μs in the dark before formation of the plasma.

The neutral atoms in the MOT are resonantly ionized using ns-duration laser pulses in a two-step process. The initial electron temperature in the plasma is determined by varying the wavelengths of the 390 nm (Ca) and 395 nm (Yb) laser pulses. The electron temperature is equal to the ionizing laser's photon energy above the ionization energy. In experiments reported here, the electron temperature is $T_e = 96$ K.

The initial ion densities are determined by varying the intensity of these same ionizing laser pulses. With our few-millijoule pulses, we can ionize all of the Ca atoms and up to 60% of the Yb atoms. The density is nearly spherically symmetric and Gaussian, and we approximate the density as $n(r) = n_0 \exp(-r^2/2\sigma_0^2)$. The peak density of the Ca^+ plasma is $n_0 = 1.8 \times 10^{10} \text{ cm}^{-3}$ with an initial rms size of $\sigma_0 = 0.29$ mm. The peak density of the Yb^+ plasma in the experiments reported here varies from $n_0 = 0.2 \times 10^{10} \text{ cm}^{-3}$ to $n_0 = 1.8 \times 10^{10} \text{ cm}^{-3}$ with an initial rms size of $\sigma_0 = 0.37$ mm. The cycle of cooling and trapping the neutral atoms and ionizing them to form a plasma is repeated 10 times per second.

The time-evolving Ca^+ ion velocity distribution is determined using laser-induced fluorescence measurements at 397 nm.²⁰² Examples of velocity distribution measurements are shown in Fig. 20. A linearly polarized probe laser beam at 397 nm passes through the plasma and is retro-reflected. The single-beam intensity is $I = 50 \text{ mW/cm}^2 \approx I_{\text{sat}}$. A strong laser beam ($I = 2000 \text{ mW/cm}^2$) at 850 nm is used to minimize optical pumping of the Ca^+ ions into dark

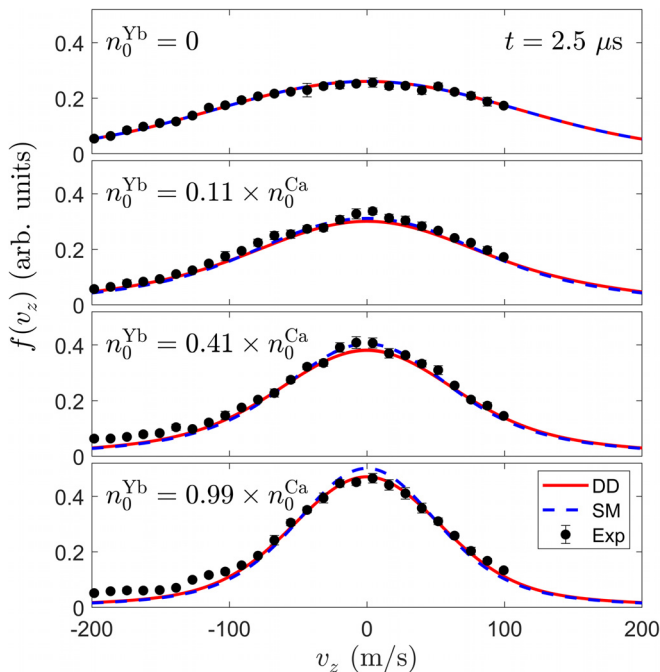


FIG. 20. A comparison of the experimental data (black circles) and the fluid code simulations (red and blue lines) for a range of initial Yb^+ densities. This plot shows the $f(v_z)$ velocity distribution after $t = 2.5 \mu\text{s}$ of plasma evolution. As the Yb^+ density increases, the Ca^+ velocity distribution becomes narrower. At time $t=0$ the calcium ion density in the center of the plasma is $n_0^{\text{Ca}} = 1.8 \times 10^{10} \text{ cm}^{-3}$. The initial Ca rms size is $\sigma_0 = 0.29$ mm. For Yb the initial rms size is $\sigma_0 = 0.37$ mm. The initial electron temperature is $T_e = 96$ K.

states. The size of these laser beams is large compared to the size of the plasma. Both laser beams illuminate the entire plasma for the duration of the experiment.

When the frequency of the probe laser is detuned by a frequency $\Delta\omega = 2\pi \times (f - f_0)$ from the atomic resonance frequency, f_0 , the fluorescence signal is proportional to the number of ions Doppler-shifted into resonance with the laser beam. We initially adjust the 397 nm probe laser frequency to a particular detuning $\Delta\omega$ and measure the fluorescence from the plasma ions as a function of time. The ions are initially at rest but accelerate outward due to the ambipolar field, and the fluorescence signal rises and falls as more or fewer ions move into a velocity class with a Doppler shift equal to $\Delta\omega$. To improve the signal-to-noise ratio, we typically average the fluorescence signal over 30 plasmas. In other words, we will cool, trap, and ionize our neutral atoms to form a plasma and then measure the fluorescence from the expanding plasma 30 times for a given probe laser frequency. By repeating this cycle for a range of different probe laser frequencies, we are able to map out the v_z velocity distribution as a function of time, averaged over the entire plasma.

B. The fluid simulation

To interpret the experimental results, we have built a two-fluid 1-d code in spherical coordinates. A kinetic treatment would probably be more appropriate. However, the mean free path in the bulk of the plasma is small enough that a fluid treatment should give reasonably reliable insight. The two species are denoted by the subscript s , and it is assumed that the important physical effects are convection, adiabatic expansion, pressure acceleration, acceleration by an ambipolar electric field, and interspecies friction, including Joule heating due to the relative velocity between the two species. Our plasma is not very strongly coupled, so we assume that the monatomic ideal gas law is the equation of state for both species, so that each one has a distribution function approximated by a drifting Maxwellian and so that each species has adiabatic exponent $\gamma = 5/3$. For our conditions, viscous effects, the thermal force, and ion thermal conduction are small and are not included in the fluid equations. With these assumptions, the three equations to be solved for each species are

$$\frac{\partial n_s}{\partial t} + u_s \frac{\partial n_s}{\partial r} = -n_s \nabla \cdot (u_s \hat{r}), \quad (97)$$

$$\frac{\partial T_s}{\partial t} + u_s \frac{\partial T_s}{\partial r} = -\frac{2}{3} T_s \nabla \cdot (u_s \hat{r}) + \frac{2}{3n_s k_B} Q_{ss'}, \quad (98)$$

$$\frac{\partial u_s}{\partial t} + u_s \frac{\partial u_s}{\partial r} = -\frac{k_B}{n_s m_s} \frac{\partial n_s T_s}{\partial r} - \frac{k_B T_e}{n_s m_s} \frac{\partial n_s}{\partial r} + \frac{F_{ss'}}{m_s}. \quad (99)$$

In these equations, (n_s, T_s, u_s) are, respectively, the density, temperature, and radial fluid velocity for species s . The quantity $F_{ss'}$ is the interspecies friction force and $Q_{ss'}$ is a term representing frictional heating and temperature equilibration between the two species.

1. The interspecies friction force

To compute the interspecies friction force $F_{ss'}$ and the heating term $Q_{ss'}$, we follow the treatment of Baalrud and Daligault in Ref. 76, including the energy exchange density in Eqs. (44) through (51) of that reference. Our friction force $F_{ss'}$ is given in terms of their fluid friction force density $\mathbf{R}^{ss'}$ by

$$F_{ss'} = \frac{\mathbf{R}^{ss'}}{n_s} = -\frac{16}{3} \frac{\sqrt{\pi} e^4 n_{s'}}{(4\pi\epsilon_0)^2 m_{ss'}^2 \bar{v}_{ss'}^3} \Xi(\Delta\bar{V})(\mathbf{u}_s - \mathbf{u}_{s'}), \quad (100)$$

where $m_{ss'}$ is the reduced mass $m_{ss'} = m_s m_{s'} / (m_s + m_{s'})$ and $\bar{v}_{ss'} = (2k_B T_s / m_s + 2k_B T_{s'} / m_{s'})^{1/2}$. The quantity $\Delta\bar{V} = |\mathbf{u}_s - \mathbf{u}_{s'}| / \bar{v}_{ss'}$, where \mathbf{u}_s and $\mathbf{u}_{s'}$ are the species fluid velocities. The particle velocities \mathbf{v}_s and $\mathbf{v}_{s'}$ of the two species are assumed to be distributed according to two Maxwellians flowing relative to each other with relative velocity $\Delta V = \mathbf{u}_s - \mathbf{u}_{s'}$.

The quantity $\Xi(\Delta\bar{V})$ is a generalized Coulomb logarithm and is given by

$$\Xi(\Delta\bar{V}) = \frac{3}{16} \frac{1}{\Delta\bar{V}^3} \frac{1}{2} \int_0^\infty d\xi \xi^2 \frac{\sigma_{ss'}^{(1)}(\xi)}{\sigma_0} \mathcal{X}, \quad (101)$$

where the function \mathcal{X} is

$$\mathcal{X} = \left[(2\xi\Delta\bar{V} + 1) e^{-(\xi+\Delta\bar{V})^2} + (2\xi\Delta\bar{V} - 1) e^{-(\xi-\Delta\bar{V})^2} \right], \quad (102)$$

where $\sigma_{ss'}^{(1)}(\xi)$ is the usual first momentum transfer cross section,⁷⁶ ξ is the ratio of the particle velocity v_s to the thermal velocity $v_{Ts} = \sqrt{2k_B T_s / m_s}$, and

$$\sigma_0 = \frac{\pi e^4}{(4\pi\epsilon_0)^2 m_{ss'}^2 \bar{v}_{ss'}^4}. \quad (103)$$

Once this friction force is computed, we use it in Eqs. (98) and (99) of the fluid model.

Baalrud and Daligault compute the energy exchange and frictional heating term $Q_{ss'}$ similarly. They find

$$Q_{ss'} = -\frac{16\sqrt{\pi} n_s n_{s'} e^4 k_B}{(4\pi\epsilon_0)^2 m_s^2 \bar{v}_{ss'}^3} \Xi(\Delta\bar{V})(T_s - T_{s'}) - \frac{v_{Ts}^2}{\bar{v}_{ss'}^2} \Delta\mathbf{V} \cdot \mathbf{R}^{ss'}, \quad (104)$$

where

$$\Xi(\Delta\bar{V}) = \frac{1}{8\Delta\bar{V}} \int_0^\infty d\xi \xi^4 \frac{\sigma_{ss'}^{(1)}(\xi)}{\sigma_0} [e^{-(\xi-\Delta\bar{V})^2} - e^{-(\xi+\Delta\bar{V})^2}]. \quad (105)$$

This term may then be used in Eq. (98) of the fluid model.

The code is built on a cell-centered spherical grid with $r_i = (i - \frac{1}{2})\Delta r$, $i = 1, 2, 3, \dots$, with r the spherical radial coordinate and with Δr the constant grid spacing. We solve these equations using the method of characteristics.

To handle the nonconvective parts of the time advance, a simple two step predictor-corrector method is used. In the first step, old values of (n_s, T_s, u_s) are used to advance to time level $m + 1/2$. In the second step, these intermediate values are used to advance (n_s, T_s, v_s) to time level t^{m+1} .

2. The Coulomb logarithm and momentum transfer

We have studied two treatments of momentum transfer. The first uses the usual Coulomb cross section, modified by a suitable generalization of $\ln \Lambda$.¹⁸⁰ As shown in Ref. 76, for this case the friction force generalized Coulomb logarithm $\Xi(\Delta\bar{V})$ is given by

$$\Xi(\Delta\bar{V}) = \frac{3\sqrt{\pi}}{4} \frac{\psi(\Delta\bar{V}^2)}{\Delta\bar{V}^3} \ln \Lambda, \quad (106)$$

where

$$\psi(x) = \operatorname{erf}(\sqrt{x}) - \frac{2}{\sqrt{\pi}} \sqrt{x} e^{-x}. \quad (107)$$

Similarly, the Baalrud-Daligault effective Coulomb logarithm for energy exchange $\tilde{\Xi}(\Delta\bar{V})$ in the case of Coulomb scattering with a Coulomb logarithm multiplier is given by

$$\tilde{\Xi}(\Delta\bar{V}) = \frac{\sqrt{\pi}}{2\Delta\bar{V}} \operatorname{erf}(\Delta\bar{V}) \ln \Lambda. \quad (108)$$

For the case of electron-ion temperature relaxation, molecular dynamics simulations¹⁸⁰ indicate that a Coulomb logarithm of the form

$$\ln \Lambda = \ln(1 + C/g) \quad (109)$$

is appropriate, where $C=0.7$ and $g = (e^2/4\pi\epsilon_0)[1/(\lambda_{De} k_B T_e)]$ is the so-called plasma parameter. Effective potential theory calculations suggest that this might be appropriate for our dual-species plasma as well.⁷³

Because we are calculating ion-ion momentum transfer, some caution is in order. In the Naval Research Laboratory Plasma Formulary, the plasma parameter is $g = r_{\min}/r_{\max}$. For ion-ion collisions in flowing Maxwellians,

$$g = \frac{e^2}{4\pi\epsilon_0} \left[\lambda_D \left(\frac{1}{2} m_{ss'} \right) \left(\bar{v}_{ss'}^2 + \frac{2}{3} |u_s - u_{s'}|^2 \right) \right]^{-1}, \quad (110)$$

where the Debye length λ_D includes both the ion contribution and a correction due to ion flow and strong coupling, as given in Ref. 121,

$$\frac{1}{\lambda_D^2} = \frac{1}{\lambda_e^2} + \sum_i \frac{1}{\lambda_i^2} \left(\frac{1}{1 + (u_s - u_{s'})^2 / v_{th,i}^2 + 3\Gamma_i} \right), \quad (111)$$

where the summation is over the ion species and $v_{th,i} = (2k_B T_i / m_i)^{1/2}$. Consistent with Ref. 57 and many other UNP studies, we take the ion strong coupling parameter to be

$$\Gamma_i \equiv \frac{e^2}{4\pi\epsilon_0 a_{ws} k_B T_i} = 2.3. \quad (112)$$

Near the center of the plasma, where the density is the highest, the value of the plasma parameter defined in Eq. (43) is $g = 2.6$.

The second form for the momentum transfer cross section uses the Debye-screened Coulomb potential described by Stanton and Murillo in Sec. III and Appendix C, Eq. (41), of Ref. 121. The collision integrals in this reference are expressed as convenient functions of the plasma parameter, g , as discussed above. Using the screened Coulomb cross section cited above,¹²¹ the integral in Eq. (101) was performed numerically and fit to an analytic form for use in the fluid code. In this treatment, the energy exchange term is density-weighted, as opposed to velocity-weighted in the Baalrud-Daligault treatment, and the temperature equilibration term was neglected since its effect turned out to be small when comparing the simulation to the experiment.

3. The velocity distribution $f(v_z)$

In order to compare the fluid code directly with the experimental measurements, we calculate the v_z velocity distribution from the

simulation results for $u(r)$, $n(r)$, and $v_{th}(r)$. In doing so, we assume that the particles of each species are drifting Maxwellians with the parameters given in the previous sentence, and we integrate over all 3 dimensions in space and over v_x and v_y in velocity space to obtain the following distribution in v_z :

$$f(v_z) \propto \int_0^\infty \frac{n(r)}{u(r)} \left[\operatorname{erf} \left(\frac{u(r) - v_z}{v_{th}} \right) + \operatorname{erf} \left(\frac{u(r) + v_z}{v_{th}} \right) \right] r^2 dr, \quad (113)$$

where $v_{th} = (2k_B T/m)^{1/2}$. We evaluate this integral numerically. Note that normalizing constants have been omitted since the experimental data are not normalized.

C. Comparing simulation with experiment

In Fig. 20, we plot a comparison of the experiment and the fluid code simulations. This figure shows the Ca^+ velocity distribution $f(v_z)$, averaged over the entire plasma. The experimental data are corrected for the estimated effects of optical-pumping into the “dark” D states. The simulation data are convolved with a Lorentzian line shape corresponding to the natural linewidth of the atomic transition in order to be directly compared with the experiment.

The top panel of Fig. 20 shows the results for a pure calcium plasma. The simulations reproduce the analytic solution from Ref. 176. Because there is no Yb^+ plasma, there is no interspecies ion-ion friction force.

The two middle panels and the bottom panels show that the Ca^+ velocity distribution narrows with the addition of Yb^+ ions in the plasma. This demonstrates the increasingly important influence of the friction force between the two species. In the absence of interspecies ion-ion friction, the density gradient would accelerate all of the Ca^+ ions radially outward. Instead, we see collisional locking of the two plasma species near the center of the plasma. For the highest densities, the wings of the velocity distribution rise, indicating the presence of a class of Ca^+ ions accelerated by the Yb^+ plasma density gradient in spatial locations where the friction force is small.

In the bottom panel of Fig. 20, we also see that the experimental data rise above the simulation data in the high-velocity wings of the distribution. This is probably due to kinetic effects not included in the fluid code simulations.

D. Discussion and future directions

The fluid code simulations reproduce the main features of the dual-species plasma expansion. Both treatments of momentum transfer result in simulated velocity distributions that largely agree with each other and with the experimental data. This result is somewhat surprising and yet encouraging. It is surprising because the assumptions going into the two formulations are so different. In one, near-equilibrium thermodynamic physics is used to find the average ion positions in the plasma. This, in turn, is used to derive the potential of mean force, a momentum transfer cross section, and a generalized “Coulomb logarithm.” In the other, a Yukawa interaction is assumed, using a strong-coupling-corrected screening length. The agreement between the two approaches is encouraging because it lends some confidence regarding the viability of either approach. We plan to explore the validity of these two approaches in carefully designed experiments. For example, the simulations appear to predict different ion temperatures in the wings of the velocity distribution.

One way to gain deeper insight into collisional processes in the plasma is to spatially resolve the velocity distribution. This approach has been beautifully described in Sec. VI. We are in the process of making these measurements in our dual-species ultracold neutral plasmas at BYU. In preliminary measurements, we see ion heating where the density gradient is highest, where Joule heating occurs due to interspecies ion-ion friction. As this work is in its infancy, we do not include it here.

IX. CONCLUSION AND OUTLOOK

In this review article, we have provided a brief overview of some aspects of HEDP theory and UNP experiments. The HEDP experiments included in this overview are those that reside in the upper right-hand corner of Fig. 2. As shown in Fig. 1, these plasmas find overlap in the moderately coupled ($\Gamma = 0.1 - 10$) and moderately screened ($\kappa \leq 1$) region of $\kappa\Gamma$ space.

We have shown that UNP experiments can be used to test HEDP theory and calculations—something that UNP experiments share in common with other table-top-scale experiments. For UNPs, the combination of low temperature and low density make it possible to use high-precision laser spectroscopy and charged-particle detection to measure the evolution of the plasma density, electron temperature, and ion velocity distribution with high reliability and, under some conditions, in real time. In the context of the YOCP model, appropriate energy-, distance-, and time-scaling of UNP measurements enable direct comparison of relaxation rates and transport properties between UNP and HEDP plasmas. The UNP measurements can also be used to verify open boundary calculations using molecular-dynamics codes in the strongly coupled regime.

One example of the HEDP/UNP crossover is DIH, which had been observed in HEDP simulations and experiments but not explained. UNP work has shown that kinetic-energy oscillations and the interaction quench are universal characteristics of YOCPs. Another example is in momentum transfer. Measurements of ion friction in the hydrodynamic expansion of dual-species UNPs were reproduced using both the effective potential theory of Sec. II and the effective Boltzmann equation of Sec. III. As a third example, electron oscillation damping rates are probing electron-ion thermalization and other effects in strongly coupled plasmas.

As mentioned throughout this overview, there are many areas of future potential overlap. One exciting area is in magnetized plasmas. Modest laboratory fields can completely magnetize the electrons in UNPs. A field of 1 T would also magnetize the ions. Then ion transport properties could be measured and compared to HEDP codes. Viscosity and conductivity could be measured, specifically in the new and comparatively larger $\Gamma = 11 \text{ Sr}^+$ plasmas. Multispecies diffusion, relaxation, and collisional heating could be measured in the dual-species plasmas of Sec. VIII, the Rydberg plasmas of Sec. V, and the electron studies of Sec. VII. These multispecies measurements could be helpful in multiphysics code development (see Sec. IV). The interaction of microwave radiation with UNPs is analogous to laser radiation interacting with overdense plasmas, and this connection could also be explored. Stopping power has been mentioned in this overview, and the exquisite measurement capabilities of UNPs suggest that it may be possible to measure this effect directly in carefully designed experiments. Finally, measurements in geometries other than the spherically symmetric or Gaussian ellipsoidal shapes could provide

access to flow- or pressure-induced instabilities. We hope that this overview will inspire these and other possibilities in the HEDP/UNP crossover.

ACKNOWLEDGMENTS

Many colleagues, students, and funding agencies have contributed to this work included in this review. It would not have been possible to carry out these many experiments, simulations, calculations, and theoretical developments without them. The U. S. Air Force Office of Scientific Research, the National Science Foundation, Lawrence Livermore National Laboratory, LLNL High Energy Density Science Center,²⁰³ and the U. S. Department of Energy have all contributed significant financial support, facilities and personnel support, and encouragement.

S. D. Baalrud acknowledges support from the U. S. Air Force Office of Scientific Research under Award No. FA9550-16-1-0221, the U. S. Department of Energy, Office of Fusion Energy Sciences, under Award No. DE-SC0016159, and the National Science Foundation under Award No. PHY-1453736. The work presented here was done in collaboration with N. Shaffer, S. Tiwari, J. Daligault, C. Starrett, and D. Saumon.

S. D. Bergeson acknowledges support from the National Science Foundation (Grant No. PHY-1500376) and the U. S. Air Force Office of Scientific Research under Award No. FA9550-17-1-0302. He gratefully acknowledges critical contributions to the dual-species UNP work by Ross L. Spencer and R. Tucker Sprengle.

The work of C. L. Ellison was performed under the auspices of the U.S. Department of Energy by Lawrence Livermore National Laboratory under Contract No. DE-AC52-07NA27344. This document was prepared as an account of work sponsored by an agency of the United States government. Neither the United States government nor Lawrence Livermore National Security, LLC, nor any of their employees makes any warranty, expressed or implied, or assumes any legal liability or responsibility for the accuracy, completeness, or usefulness of any information, apparatus, product, or process disclosed, or represents that its use would not infringe privately owned rights. Reference herein to any specific commercial product, process, or service by trade name, trademark, manufacturer, or otherwise does not necessarily constitute or imply its endorsement, recommendation, or favoring by the United States government or Lawrence Livermore National Security, LLC. The views and opinions of authors expressed herein do not necessarily state or reflect those of the United States government or Lawrence Livermore National Security, LLC, and shall not be used for advertising or product endorsement purposes.

E. Grant acknowledges support from the U.S. Air Force Office of Scientific Research (Grant No. FA9550-17-1-0343), together with the Natural Sciences and Engineering research Council of Canada (NSERC), the Canada Foundation for Innovation (CFI), and the British Columbia Knowledge Development Fund (BCKDF).

The work of F. Graziani was performed under the auspices of the U.S. Department of Energy by Lawrence Livermore National Laboratory under Contract No. DE-AC52-07NA27344.

T. C. Killian acknowledges support from the Air Force Office of Scientific Research through Grant No. FA9550-17-1-0391 and by the NSF/DOE Partnership in Basic Plasma Science and Engineering through the DOE/SC Office of Fusion Energy Sciences Grant No. DE-

SC0014455. He gratefully acknowledges critical contributions from numerous graduate students and postdoctoral researchers who worked on the ultracold plasmas experiment at Rice University: V. S. Ashoka, Y. C. Chen, H. Gao, T. Strickler, S. Laha, P. Gupta, S. B. Nagel, C. E. Simien, Y. N. Martinez, P. G. Mickelson, J. Castro, P. McQuillen, T. Langin, Grant Gorman, and MacKenzie Warrens.

J. Roberts acknowledges support from the Air Force Office of Scientific Research under Grant Nos. FA 9550-12-1-0222 and FA9550-17-1-0148. He gratefully acknowledges the contributions of Colorado State University graduate students Wei-Ting Chen, John Guthrie, Puchang Jiang, Truman Wilson, and Craig Witte who worked on the low-density UNP efforts described in this part of the review.

REFERENCES

- ¹R. Paul Drake, *High-Energy-Density Physics: Foundation of Inertial Fusion and Experimental Astrophysics (Graduate Texts in Physics)* (Springer, 2018).
- ²S. Atzeni and J. Meyer-Ter-Vehn, *The Physics of Inertial Fusion* (Clarendon Press, Oxford, UK, 2004).
- ³R. T. Farouki and S. Hamaguchi, "Thermodynamics of strongly-coupled Yukawa systems near the one-component-plasma limit. II. Molecular dynamics simulations," *J. Chem. Phys.* **101**, 9885 (1994).
- ⁴M. Baus and J.-P. Hansen, "Statistical mechanics of simple Coulomb systems," *Phys. Rep.* **59**(1), 1–94 (1980).
- ⁵S. Hamaguchi, R. T. Farouki, and D. H. E. Dubin, "Triple point of Yukawa systems," *Phys. Rev. E* **56**, 4671–4682 (1997).
- ⁶E. E. Salpeter and H. M. Van Horn, "Nuclear reaction rates at high densities," *Astrophys. J.* **155**, 183 (1969).
- ⁷D. Stevenson, "The condensed matter physics of planetary interiors," *J. Phys. Condens. Matter* **41**, 53 (1980).
- ⁸B. A. Remington, R. P. Drake, and D. D. Ryutov, "Experimental astrophysics with high power lasers and Z pinches," *Rev. Mod. Phys.* **78**, 755 (2006).
- ⁹J. Lindl, "Development of the indirect-drive approach to inertial confinement fusion and the target physics basis for ignition and gain," *Phys. Plasmas* **2**, 3933 (1995).
- ¹⁰P. K. Shukla and A. A. Mamun, *Introduction to Dusty Plasma Physics* (CRC Press, 2015).
- ¹¹A. Schella, M. Mulsow, and A. Melzer, "Correlation buildup during recrystallization in three-dimensional dusty plasma clusters," *Phys. Plasmas* **21**, 050701 (2014).
- ¹²A. Pielt and A. Melzer, "Dynamical processes in complex plasmas," *Plasma Phys. Controlled Fusion* **44**(1), R1–R26 (2002).
- ¹³M. Bonitz, C. Henning, and D. Block, "Complex plasmas: A laboratory for strong correlations," *Rep. Prog. Phys.* **73**(6), 066501 (2010).
- ¹⁴F. Westermeier, B. Fischer, W. Roseker, G. Grübel, G. Nägele, and M. Heinen, "Structure and short-time dynamics in concentrated suspensions of charged colloids," *J. Chem. Phys.* **137**(11), 114504 (2012).
- ¹⁵M. O. Robbins, K. Kremer, and G. S. Grest, "Phase diagram and dynamics of yukawa systems," *J. Chem. Phys.* **88**(5), 3286–3312 (1988).
- ¹⁶D. H. E. Dubin and T. M. O'Neil, "Trapped nonneutral plasmas, liquids, and crystals (the thermal equilibrium states)," *Rev. Mod. Phys.* **71**, 87–172 (1999).
- ¹⁷T. C. Killian, T. Pattard, T. Pohl, and J. M. Rost, "Ultracold neutral plasmas," *Phys. Rep.* **449**, 77 (2007).
- ¹⁸M. Lyon and S. L. Rolston, "Ultracold neutral plasmas," *Rep. Prog. Phys.* **80**(1), 017001 (2017).
- ¹⁹B. Jeon, M. Foster, J. Colgan, G. Csanak, J. D. Kress, L. A. Collins, and N. Grønbech-Jensen, "Energy relaxation rates in dense hydrogen plasmas," *Phys. Rev. E* **78**, 036403 (2008).
- ²⁰B. Xu and S. X. Hu, "Effects of electron-ion temperature equilibration on inertial confinement fusion implosions," *Phys. Rev. E* **84**, 016408 (2011).
- ²¹Q. Ma, J. Dai, D. Kang, M. S. Murillo, Y. Hou, Z. Zhao, and J. Yuan, "Extremely low electron-ion temperature relaxation rates in warm dense hydrogen: Interplay between quantum electrons and coupled ions," *Phys. Rev. Lett.* **122**, 015001 (2019).

- ²²R. Redmer and G. Röpke, "Progress in the theory of dense strongly coupled plasmas," *Contrib. Plasma Phys.* **50**(10), 970–985 (2010).
- ²³P. K. Shukla and B. Eliasson, "Colloquium: Nonlinear collective interactions in quantum plasmas with degenerate electron fluids," *Rev. Mod. Phys.* **83**, 885–906 (2011).
- ²⁴O. Vaulina, S. Khrapak, and G. Morfill, "Universal scaling in complex (dusty) plasmas," *Phys. Rev. E* **66**, 016404 (2002).
- ²⁵M. S. Murillo, "X-ray Thomson scattering in warm dense matter at low frequencies," *Phys. Rev. E* **81**, 036403 (2010).
- ²⁶S. X. Hu, B. Militzer, V. N. Goncharov, and S. Skupsky, "Strong coupling and degeneracy effects in inertial confinement fusion implosions," *Phys. Rev. Lett.* **104**, 235003 (2010).
- ²⁷O. Ciricosta, S. M. Vinko, B. Barbrel, D. S. Rackstraw, T. R. Preston, T. Burian, J. Chalupský, B. I. Cho, H. K. Chung, G. L. Dakovski, K. Engelhorn, V. Hájková, P. Heimann, M. Holmes, L. Juha, J. Krzywinski, R. W. Lee, S. Toleikis, J. J. Turner, U. Zastra, and J. S. Wark, "Measurements of continuum lowering in solid-density plasmas created from elements and compounds," *Nat. Commun.* **7**(1), 11713 (2016).
- ²⁸Zh. A. Moldabekov, S. Groth, T. Dornheim, H. Kählert, M. Bonitz, and T. S. Ramazanov, "Structural characteristics of strongly coupled ions in a dense quantum plasma," *Phys. Rev. E* **98**, 023207 (2018).
- ²⁹M. Schlanges, M. Bonitz, and A. Tschtschjan, "Plasma phase transition in fluid hydrogen-helium mixtures," *Contrib. Plasma Phys.* **35**(2), 109–125 (1995).
- ³⁰R. Fehr and W. D. Kraeft, "Single- and two-particle energies and thermodynamics of dense plasmas," *Contrib. Plasma Phys.* **35**(6), 463–479 (1995).
- ³¹M. W. C. Dharma-wardana and M. S. Murillo, "Pair-distribution functions of two-temperature two-mass systems: Comparison of molecular dynamics, classical-map hypernetted chain, quantum monte carlo, and kohn-sham calculations for dense hydrogen," *Phys. Rev. E* **77**, 026401 (2008).
- ³²G. Kalman and K. I. Golden, "Response function and plasmon dispersion for strongly coupled Coulomb liquids," *Phys. Rev. A* **41**, 5516–5527 (1990).
- ³³K. I. Golden and G. J. Kalman, "Quasilocated charge approximation in strongly coupled plasma physics," *Phys. Plasmas* **7**(1), 14–32 (2000).
- ³⁴Y. Rosenfeld, "Free energy model for inhomogeneous fluid mixtures: Yukawa-charged hard spheres, general interactions, and plasmas," *J. Chem. Phys.* **98**(10), 8126–8148 (1993).
- ³⁵V. Recoules, F. Lambert, A. Decoster, B. Canaud, and J. Cléroutin, "Ab initio determination of thermal conductivity of dense hydrogen plasmas," *Phys. Rev. Lett.* **102**, 075002 (2009).
- ³⁶M. P. Desjarlais, J. D. Kress, and L. A. Collins, "Electrical conductivity for warm, dense aluminum plasmas and liquids," *Phys. Rev. E* **66**, 025401 (2002).
- ³⁷T. C. Killian, S. Kulin, S. D. Bergeson, L. A. Orozco, C. Orzel, and S. L. Rolston, "Creation of an ultracold neutral plasma," *Phys. Rev. Lett.* **83**, 4776–4779 (1999).
- ³⁸J. P. Morrison, C. J. Rennick, J. S. Keller, and E. R. Grant, "Evolution from a molecular Rydberg gas to an ultracold plasma in a seeded supersonic expansion of NO," *Phys. Rev. Lett.* **101**(20), 205005 (2008).
- ³⁹M. P. Robinson, B. L. Tolra, M. W. Noel, T. F. Gallagher, and P. Pillet, "Spontaneous evolution of Rydberg atoms into an ultracold plasma," *Phys. Rev. Lett.* **85**, 4466–4469 (2000).
- ⁴⁰A. Walz-Flannigan, J. R. Guest, J.-H. Choi, and G. Raithel, "Cold-Rydberg-gas dynamics," *Phys. Rev. A* **69**, 063405 (2004).
- ⁴¹E. V. Crockett, R. C. Newell, F. Robicheaux, and D. A. Tate, "Heating and cooling of electrons in an ultracold neutral plasma using Rydberg atoms," *Phys. Rev. A* **98**, 043431 (2018).
- ⁴²S. X. Hu, "Three-body recombination of atomic ions with slow electrons," *Phys. Rev. Lett.* **98**, 133201 (2007).
- ⁴³T. Š Kotrík, P. Dohnal, Š. Roučka, P. Jusko, R. Plašil, J. Glosík, and R. Johnsen, "Collisional-radiative recombination $\text{Ar}^+ + e + e$: Experimental study at 77–180 K," *Phys. Rev. A* **83**, 032720 (2011).
- ⁴⁴S. X. Hu, "Heating of frozen Rydberg gases in a strong magnetic field," *J. Phys. B: At. Mol. Opt. Phys.* **41**(8), 081009 (2008).
- ⁴⁵T. Pohl, D. Vrinceanu, and H. R. Sadeghpour, "Rydberg atom formation in ultracold plasmas: Small energy transfer with large consequences," *Phys. Rev. Lett.* **100**, 223201 (2008).
- ⁴⁶F. Robicheaux, S. D. Loch, M. S. Pindzola, and C. P. Ballance, "Contribution of near threshold states to recombination in plasmas," *Phys. Rev. Lett.* **105**, 233201 (2010).
- ⁴⁷T. K. Langin, G. M. Gorman, and T. C. Killian, "Laser cooling of ions in a neutral plasma," *Science* **363**(6422), 61–64 (2019).
- ⁴⁸F. Robicheaux and J. D. Hanson, "Simulation of the expansion of an ultracold neutral plasma," *Phys. Rev. Lett.* **88**(5), 55002 (2002).
- ⁴⁹F. Robicheaux and J. D. Hanson, "Simulated expansion of an ultra-cold, neutral plasma," *Phys. Plasmas* **10**(6), 2217 (2003).
- ⁵⁰J. L. Roberts, C. D. Fertig, M. J. Lim, and S. L. Rolston, "Electron temperature of ultracold plasmas," *Phys. Rev. Lett.* **92**, 253003 (2004).
- ⁵¹P. Gupta, S. Laha, C. E. Simien, H. Gao, J. Castro, T. C. Killian, and T. Pohl, "Electron temperature evolution in expanding ultracold neutral plasmas," *Phys. Rev. Lett.* **99**, 75005 (2007).
- ⁵²Y. C. Chen, C. E. Simien, S. Laha, P. Gupta, Y. N. Martinez, P. G. Mickelson, S. B. Nagel, and T. C. Killian, "Electron screening and kinetic energy oscillations in a strongly coupled plasma," *Phys. Rev. Lett.* **93**, 265003 (2004).
- ⁵³D. O. Gericke and M. S. Murillo, "Disorder-induced heating of ultracold plasmas," *Contrib. Plasma Phys.* **43**, 298 (2003).
- ⁵⁴S. D. Bergeson, A. Denning, M. Lyon, and F. Robicheaux, "Density and temperature scaling of disorder-induced heating in ultracold plasmas," *Phys. Rev. A* **83**, 023409 (2011).
- ⁵⁵M. S. Murillo, "Ultrafast dynamics of strongly coupled plasmas," *Phys. Rev. Lett.* **96**, 165001 (2006).
- ⁵⁶T. K. Langin, T. Strickler, N. Maksimovic, P. McQuillen, T. Pohl, D. Vrinceanu, and T. C. Killian, "Demonstrating universal scaling for dynamics of Yukawa one-component plasmas after an interaction quench," *Phys. Rev. E* **93**, 023201 (2016).
- ⁵⁷P. McQuillen, T. Strickler, T. Langin, and T. C. Killian, "Ion temperature evolution in an ultracold neutral plasma," *Phys. Plasmas* **22**(3), 033513 (2015).
- ⁵⁸G. Zwicknagel, "Molecular dynamics simulations of the dynamics of correlations and relaxation in an OCP," *Contrib. Plasma Phys.* **39**, 155 (1999).
- ⁵⁹M. S. Murillo, "Using Fermi statistics to create strongly coupled ion plasmas in atom traps," *Phys. Rev. Lett.* **87**(11), 115003 (2001).
- ⁶⁰S. G. Kuzmin and T. M. O'Neil, "Numerical simulation of ultracold plasmas: How rapid intrinsic heating limits the development of correlation," *Phys. Rev. Lett.* **88**, 065003 (2002).
- ⁶¹I. V. Morozov and G. E. Norman, "Non-exponential dynamic relaxation in strongly nonequilibrium nonideal plasmas," *J. Phys. A: Math. Gen.* **36**, 6005 (2003).
- ⁶²C. R. D. Brown, D. O. Gericke, M. Cammarata, B. I. Cho, T. Döppner, K. Engelhorn, E. Förster, C. Fortmann, D. Fritz, E. Galtier, S. H. Glenzer, M. Harmand, P. Heimann, N. L. Kugland, D. Q. Lamb, H. J. Lee, R. W. Lee, H. Lemke, M. Makita, A. Moinard, C. D. Murphy, B. Nagler, P. Neumayer, K.-U. Plagemann, R. Redmer, D. Riley, F. B. Rosmej, P. Sperling, S. Toleikis, S. M. Vinko, J. Vorberger, S. White, T. G. White, K. Wünsch, U. Zastra, D. Zhu, T. Tschentscher, and G. Gregori, "Evidence for a glassy state in strongly driven carbon," *Sci. Rep.* **4**(1), 5214 (2014).
- ⁶³M. Lyon and S. D. Bergeson, "Towards stronger coulomb coupling in an ultracold neutral plasma," *Contrib. Plasma Phys.* **55**(5), 399–406 (2015).
- ⁶⁴T. S. Strickler, T. K. Langin, P. McQuillen, J. Daligault, and T. C. Killian, "Experimental measurement of self-diffusion in a strongly coupled plasma," *Phys. Rev. X* **6**, 021021 (2016).
- ⁶⁵H. Grad, *Handbuch der Physik* (Springer-Verlag, Berlin, 1958), Vol. 12.
- ⁶⁶A. Lenard, "On Bogoliubov's kinetic equation for a spatially homogeneous plasma," *Ann. Phys.* **10**, 390–400 (1960).
- ⁶⁷R. Balescu, "Irreversible processes in ionized gases," *Phys. Fluids* **3**, 52 (1960).
- ⁶⁸P. K. Shukla and B. Eliasson, "Nonlinear aspects of quantum plasma physics," *Phys.-Usp.* **53**(11), 51–76 (2010).
- ⁶⁹M. Bonitz, D. Semkat, A. Filinov, V. Golubnychi, D. Kremp, D. O. Gericke, M. S. Murillo, V. Filinov, V. Fortov, W. Hoyer, and S. W. Koch, "Theory and simulation of strong correlations in quantum Coulomb systems," *J. Phys. A: Math. Gen.* **36**(22), 5921–5930 (2003).
- ⁷⁰J. N. Glosli, F. R. Graziani, R. M. More, M. S. Murillo, F. H. Streitz, M. P. Surh, L. X. Benedict, S. Hau-Riege, A. B. Langdon, and R. A. London, "Molecular dynamics simulations of temperature equilibration in dense hydrogen," *Phys. Rev. E* **78**, 025401R (2008).

- ⁷¹M. Bonitz, *Quantum Kinetic Theory* (Springer International Publishing, 2016).
- ⁷²S. D. Baalrud and J. Daligault, “Effective potential theory for transport coefficients across coupling regimes,” *Phys. Rev. Lett.* **110**, 235001 (2013).
- ⁷³S. D. Baalrud and J. Daligault, “Extending plasma transport theory to strong coupling through the concept of an effective interaction potential,” *Phys. Plasmas* **21**(5), 055707 (2014).
- ⁷⁴T. S. Ramazanov and K. N. Dzhamagulova, “Effective screened potentials of strongly coupled semiclassical plasma,” *Phys. Plasmas* **9**(9), 3758–3761 (2002).
- ⁷⁵T. L. Hill, *An Introduction to Statistical Thermodynamics* (Addison-Wesley, Reading, 1960).
- ⁷⁶J. Daligault, K. Ø. Rasmussen, and S. D. Baalrud, “Determination of the shear viscosity of the one-component plasma,” *Phys. Rev. E* **90**, 033105 (2014).
- ⁷⁷N. R. Shaffer, S. D. Baalrud, and J. Daligault, “Effective potential theory for diffusion in binary ionic mixtures,” *Phys. Rev. E* **95**, 013206 (2017).
- ⁷⁸S. D. Baalrud and J. Daligault, “Temperature anisotropy relaxation of the one-component plasma,” *Contrib. Plasma Phys.* **57**(6–7), 238–251 (2017).
- ⁷⁹S. D. Baalrud and J. Daligault, “Mean force kinetic theory: A convergent kinetic theory for weakly and strongly coupled plasmas,” *Phys. Plasmas* **26**(8), 082106 (2019).
- ⁸⁰J.-P. Hansen and I. R. McDonald, *Theory of Simple Liquids*, 3rd ed. (Academic Press, Oxford, 2006).
- ⁸¹C. E. Starrett, D. Saumon, J. Daligault, and S. Hamel, “Integral equation model for warm and hot dense mixtures,” *Phys. Rev. E* **90**, 033110 (2014).
- ⁸²S. D. Baalrud and J. Daligault, “Modified Enskog kinetic theory for strongly coupled plasmas,” *Phys. Rev. E* **91**, 063107 (2015).
- ⁸³D. Enskog, “Kinetic theory of heat conductivity, viscosity and diffusion in certain condensed gases and liquids,” *K. Sven. Vetenskapskad. Handl.* **63**, 1–44 (1922).
- ⁸⁴S. D. Baalrud and J. Daligault, “Effective potential kinetic theory for strongly coupled plasmas,” *AIP Conf. Proc.* **1786**(1), 130001 (2016).
- ⁸⁵J. Daligault, S. D. Baalrud, C. E. Starrett, D. Saumon, and T. Sjöstrom, “Ionic transport coefficients of dense plasmas without molecular dynamics,” *Phys. Rev. Lett.* **116**, 075002 (2016).
- ⁸⁶J. H. Ferziger and H. G. Kaper, *Mathematical Theory of Transport Processes in Gases* (Elsevier, New York, 1972).
- ⁸⁷M. V. Beznogov and D. G. Yakovlev, “Effective potential and interdiffusion in binary ionic mixtures,” *Phys. Rev. E* **90**, 033102 (2014).
- ⁸⁸D. J. Bernstein, S. D. Baalrud, and J. Daligault, “Effects of coulomb coupling on stopping power and a link to macroscopic transport,” *Phys. Plasmas* **26**(8), 082705 (2019).
- ⁸⁹P. E. Grabowski, M. P. Surh, D. F. Richards, F. R. Graziani, and M. S. Murillo, “Molecular dynamics simulations of classical stopping power,” *Phys. Rev. Lett.* **111**, 215002 (2013).
- ⁹⁰J. A. Frenje, R. Florido, R. Mancini, T. Nagayama, P. E. Grabowski, H. Rinderknecht, H. Sio, A. Zylstra, M. Gatu Johnson, C. K. Li, F. H. Séguin, R. D. Petrasso, V. Yu. Glebov, and S. P. Regan, “Experimental validation of low-Z ion-stopping formalisms around the Bragg peak in high-energy-density plasmas,” *Phys. Rev. Lett.* **122**, 015002 (2019).
- ⁹¹W. Cayzac, A. Frank, A. Ortner, V. Bagnoud, M. M. Basko, S. Bedacht, C. Bläser, A. Blažević, S. Busold, O. Deppert, J. Ding, M. Ehret, P. Fiala, S. Frydrych, D. O. Gericke, L. Hallo, J. Helfrich, D. Jahn, E. Kjartansson, A. Knetsch, D. Kraus, G. Malka, N. W. Neumann, K. Pépitone, D. Pepler, S. Sander, G. Schaumann, T. Schlegel, N. Schroeter, D. Schumacher, M. Seibert, An. Tauschwitz, J. Vorberger, F. Wagner, S. Weih, Y. Zobus, and M. Roth, “Experimental discrimination of ion stopping models near the Bragg peak in highly ionized matter,” *Nat. Commun.* **8**(1), 15693 (2017).
- ⁹²Y. H. Ding, A. J. White, S. X. Hu, O. Certik, and L. A. Collins, “Ab initio studies on the stopping power of warm dense matter with time-dependent orbital-free density functional theory,” *Phys. Rev. Lett.* **121**, 145001 (2018).
- ⁹³A. J. White, O. Certik, Y. H. Ding, S. X. Hu, and L. A. Collins, “Time-dependent orbital-free density functional theory for electronic stopping power: Comparison to the Mermin-Kohn-Sham theory at high temperatures,” *Phys. Rev. B* **98**, 144302 (2018).
- ⁹⁴R. L. Liboff, “Transport coefficients determined using the shielded coulomb potential,” *Phys. Fluids* **2**(1), 40–46 (1959).
- ⁹⁵C. Paquette, C. Pelletier, G. Fontaine, and G. Michaud, “Diffusion coefficients for stellar plasmas,” *Astrophys. J. Suppl. Ser.* **61**, 177–195 (1986).
- ⁹⁶G. Bannasch, J. Castro, P. McQuillen, T. Pohl, and T. C. Killian, “Velocity relaxation in a strongly coupled plasma,” *Phys. Rev. Lett.* **109**, 185008 (2012).
- ⁹⁷C. E. Starrett and D. Saumon, “Electronic and ionic structures of warm and hot dense matter,” *Phys. Rev. E* **87**, 013104 (2013).
- ⁹⁸N. R. Shaffer and S. D. Baalrud, “The Barkas effect in plasma transport,” *Phys. Plasmas* **26**, 032110 (2019).
- ⁹⁹W. H. Barkas, J. N. Dyer, and H. H. Heckman, “Resolution of the Σ^- -mass anomaly,” *Phys. Rev. Lett.* **11**, 26–28 (1963).
- ¹⁰⁰S. Ichimaru, *Statistical Plasma Physics* (Addison-Wesley, Tokyo, 1992), Vol. 1.
- ¹⁰¹S. K. Tiwari, N. R. Shaffer, and S. D. Baalrud, “Thermodynamic state variables in quasiequilibrium ultracold neutral plasma,” *Phys. Rev. E* **95**, 043204 (2017).
- ¹⁰²D. B. Boercker and R. M. More, “Statistical mechanics of a two-temperature, classical plasma,” *Phys. Rev. A* **33**, 1859–1869 (1986).
- ¹⁰³P. Seufferling, J. Vogel, and C. Toepffer, “Correlations in a two-temperature plasma,” *Phys. Rev. A* **40**, 323–329 (1989).
- ¹⁰⁴R. Bredow, Th. Bornath, W.-D. Kraeft, and R. Redmer, “Hypernetted chain calculations for multi-component and nonequilibrium plasmas,” *Contrib. Plasma Phys.* **53**(4–5), 276–284 (2013).
- ¹⁰⁵N. R. Shaffer, S. Kumar Tiwari, and S. D. Baalrud, “Pair correlation functions of strongly coupled two-temperature plasma,” *Phys. Plasmas* **24**(9), 092703 (2017).
- ¹⁰⁶W.-T. Chen, C. Witte, and J. L. Roberts, “Damping of electron center-of-mass oscillation in ultracold plasmas,” *Phys. Plasmas* **23**(5), 052101 (2016).
- ¹⁰⁷W.-T. Chen, C. Witte, and J. L. Roberts, “Observation of a strong-coupling effect on electron-ion collisions in ultracold plasmas,” *Phys. Rev. E* **96**, 013203 (2017).
- ¹⁰⁸M. R. Gomez, S. A. Slutz, A. B. Sefkow, D. B. Sinars, K. D. Hahn, S. B. Hansen, E. C. Harding, P. F. Knapp, P. F. Schmit, C. A. Jennings, T. J. Awe, M. Geissel, D. C. Rovang, G. A. Chandler, G. W. Cooper, M. E. Cuneo, A. J. Harvey-Thompson, M. C. Herrmann, M. H. Hess, O. Johns, D. C. Lamppa, M. R. Martin, R. D. McBride, K. J. Peterson, J. L. Porter, G. K. Robertson, G. A. Rochau, C. L. Ruiz, M. E. Savage, I. C. Smith, W. A. Stygar, and R. A. Vesey, “Experimental demonstration of fusion-relevant conditions in magnetized liner inertial fusion,” *Phys. Rev. Lett.* **113**, 155003 (2014).
- ¹⁰⁹S. D. Baalrud and J. Daligault, “Transport regimes spanning magnetization-coupling phase space,” *Phys. Rev. E* **96**, 043202 (2017).
- ¹¹⁰X. L. Zhang, R. S. Fletcher, S. L. Rolston, P. N. Guzdar, and M. Swisdak, “Ultracold plasma expansion in a magnetic field,” *Phys. Rev. Lett.* **100**, 235002 (2008).
- ¹¹¹S. K. Tiwari and S. D. Baalrud, “Reduction of electron heating by magnetizing ultracold neutral plasma,” *Phys. Plasmas* **25**(1), 013511 (2018).
- ¹¹²T. Ott and M. Bonitz, “Diffusion in a strongly coupled magnetized plasma,” *Phys. Rev. Lett.* **107**, 135003 (2011).
- ¹¹³T. Ott, M. Bonitz, and Z. Donkó, “Effect of correlations on heat transport in a magnetized strongly coupled plasma,” *Phys. Rev. E* **92**, 063105 (2015).
- ¹¹⁴T. Ott, M. Bonitz, P. Hartmann, and Z. Donkó, “Spontaneous generation of temperature anisotropy in a strongly coupled magnetized plasma,” *Phys. Rev. E* **95**, 013209 (2017).
- ¹¹⁵T. Sprenkle, A. Dodson, Q. McKnight, R. Spencer, S. Bergeson, A. Diaw, and M. S. Murillo, “Ion friction at small values of the Coulomb logarithm,” *Phys. Rev. E* **99**, 053206 (2019).
- ¹¹⁶B. Paxton, R. Smolec, J. Schwab, A. Gautschy, L. Bildsten, M. Cantiello, A. Dotter, R. Farmer, J. A. Goldberg, A. S. Jermyn, S. M. Kanbur, P. Marchant, A. Thoul, R. H. D. Townsend, W. M. Wolf, M. Zhang, and F. X. Timmes, “Modules for experiments in stellar astrophysics (MESA): Pulsating variable stars, rotation, convective boundaries, and energy conservation,” *Astrophys. J. Suppl. Ser.* **243**(1), 10 (2019).
- ¹¹⁷B. Paxton, J. Schwab, E. B. Bauer, L. Bildsten, S. Blinnikov, P. Duffell, R. Farmer, J. A. Goldberg, P. Marchant, E. Sorokina, A. Thoul, R. H. D. Townsend, and F. X. Timmes, “Modules for experiments in stellar astrophysics (MESA): Convective boundaries, element diffusion, and massive star explosions,” *Astrophys. J. Suppl. Ser.* **234**(2), 34 (2018).
- ¹¹⁸Y. Zhou, “Rayleigh–Taylor and Richtmyer–Meshkov instability induced flow, turbulence, and mixing. II,” *Phys. Rep.* **723–725**, 1–160 (2017).

- ¹¹⁹C. Ticknor, J. D. Kress, L. A. Collins, J. Cl  rouin, P. Arnault, and A. Decoster, "Transport properties of an asymmetric mixture in the dense plasma regime," *Phys. Rev. E* **93**(6), 063208 (2016).
- ¹²⁰L. G. Stanton and M. S. Murillo, "Ionic transport in high-energy-density matter," *Phys. Rev. E* **93**, 043203 (2016).
- ¹²¹O. Aono, "Various expressions of the kinetic equation for a plasma," *Phys. Plasmas* **11**(2), 341–345 (1968).
- ¹²²D. O. Gericke, M. S. Murillo, and M. Schlanges, "Dense plasma temperature equilibration in the binary collision approximation," *Phys. Rev. E* **65**(3), 036418 (2002).
- ¹²³S. Chapman and T. G. Cowling, *The Mathematical Theory of Non-Uniform Gases* (Cambridge University Press, 1991).
- ¹²⁴L. G. Stanton, J. N. Glosli, and M. S. Murillo, "Multiscale molecular dynamics model for heterogeneous charged systems," *Phys. Rev. X* **8**, 021044 (2018).
- ¹²⁵C. L. Ellison, H. D. Whitley, C. R. D. Brown, S. R. Copeland, W. J. Garbett, H. P. Le, M. B. Schneider, Z. B. Walters, H. Chen, J. I. Castor, R. S. Craxton, M. Gatu Johnson, E. M. Garcia, F. R. Graziani, G. E. Kemp, C. M. Krauland, P. W. McKenty, B. Lahmann, J. E. Pino, M. S. Rubery, H. A. Scott, R. Shepherd, and H. Sio, "Development and modeling of a polar-direct-drive exploding pusher platform at the national ignition facility," *Phys. Plasmas* **25**(7), 072710 (2018).
- ¹²⁶D. Mihalas, *Stellar Atmospheres*, 2nd ed. (W.H. Freeman and Company, New York, 1977).
- ¹²⁷G. Rybicki and A. Lightman, *Radiative Processes in Astrophysics*, 2nd ed. (Wiley-VCH Verlag, Berlin, Germany, 2004).
- ¹²⁸G. Pomraning, *The Equations of Radiation Hydrodynamics*, 1st ed. (Pergamon Press, New York, 1973).
- ¹²⁹D. Mihalas and B. Weibel-Mihalas, *Foundations of Radiation Hydrodynamics*, 1st ed. (Oxford University Press, New York, 1984).
- ¹³⁰S. Ichimaru, "Strongly coupled plasmas: high-density classical plasmas and degenerate electron liquids," *Rev. Mod. Phys.* **54**, 1017 (1982).
- ¹³¹S. Ichimaru, H. Iyetomi, and S. Tanaka, "Statistical physics of dense plasmas: thermodynamics, transport coefficients and dynamic correlations," *Phys. Rep.* **149**, 91 (1987).
- ¹³²R. M. Darlington, T. L. McAbee, and G. Rodrigue, "A study of ALE simulations of Rayleigh–Taylor instability," *Comput. Phys. Commun.* **135**(1), 58–73 (2001).
- ¹³³B. E. Morgan and J. A. Greenough, "Large-Eddy and unsteady RANS simulations of a shock-accelerated heavy gas cylinder," *Shock Waves* **26**(4), 355–383 (2016).
- ¹³⁴A. J. White, L. A. Collins, J. D. Kress, C. Ticknor, J. Cl  rouin, P. Arnault, and N. Desbiens, "Correlation and transport properties for mixtures at constant pressure and temperature," *Phys. Rev. E* **95**, 063202 (2017).
- ¹³⁵E. R. Meyer, J. D. Kress, L. A. Collins, and C. Ticknor, "Effect of correlation on viscosity and diffusion in molecular-dynamics simulations," *Phys. Rev. E* **90**, 043101 (2014).
- ¹³⁶D. C. Wilson, A. J. Scannapieco, C. W. Cranfill, M. R. Clover, N. M. Hoffman, and J. Collins, "Degradation of radiatively driven inertial confinement fusion capsule implosions by multifluid interpenetration mixing," *Phys. Plasmas* **10**(11), 4427–4434 (2003).
- ¹³⁷C. R. Weber, D. S. Clark, A. W. Cook, L. E. Busby, and H. F. Robey, "Inhibition of turbulence in inertial-confinement-fusion hot spots by viscous dissipation," *Phys. Rev. E* **89**, 053106 (2014).
- ¹³⁸M. S. Murillo, "Viscosity estimates of liquid metals and warm dense matter using the yukawa reference system," *High Energy Density Phys.* **4**(1), 49–57 (2008).
- ¹³⁹R. E. Rudd, "Notes on the Yukawa viscosity model," Technical report, LLNL Report No. LLNL-MI-661976 (Lawrence Livermore National Laboratory, 2012).
- ¹⁴⁰T. Haxhimali, R. E. Rudd, W. H. Cabot, and F. R. Graziani, "Shear viscosity for dense plasmas by equilibrium molecular dynamics in asymmetric Yukawa ionic mixtures," *Phys. Rev. E* **92**, 053110 (2015).
- ¹⁴¹J. M. Burgers, *Flow Equations for Composite Gases* (Academic Press, Inc., New York, 1969).
- ¹⁴²L. D. Landau, "Kinetic equation for the Coulomb effect," *JETP* **7**, 203 (1937).
- ¹⁴³H. Brysk, "Electron-ion equilibration in a partially degenerate plasma," *Plasma Phys.* **16**(10), 927 (1974).
- ¹⁴⁴M. W. C. Dharma-wardana and F. Perrot, "Energy relaxation and the quasiequation of state of a dense two-temperature nonequilibrium plasma," *Phys. Rev. E* **58**, 3705–3718 (1998).
- ¹⁴⁵L. S. Brown, D. L. Preston, and R. L. Singleton, Jr., "Charged particle motion in a highly ionized plasma," *Phys. Rep.* **410**(4), 237–333 (2005).
- ¹⁴⁶J. Daligault and G. Dimonte, "Correlation effects on the temperature-relaxation rates in dense plasmas," *Phys. Rev. E* **79**, 056403 (2009).
- ¹⁴⁷J. Vorberger, D. O. Gericke, Th. Bornath, and M. Schlanges, "Energy relaxation in dense, strongly coupled two-temperature plasmas," *Phys. Rev. E* **81**, 046404 (2010).
- ¹⁴⁸M. Lampe, "Transport theory of a partially degenerate plasma," *Phys. Rev.* **174**, 276 (1968).
- ¹⁴⁹C. R. Scullard, A. Hickok, J. O. Sotiris, B. M. Tzolova, R. L. Van Heyningen, and F. R. Graziani, "Adaptive spectral solution method for the Landau and Lenard-Balescu equations," preprint [arXiv:1812.04084](https://arxiv.org/abs/1812.04084) [physics.comp-ph] (2018).
- ¹⁵⁰C. R. Scullard, S. Serna, L. X. Benedict, C. L. Ellison, and F. R. Graziani, "Analytic expressions for electron-ion temperature equilibration rates from the Lenard-Balescu equation," *Phys. Rev. E* **97**, 013205 (2018).
- ¹⁵¹L. X. Benedict, M. P. Surh, J. I. Castor, S. A. Khairallah, H. D. Whitley, D. F. Richards, J. N. Glosli, M. S. Murillo, C. R. Scullard, P. E. Grabowski, D. Michta, and F. R. Graziani, "Molecular dynamics simulations and generalized Lenard-Balescu calculations of electron-ion temperature equilibration in plasmas," *Phys. Rev. E* **86**, 046406 (2012).
- ¹⁵²L. X. Benedict, M. P. Surh, L. G. Stanton, C. R. Scullard, A. A. Correa, J. I. Castor, F. R. Graziani, L. A. Collins, O.   rtik, J. D. Kress, and M. S. Murillo, "Molecular dynamics studies of electron-ion temperature equilibration in hydrogen plasmas within the coupled-mode regime," *Phys. Rev. E* **95**, 043202 (2017).
- ¹⁵³D. O. Gericke, "Kinetic approach to temperature relaxation in dense plasmas," *J. Phys. Conf. Ser.* **11**, 111–123 (2005).
- ¹⁵⁴W. Li, M. W. Noel, M. P. Robinson, P. J. Tanner, T. F. Gallagher, D. Comparat, B. L. Tolra, N. Vanhaecke, T. Vogt, N. Zahzam, P. Pillet, and D. A. Tate, "Evolution dynamics of a dense frozen Rydberg gas to plasma," *Phys. Rev. A* **70**(4), 10 (2004).
- ¹⁵⁵M. Robert-de-Saint-Vincent, C. S. Hofmann, H. Schempp, G. G  nter, S. Whitlock, and M. Weidem  ller, "Spontaneous avalanche ionization of a strongly blockaded Rydberg gas," *Phys. Rev. Lett.* **110**, 045004 (2013).
- ¹⁵⁶M. Schulz-Weiling and E. R. Grant, "Quantum state control of ultracold plasma fission," *J. Phys. B: At. Mol. Opt. Phys.* **49**(6), 064009 (2016).
- ¹⁵⁷R. Haedel, M. Schulz-Weiling, J. Sous, H. Sadeghi, M. Aghigh, L. Melo, J. S. Keller, and E. R. Grant, "Arrested relaxation in an isolated molecular ultracold plasma," *Phys. Rev. A* **96**, 023613 (2017).
- ¹⁵⁸M. Schulz-Weiling, H. Sadeghi, J. Hung, and E. Grant, "On the evolution of the phase-space distributions of a non-spherical molecular ultracold plasma in a superionic beam," *J. Phys. B: At. Mol. Opt. Phys.* **49**(19), 193001 (2016).
- ¹⁵⁹D. Comparat and P. Pillet, "Dipole blockade in a cold Rydberg atomic sample," *J. Opt. Soc. Am. B* **27**(6), A208–A232 (2010).
- ¹⁶⁰S. Torquato, B. Lu, and J. Rubinstein, "Nearest-neighbor distribution functions in many-body systems," *Phys. Rev. A* **41**(4), 2059–2075 (1990).
- ¹⁶¹F. Robicheaux, "Ionization due to the interaction between two Rydberg atoms," *J. Phys. B: At. Mol. Opt. Phys.* **38**, S333–S342 (2005).
- ¹⁶²H. Sadeghi, A. Kruey, J. Hung, J. H. Gurian, J. P. Morrison, M. Schulz-Weiling, N. Saquet, C. J. Rennick, and E. R. Grant, "Dissociation and the development of spatial correlation in a molecular ultracold plasma," *Phys. Rev. Lett.* **112**, 075001 (2014).
- ¹⁶³T. Pohl, T. Pattard, and J. M. Rost, "Kinetic modeling and molecular dynamics simulation of ultracold neutral plasmas including ionic correlations," *Phys. Rev. A* **70**(3), 33416 (2004).
- ¹⁶⁴N. Saquet, J. P. Morrison, M. Schulz-Weiling, H. Sadeghi, J. Yiu, C. J. Rennick, and E. R. Grant, "On the formation and decay of a molecular ultracold plasma," *J. Phys. B: At. Mol. Opt. Phys.* **44**, 184015 (2011).
- ¹⁶⁵N. Saquet, J. P. Morrison, and E. Grant, "Recombinative dissociation and the evolution of a molecular ultracold plasma," *J. Phys. B: At. Mol. Opt. Phys.* **45**, 175302 (2012).
- ¹⁶⁶J. P. Morrison, N. Saquet, and E. R. Grant, "Classical scaling and the correspondence between the coupled rate equation and molecular dynamics models

- for the evolution of ultracold neutral plasma," *J. Phys. B: At. Mol. Opt. Phys.* **45**(2), 025701-1–7 (2012).
- ¹⁶⁷J. Hung, H. Sadeghi, M. Schluz-Weiling, and E. R. Grant, "Evolution from Rydberg gas to ultracold plasma in a supersonic atomic beam of Xe," *J. Phys. B: At. Mol. Opt. Phys.* **47**, 155301 (2014).
- ¹⁶⁸R. Haenel and E. R. Grant, "Coupled rate-equation hydrodynamic simulation of a rydberg gas Gaussian ellipsoid: Classical avalanche and evolution to molecular plasma," *Chem. Phys.* **514**, 55–66 (2018).
- ¹⁶⁹H. Sadeghi and E. R. Grant, "Dissociative recombination slows the expansion of a molecular ultracold plasma," *Phys. Rev. A* **86**(5), 052701 (2012).
- ¹⁷⁰T. Pohl, T. Pattard, and J. M. Rost, "Plasma formation from ultracold Rydberg gases," *Phys. Rev. A* **68**(1), 010703 (2003).
- ¹⁷¹J. Sous and E. R. Grant, "Possible many-body localization in a long-lived finite-temperature ultracold quasi-neutral molecular plasma," *Phys. Rev. Lett.* **120**, 110601 (2018).
- ¹⁷²J. Sous and E. R. Grant, "Many-body physics with ultracold plasmas: Quenched randomness and localization," *New J. Phys.* **21**, 043033 (2019).
- ¹⁷³A. L. Burin, "Localization in a random xy model with long-range interactions: Intermediate case between single-particle and many-body problems," *Phys. Rev. B* **92**, 104428 (2015).
- ¹⁷⁴R. M. Nandkishore and S. L. Sondhi, "Many body localization with long range interactions," *Phys. Rev. X* **7**, 041021 (2017).
- ¹⁷⁵J. P. Morrison and E. R. Grant, "Dynamics of colliding ultracold plasmas," *Phys. Rev. A* **91**, 023423 (2015).
- ¹⁷⁶S. Laha, P. Gupta, C. E. Simien, H. Gao, J. Castro, and T. C. Killian, "Experimental realization of an exact solution to the Vlasov equations for an expanding plasma," *Phys. Rev. Lett.* **99**, 155001 (2007).
- ¹⁷⁷J. Castro, H. Gao, and T. C. Killian, "Using sheet fluorescence to probe ion dynamics in an ultracold neutral plasma," *Plasma Phys. Controlled Fusion* **50**, 124011 (2008).
- ¹⁷⁸The CCD camera provides spatial resolution as well, which enables analysis of individual regions of the plasma that have little variation in density and average plasma expansion velocity. For simplicity, during this discussion we neglect this additional capability.
- ¹⁷⁹L. Spitzer and R. Härm, "Evaporation of stars from isolated clusters," *Astrophys. J.* **127**, 544 (1958).
- ¹⁸⁰G. Dimonte and J. Daligault, "Molecular-dynamics simulations of electron-ion temperature relaxation in a classical coulomb plasma," *Phys. Rev. Lett.* **101**, 135001 (2008).
- ¹⁸¹S. D. Baalrud, "Transport coefficients in strongly coupled plasmas," *Phys. Plasmas* **19**(3), 030701 (2012).
- ¹⁸²J. P. Hansen, I. R. McDonald, and E. L. Pollock, "Statistical mechanics of dense ionized matter. III. Dynamical properties of the classical one-component plasma," *Phys. Rev. A* **11**(3), 1025 (1975).
- ¹⁸³S. Ichimaru, *Statistical Plasma Physics, Volume II: Condensed Plasmas*, Frontiers in Physics (Westview Press, Boulder, CO, 2004).
- ¹⁸⁴J. Daligault, "Diffusion in ionic mixtures across coupling regimes," *Phys. Rev. Lett.* **108**, 225004 (2012).
- ¹⁸⁵F. L. Hinton and R. D. Hazeltine, "Theory of plasma transport in toroidal confinement systems," *Rev. Mod. Phys.* **48**, 239–308 (1976).
- ¹⁸⁶J. A. Frenje, P. E. Grabowski, C. K. Li, F. H. Séguin, A. B. Zylstra, M. Gatu Johnson, R. D. Petrasso, V. Yu. Glebov, and T. C. Sangster, "Measurements of ion stopping around the Bragg peak in high-energy-density plasmas," *Phys. Rev. Lett.* **115**, 205001 (2015).
- ¹⁸⁷A. B. Zylstra, J. A. Frenje, P. E. Grabowski, C. K. Li, G. W. Collins, P. Fitzsimmons, S. Glenzer, F. Graziani, S. B. Hansen, S. X. Hu, M. G. Johnson, P. Keiter, H. Reynolds, J. R. Rygg, F. H. Séguin, and R. D. Petrasso, "Measurement of charged-particle stopping in warm dense plasma," *Phys. Rev. Lett.* **114**, 215002 (2015).
- ¹⁸⁸T. M. Wilson, W.-T. Chen, and J. L. Roberts, "Density-dependent response of an ultracold plasma to few-cycle radio-frequency pulses," *Phys. Rev. A* **87**, 013410 (2013).
- ¹⁸⁹N. Heilmann, J. B. Peatross, and S. D. Bergeson, "'Ultracold' neutral plasmas at room temperature," *Phys. Rev. Lett.* **109**, 035002 (2012).
- ¹⁹⁰J. Guthrie and J. Roberts, "A scalable theoretical mean-field model for the electron component of an ultracold neutral plasma," *J. Phys. B: At. Mol. Opt. Phys.* **49**(4), 045701 (2016).
- ¹⁹¹G. Bannasch and T. Pohl, "Rydberg-atom formation in strongly correlated ultracold plasmas," *Phys. Rev. A* **84**, 052710 (2011).
- ¹⁹²T. Wilson, W.-T. Chen, and J. Roberts, "Influence of electron evaporative cooling on ultracold plasma expansion," *Phys. Plasmas* **20**(7), 073503 (2013).
- ¹⁹³G. Dharuman, L. G. Stanton, J. N. Glosli, and M. S. Murillo, "A generalized Ewald decomposition for screened Coulomb interactions," *J. Chem. Phys.* **146**(2), 024112 (2017).
- ¹⁹⁴K. N. Kudin and G. E. Scuseria, "A fast multipole method for periodic systems with arbitrary unit cell geometries," *Chem. Phys. Lett* **283**(1), 61–68 (1998).
- ¹⁹⁵J. D. Huba, *NRL Plasma Formulary Supported by the Office of Naval Research* (Naval Research Laboratory, Washington, DC, 2013).
- ¹⁹⁶M. S. Murillo, "Strongly coupled plasma physics and high energy density matter," *Phys. Plasmas* **11**, 2964 (2004).
- ¹⁹⁷P. Amendt, O. L. Landen, H. F. Robey, C. K. Li, and R. D. Petrasso, "Plasma barodiffusion in inertial-confinement-fusion implosions: Application to observed yield anomalies in thermonuclear fuel mixtures," *Phys. Rev. Lett.* **105**, 115005 (2010).
- ¹⁹⁸J. H. Bin, M. Yeung, Z. Gong, H. Y. Wang, C. Kreuzer, M. L. Zhou, M. J. V. Streeter, P. S. Foster, S. Cousens, B. Dromey, J. Meyer-ter Vehn, M. Zepf, and J. Schreiber, "Enhanced laser-driven ion acceleration by superponderomotive electrons generated from near-critical-density plasma," *Phys. Rev. Lett.* **120**, 074801 (2018).
- ¹⁹⁹V. Aslanyan, S. E. Sharapov, D. A. Spong, and M. Porkolab, "Two species drag/diffusion model for energetic particle driven modes," *Phys. Plasmas* **24**(12), 122511 (2017).
- ²⁰⁰M. Marcianite and M. S. Murillo, "Thermodynamic and kinetic properties of shocks in two-dimensional Yukawa systems," *Phys. Rev. Lett.* **118**, 025001 (2017).
- ²⁰¹W. L. Shang, R. Betti, S. X. Hu, K. Woo, L. Hao, C. Ren, A. R. Christopherson, A. Bose, and W. Theobald, "Electron shock ignition of inertial fusion targets," *Phys. Rev. Lett.* **119**, 195001 (2017).
- ²⁰²A. Kramida, Yu. Ralchenko, J. Reader, and NIST ASD Team, <https://physics.nist.gov/asd> for "NIST Atomic Spectra Database (ver. 5.5.3)," National Institute of Standards and Technology, Gaithersburg, MD, 2018.
- ²⁰³See <https://heds-center.llnl.gov/> for the LLNL High Energy Density Science Center.